DISS. ETH NO. 21984

A variational approach to coherent structures in unsteady dynamical systems

A thesis submitted to attain the degree of
DOCTOR OF SCIENCES of ETH ZURICH
(Dr. sc. ETH Zurich)

presented by
MOHAMMAD FARAZMAND
M.A.Sc., McMaster University, Hamilton

born on 18.04.1985
citizen of Iran

accepted on the recommendation of
Prof. George Haller
Prof. Siddhartha Mishra
Dr. Kathrin Padberg-Gehle

2014

Dedicated to

Jalal Rasti

who fostered critical thinking

Contents

Acknowledgments

I am indebted to my advisor, Prof. George Haller, who has been a constant source of invaluable support and advice throughout my Ph.D. studies. Good research often emerges from pursuing a simple curiosity with unclear outcomes. George never stopped me from following such curiosities and even encouraged me to do so. I'd like to express my gratitude for his faith in me.

I started my Ph.D. at McGill University (Montreal, Canada) where I did most of my course work. I would like to thank the Department of Mathematics and Statistics at McGill for providing a lovely learning and research environment.

Changing institution in the midst of Ph.D. studies is not easy. I would like to thank the Department of Mathematics at ETH Zürich for making this transition possible and smooth. In particular, I'd like to thank my co-advisor, Prof. Siddhartha Mishra, for his support and guidance. My office at ETH was located in the Institute of Mechanical Systems (IMES). I am grateful to the hospitality of IMES members.

Over the last four years, I enjoyed many fruitful discussions with several colleagues including Javier Beron-Vera, Anton Daitche, Jan Feys, Manikandan Mathur, Josefina Olascoaga, Irina Rypina, Tamás Tél and the members of the Haller Group. I sincerely thank you all for your insight. Chapters 3 and 6 are the result of join work with Daniel Blazevski and Alireza Hadjighasem, respectively. I'd like to acknowledge their contributions.

Last but not least, I thank my family for their unconditional support and love.

Abstract

Lagrangian coherent structures (LCSs) are time-evolving surfaces that shape trajectory patterns in non-autonomous dynamical systems, such as turbulent fluid flows.

Hyperbolic LCSs (generalized stable-unstable manifolds) are the main drivers of chaotic mixing in the phase space. Elliptic and parabolic LCSs (generalized KAM tori), on the other hand, confine coherent patches with regular dynamics. In many applications, these structures co-exist, partitioning the phase space into regions of distinct dynamics. Hence, knowledge of the location and evolution of LCSs is key to the understanding of the overall dynamics.

Here, we show that LCSs are the solutions of suitably defined variational problems. Hyperbolic and parabolic (shearless) LCSs are shown to be the extrema of a Lagrangian shear functional. Elliptic LCSs, on the other hand, extremize a Lagrangian strain functional.

Using these variational principles, we develop algorithms for numerical detection of LCSs from models and data sets. The algorithms are tested on several examples. They are then used to study a variety of transport phenomena in fluid flows as well as the stability of mechanical systems with arbitrary time-dependence.

Compendio

Lagrangian Coherent Structures(LCSs) rappresentano superfici tempo-varianti che guidano le traiettorie di sistemi non autonomi come ad esempio il moto dei fluidi.

LCSs Iperboliche sono le guide principali dell'evoluzione temporale in fenomeni caotici come la miscelazione di fluidi. LCSs Ellittiche e Paraboliche (KAM Tori Generalizzati), invece, confinano regioni coerenti con dinamiche regolari. In molte applicazioni, queste strutture coesistono dividendo il diagramma delle fasi di un sistema dinamico in regioni distinte. La conoscenza della posizione e dell'evoluzione di queste strutture separatrici quindi di fondamentale importanza per capire la dinamica complessiva di sistemi complessi.

Nel presente lavoro mostriamo come LCSs sono soluzioni di particolari problemi variazionali adeguatamente definiti. LCSs Iperboliche e Paraboliche sono estremi del funzionale chiamato Taglio Lagrangiano (Lagrangian Shear) mentre LCSs Ellittiche sono estremi del funzionale Deformazione Lagrangiana (Lagrangian Strain).

Utilizzando questi principi variazionali, sviluppiamo algoritmi numerici per l'identificazione di LCSs in modelli definiti analiticamente o tramite data-set numerici. Tali algoritmi sono stati testati su diversi sistemi e sono utilizzati per lo studio di fenomeni quali il trasporto nei fluidi e la stabilit di sistemi meccanici con arbitrarie dipendenze dal tempo.

Chapter 0

General introduction

0.1 Introduction

The problem of transport and mixing in fluid flows is a truly multidisciplinary area of science with challenging mathematical, physical and engineering aspects. Engineering applications include fuel mixing in jet engines [1] and mixing in micro- and nano-scale devices [2]. In nature, transport phenomena have crucial environmental consequences such as transport of heat, nutritions and garbage through the ocean currents [3]. It has even been proposed that the heat transport by particular ocean eddies impacts climate change [4].

Mixing of scalars in a background continuum can occur through various mechanisms. Material transport, for instance, happens through diffusion and advection. Modeling molecular diffusion by Brownian motion, dispersion of a passive scalar field $\theta(\mathbf{x}, t)$ is governed by the advection-diffusion equation

$$\partial_t \theta + \mathbf{u} \cdot \boldsymbol{\nabla} \theta = \nu \Delta \theta, \tag{1}$$

where the constant ν is the mass diffusivity and $\mathbf{u}(\mathbf{x}, t)$ is the fluid velocity. The analysis of the various aspects of the advection-diffusion equation is a subject of active research (see [5], for an extensive review).

Molecular diffusion occurs slowly and therefore is only significant over long time-scales. For "short" time-scales, one can neglect the molecular diffusion and study the transport through pure material advection. Throughout the present work, we make this assumption (i.e., negligibility of molecular diffusion) and focus on transport and mixing due to pure advection.

Neglecting diffusion is equivalent to setting $\nu = 0$ in equation (1). Therefore, passive tracer dynamics under pure material advection is governed by the equation $\partial_t \theta + \mathbf{u} \cdot \boldsymbol{\nabla} \theta = 0$. As one expects, this equation implies that the passive tracer θ is conserved along fluid trajectories, i.e., $\theta(\mathbf{x}(t; \mathbf{x}_0, t_0), t) = \theta(\mathbf{x}_0, t_0)$ where $\mathbf{x}(t; \mathbf{x}_0, t_0)$ denotes the time-t position of a fluid trajectory starting from the initial condition $\mathbf{x}_0$ at time t_0.

Fluid trajectories coincide with the solutions of the ordinary differential equation (ODE) $\dot{\mathbf{x}} = \mathbf{u}(\mathbf{x}, t)$. This ties the analysis of mixing patterns to the

theory of finite-dimensional dynamical systems. In general, these trajectories can be very complicated, resulting in complex mixing patterns.

As an illustration, Fig. 1 shows an initially simple concentration field which develops very complex mixing patterns after being advected by the background flow. Here the background flow is a numerical solution of the forced Navier–Stokes equations restricted to two spatial dimensions. In Chapter 5, we revisit this flow in full detail.

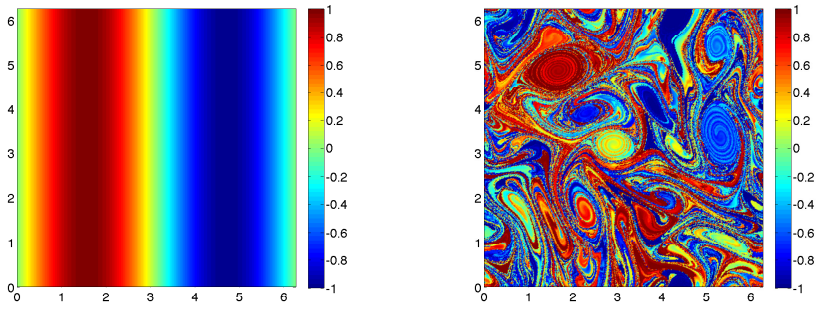

Figure 1: Left: Initial concentration of a passive scalar. Right: The passive scalar concentration after 100 time units. The background flow is a turbulent solution of the Navier–Stokes equation in two dimensions.

Being turbulent, the velocity field $\mathbf{u}(\mathbf{x}, t)$ of Fig. 1 has a complex spatiotemporal structure. As such, the complexity of the resulting mixing pattern might be expected. However, even simple velocity fields can generate complicated mixing patterns. We illustrate this on an example.

Consider the two-dimensional cellular velocity field $\mathbf{u} = (-\partial_y\psi, \partial_x\psi)^\top$ with stream function $\psi(x, y) = \sin(\pi x)\sin(\pi y)$ where $\mathbf{x} = (x, y)^\top$ is the spatial coordinates. The cellular flow is integrable with trajectories confined to the level curves of the stream function ψ (see Fig. 2). The resulting dynamical system $\dot{\mathbf{x}} = \mathbf{u}(\mathbf{x})$ has two elliptic fixed points at $(1/2, 1/2)$ and $(3/2, 1/2)$ and two hyperbolic fixed points at $(1, 0)$ and $(1, 1)$ connected by a heteroclinic orbit that coincides with the line $x = 1$. This separatrix acts as a transport barrier inhibiting mixing between the two cells.

In general, Poincaré–Bendixson theorem eliminates the possibility of chaotic trajectories in two-dimensional autonomous vector fields [see, e.g., 6]. In higher dimensions, autonomous dynamical systems can produce chaotic trajectories and as a result exhibit complicated dynamics. Here, however, we would like to illustrate that adding a simple time-dependence to a simple two-dimensional vector field can lead to chaotic trajectories and, as a result, to complex mixing patterns.

To this end we consider a time-periodic perturbation, first introduced by Shadden et al. [7], to the above-mentioned cellular flow. Leaving the details to Section 1.5.1, under this perturbation, the heteroclinic separatrix of the Eulerian frame remains a vertical straight line, oscillating left-right with a frequency $1/T$

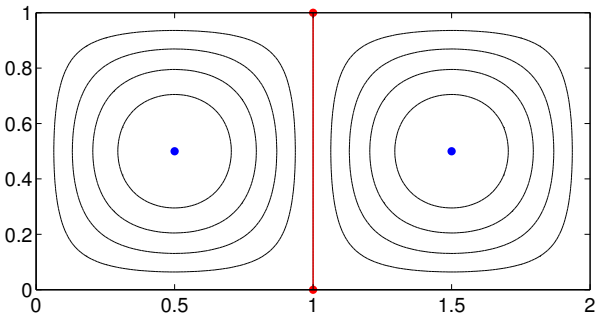

Figure 2: The streamlines (black) of the cellular flow. The two elliptic fixed points are marked with blue dots. Two hyperbolic fixed points (red dots) are connected by a heteroclinic orbit (red line).

where T is the period of the perturbation. Moreover, the domain $[0, 2] \times [0, 1]$ remains invariant and the velocity field $\mathbf{u}$ remains incompressible under this sinusoidal perturbation.

As such, the resulting velocity field is far from being turbulent, possessing a simple spatiotemporal structure. Yet, it can be shown that it generates chaotic Lagrangian trajectories and hence complex mixing patterns.

To illustrate this, we seed two sets of initial conditions on either side of the separatrix $x = 1$ at time $t = 0$, as shown in Fig. 3a. Note that in the autonomous case, these two sets will remain unmixed for all times. In the presence of the perturbation, however, the two sets become completely mixed after a few periods of the perturbation (see Fig. 3b-c).

The observation that adding simple time dependence to simple velocity fields potentially leads to chaotic Lagrangian dynamics was first made in the seminal work of Aref [8], giving birth to the field of *chaotic advection*. Since then, great progress has been made towards a better understanding of the mechanisms involved in the process of chaotic advection (see [9–11], for reviews).

The geometric theory of dynamical systems has been one of the main contributors to this progress, due to the aforementioned connection between the advection equation $\partial_t \theta + \mathbf{u} \cdot \boldsymbol{\nabla} \theta = 0$ and the dynamical system $\dot{\mathbf{x}} = \mathbf{u}(\mathbf{x}, t)$. In a nutshell, hyperbolic invariant manifolds enhance mixing due to exponential stretching and folding of nearby material elements [12, 13]. On the other hand, invariant Kolmogorov-Arnold–Moser (KAM) tori inhibit mixing and form regions of coherent dynamics [14–16].

While the invariant manifolds provide a strong geometric tool for the analysis of dynamical systems, their application is restricted to autonomous and time-periodic systems. This limitation is due to the fact that, in a *time-aperiodic* dynamical system, material surfaces evolve indefinitely with no particular recurrence pattern. As a result, no material surface is truly invariant in any useful sense.

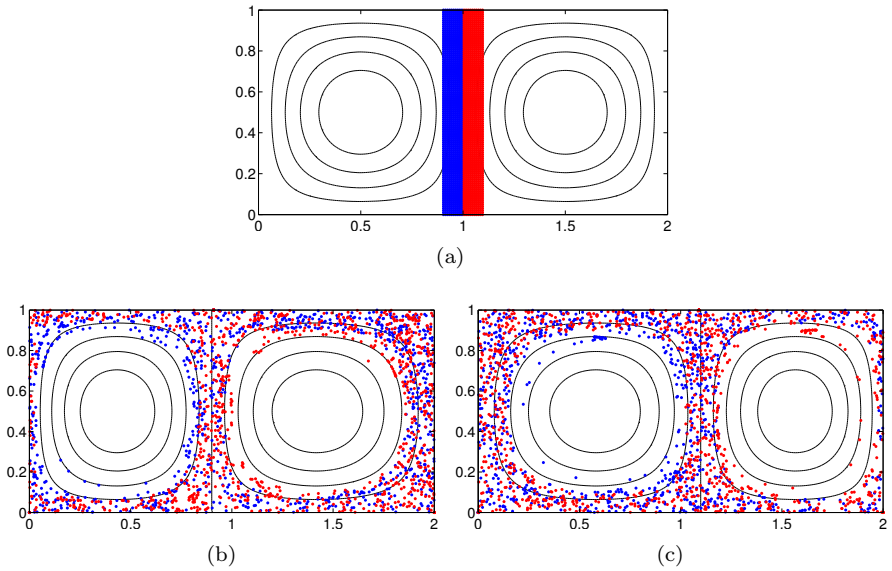

Figure 3: Periodically perturbed cellular flow or the double gyre. Two sets of initial conditions marked in red and blue are released at time $t = 0$ (a). The initial conditions are advected under the flow to times $\frac{35T}{4}$ (b) and $\frac{65T}{4}$ (c) where the period of the perturbation is $T = 2$.

At the same time, there is great interest in analysis of chaotic advection in time-aperiodic flows. This is mostly motivated by the simple fact that almost all fluid flow in nature are unsteady; consider for instance the ocean currents or atmospheric flow. As a result, the state-of-the-art research on chaotic advection is focused on unsteady flows.

Great progress has been made in this area with many contributions from researchers who have approached the problem from various angles. One may divide the different approaches into three general groups[1]:

(i) *Differential-geometric approach*: This approach generalizes the notion of invariant manifolds to unsteady flows [18, 19]. Strictly speaking, these manifolds are not invariant in the phase space; yet they are the most important players in the formation of mixing patterns due to their distinguished impact on nearby material elements. Initial attempts in this direction where focused on generalizing the notion of *hyperbolic* invariant manifolds that facilitate mixing [20–22, 7]. More recently, invariant KAM tori, as inhibitors of mixing, have also been generalized to the unsteady setting [23–26].

(ii) *Measure-theoretic approach*: This approach uses the ideas from ergodic

[1]This categorization is not meant as an all-encompassing list. For an extensive review of the field see Aref et al. [17].

theory [27] to develop tools for the analysis of unsteady flows. The invariants of appropriately modified Perron-Frobenius [28, 29] and Koopman [30, 31] operators are used to identify coherent subsets of the phase space with relatively small dispersion.

(iii) *Diagnostic tools*: A number of diagnostics have been developed whose features are argued to indicate the most influential material surfaces governing transport and mixing in unsteady flows [32–38]. These diagnostics are usually a scalar field and can be computed with a relatively low computational cost. As such, they are also referred to as *fast indicators*.

In the present work, we take the view of approach (i) above. This view was first introduced by Haller and Yuan [21] who proposed that in unsteady flow one should seek most influential material surfaces that shape the mixing patterns in the flow by their distinguished effect on nearby material elements. They referred to such distinguished material surfaces as *Lagrangian Coherent Structures* (LCSs). Hyperbolic LCSs enhance mixing by stretching and folding nearby material elements, while elliptic and parabolic LCSs inhibit mixing by confining coherent regions of the flow that resist significant deformation. LCSs are, in a sense, a generalization of hyperbolic invariant manifolds and invariant KAM tori.

LCSs were subsequently visualized using diagnostic tools [34, 39, 40] and were applied to study a variety of physics and engineering problems [41–43]. Only recently, however, was an attempt made to define and identify LCSs with mathematical rigor [44–46, 23].

The main insight in [44] is the fact that one can locate LCSs as the solutions of a suitably formulated variational problem. Adopting this view, here we develop variational principles for LCS detection. Based on these principles, we devise algorithms for numerical detection of LCSs from models and data sets. The algorithms are then used to study a number of transport phenomena.

0.2 Set-up

Consider the differential equation

$$\dot{\mathbf{x}} = \mathbf{u}(\mathbf{x}, t), \quad \mathbf{x} \in U, \quad t \in [a, b], \tag{2}$$

with U denoting an open, bounded subset of $\mathbb{R}^n$, with the time t varying over the finite interval $[a, b]$, and with the velocity field $\mathbf{u} : U \times [a, b] \to \mathbb{R}^n$ assumed to be smooth in its arguments.

If $\mathbf{x}(t; t_0, \mathbf{x}_0)$ denotes the trajectory of (2) passing through a point $\mathbf{x}_0$ at time t_0, the flow map $\mathbf{F}_{t_0}^t$ is defined as

$$\begin{aligned} \mathbf{F}_{t_0}^t &: U \to U \\ &\mathbf{x}_0 \mapsto \mathbf{x}(t; t_0, \mathbf{x}_0), \end{aligned} \tag{3}$$

This is as smooth as the vector field $\mathbf{u}$ [see, e.g., 47]), enabling us to define the the deformation gradient $\boldsymbol{\nabla}\mathbf{F}_{t_0}^t$ as the Jacobian of the flow map.

The flow map $\mathbf{F}_{t_0}^t$ defines a dynamical system over the phase space U. That is, for any $\mathbf{x}_0 \in U$ and $t_0, t_1, t_2 \in [a, b]$, the flow map satisfies $\mathbf{F}_{t_0}^{t_0}(\mathbf{x}_0) = \mathbf{x}_0$ and $\mathbf{F}_{t_0}^{t_2}(\mathbf{x}_0) = \mathbf{F}_{t_1}^{t_2}\mathbf{F}_{t_0}^{t_1}(\mathbf{x}_0)$. In the following, we also refer to the differential equation (2) generating the flow map $\mathbf{F}_{t_0}^t$ as a dynamical system.

The (right) Cauchy–Green strain tensor field is then defined as

$$\mathbf{C}_{t_0}^t(\mathbf{x}_0) = \left[\boldsymbol{\nabla}\mathbf{F}_{t_0}^t(\mathbf{x}_0)\right]^\top \boldsymbol{\nabla}\mathbf{F}_{t_0}^t(\mathbf{x}_0), \tag{4}$$

for any $\mathbf{x}_0 \in U$ with $\top$ referring to matrix transposition. The tensor $\mathbf{C}_{t_0}^t$ is symmetric and positive definite, and hence admits two real positive eigenvalues and orthogonal real eigenvectors. The eigenvalues λ_i and corresponding unit eigenvectors $\boldsymbol{\xi}_i$ of the tensor $\mathbf{C}_{t_0}^t$ are defined by the relations

$$\mathbf{C}_{t_0}^t(\mathbf{x}_0)\boldsymbol{\xi}_i(\mathbf{x}_0) = \lambda_i(\mathbf{x}_0)\boldsymbol{\xi}_i(\mathbf{x}_0), \qquad |\boldsymbol{\xi}_i(\mathbf{x}_0)| = 1, \qquad i = 1, 2, \cdots, n \tag{5}$$

$$0 < \lambda_1(\mathbf{x}_0) \leq \lambda_2(\mathbf{x}_0) \leq \cdots \leq \lambda_n(\mathbf{x}_0). \tag{6}$$

We suppress the dependence of λ_i and $\boldsymbol{\xi}_i$ on t_0 and t for notational simplicity.

If the flow is incompressible (i.e. $\boldsymbol{\nabla} \cdot \mathbf{u} \equiv 0$), the eigenvalues of $\mathbf{C}_{t_0}^t$ also satisfy $\prod_{i=1}^n \lambda_i(\mathbf{x}_0) = 1$ for any $\mathbf{x}_0 \in U$ [see, e.g., 47].

0.3 Terminology

In this section, we define some main objects that will be used in the following chapters. To keep each chapter self-contained, we repeat the definition of each concept as it appears in a later chapter. The motivation for such definitions also become clear in the corresponding chapter. Therefore, the present section is meant as a glossary of the main terms and concepts.

The eigenvectors $\{\boldsymbol{\xi}_k\}_{1\leq k\leq n}$ of the Cauchy–Green strain tensor define n vector fields $\boldsymbol{\xi}_k : U \to \mathbb{R}^n$ $(k = 1, 2, \cdots, n)$ on the phase space U. Let $\mathcal{M}(t)$ be a one-parameter family of smooth co-dimension one manifolds in the phase space U given by $\mathcal{M}(t) = \mathbf{F}_{t_0}^t(\mathcal{M}(t_0))$. Then we have the following definitions.

Definition 0.1 (Strain-surface)**.** The family $\mathcal{M}(t)$ is called a *strain-surface* if $\mathcal{M}(t_0)$ is everywhere orthogonal to the $\boldsymbol{\xi}_n$ vector filed. If $n = 2$, the manifold is a smooth curve, and we use the term *strainline* for curves that are everywhere orthogonal to the vector field $\boldsymbol{\xi}_2$.

Definition 0.2 (Stretch-surface)**.** The family $\mathcal{M}(t)$ is called a *stretch-surface* if $\mathcal{M}(t_0)$ is everywhere orthogonal to the $\boldsymbol{\xi}_1$ vector filed. If $n = 2$, the manifold is a smooth curve, and we use the term *stretchline* for curves that are everywhere orthogonal to the vector field $\boldsymbol{\xi}_1$.

Following [24], for a two-dimensional dynamical system ($n = 2$), we define the one-parameter family of vector fields

$$\boldsymbol{\eta}_\lambda^\pm = \sqrt{\frac{\lambda_2 - \lambda^2}{\lambda_2 - \lambda_1}}\boldsymbol{\xi}_1 \pm \sqrt{\frac{\lambda^2 - \lambda_1}{\lambda_2 - \lambda_1}}\boldsymbol{\xi}_2, \tag{7}$$

with $\lambda > 0$ being the parameter. We refer to these vector fields as the λ-*vector fields*. Note that, for a given λ, the λ-vector fields are only defined on a subset U_λ of the phase space U given by

$$U_\lambda = \{\mathbf{x} \in U : \lambda_1(\mathbf{x}) \leq \lambda^2 \leq \lambda_2(\mathbf{x})\}. \tag{8}$$

In an incompressible flow, when $\lambda = 1$, the vector fields $\boldsymbol{\eta}_1^\pm$ are well-defined over the entire phase space U. In this special case, we refer to the vector fields $\boldsymbol{\eta}_1^\pm$ as the *shear vector fields*.

Definition 0.3 (λ-lines)**.** A material line $\mathcal{M}(t)$ is called a λ-*line* if $\mathcal{M}(t_0) \subset U_\lambda$ is everywhere tangent to $\boldsymbol{\eta}_\lambda^+$ or $\boldsymbol{\eta}_\lambda^-$. In the special case $\lambda = 1$, the λ-line is referred to as a *shearline*.

As shown in Chapters 5 and 6, the λ-lines (and shearlines in particular) form the boundaries of coherent regions that preserve their overall shape as they evolve over a given finite time interval. An extension of shearlines to three-dimensional dynamical systems is given in [25].

Finally, we introduce the (largest) finite-time Lyapunov exponent (FTLE), a broadly used diagnostic tool for visualizing the Lagrangian coherent structures in unsteady flow.

Definition 0.4 (FTLE)**.** The finite-time Lyapunov exponent associated with the dynamical system (2) is the scalar field $\Lambda_{t_0}^t : U \to \mathbb{R}^+$ defined as

$$\Lambda_{t_0}^t(\mathbf{x}_0) = \frac{1}{2|t - t_0|}\log \lambda_n(\mathbf{x}_0), \tag{9}$$

where λ_n is the largest eigenvalue of the Cauchy–Green strain tensor $\mathbf{C}_{t_0}^t$.

0.4 Organization of the thesis

The following chapters are a collection of author's results that are published (or are submitted for publication) as research articles. As such, each chapter is self-contained, starting with an introduction and followed by problem formulation and results. The results are invariably illustrated with numerical examples. The notation introduced in Section 0.2 above may be slightly modified to best suit the corresponding chapter. That, however, should not be a source of confusion since the terms are explicitly defined wherever they appear.

Part I contains the main theoretical and computational results. Chapter 1 does not have substantial theoretical contributions. It, however, introduces

some main concepts and ideas. It also resolves the computational difficulties in locating Lagrangian coherent structures (LCSs). The computational framework developed in this chapter is used in subsequent chapters, with possibly slight modifications.

Chapter 2 presents a self-consistent theory of hyperbolic LCSs and investigates their relation to stable-unstable manifolds in autonomous dynamical systems.

A variational theory of shearless transport barriers (a particular type of KAM tori) is developed in Chapter 3. Based on the theory, an automated algorithm is proposed for computing such barriers.

Chapter 4 may appear out of place. It emerged from author's recent interest in the mixing of *inertial particles* in a background fluid flow. Inertial particles are small finite-size particles that are pushed around by the surrounding fluid. Because of their inertia, such particles do not simply follow fluid trajectories. Their motion is, instead, modeled by a fractional-order differential equation, with the fractional derivative (the Basset force) modeling the diffusion of vorticity around the particle. As such, many fundamental questions are unanswered about the equations of motion of inertial particles. Chapter 4 addresses some of these questions, namely the existence, uniqueness and regularity of solutions.

The numerical examples of Part I serve the purpose of illustrating the application of the corresponding theory and algorithms. In part II, however, we use Lagrangian coherent structures to investigate specific problems. Chapter 5 is dedicated to a Lagrangian study of coherent vortices in the numerical solutions of two-dimensional Navier–Stokes equation. While most previous numerical examples are concerned with fluid flows, Chapter 6 demonstrates the application of Lagrangian coherent structures to the study of mechanical systems.

The list of publications on which each chapter is based follows:

- Chapter 1: *Computing Lagrangian coherent structures from their variational theory*, M. Farazmand & G. Haller, Chaos, vol. 22, pp. 013128, 2012 [48]

- Chapter 2: *Attracting and repelling Lagrangian coherent structures from a single computation*, M. Farazmand & G. Haller, Chaos, vol. 23, pp. 023101, 2013 [49]

- Chapter 3: *Shearless transport barriers in unsteady two-dimensional flows and maps*, M. Farazmand, D. Blazevski & G. Haller, Physica D, in press, 2014 [50]

- Chapter 4: *The Maxey-Riley equation: Existence, uniqueness and regularity of solutions*, M. Farazmand & G. Haller, Submitted [51]

- Chapter 5: *How coherent are the vortices of two-dimensional turbulence?*, M. Farazmand & G. Haller, Submitted [52]

- Chapter 6: *Detecting invariant manifolds, attractors and generalized KAM*

tori in aperiodically forced mechanical systems[2], A. Hadjighasem, M. Farazmand & G. Haller, Nonlinear Dynamics, vol. 73, pp. 689-704, 2013 [53]

[2]Contributions: The author (M. Farazmand) provided the original codes over which the first author (A. Hadjighasem) has improved upon for the purposes of this publication. All authors contributed to designing the numerical experiments and writing the manuscript.

Part I

Lagrangian Coherent Structures: Theory and Computation

Chapter 1

Computational aspects

1.1 Introduction

Lagrangian Coherent Structures (LCSs) are skeletons of observed tracer patterns in dynamical systems, such as those describing the evolution of fluid particles in a two-dimensional physical domain. While such centerpieces of trajectory patterns have been well understood for steady and time-periodic flows (see, e.g., Ottino [54]), exploring similar structures in unsteady flows with general time dependence, especially over a finite time-interval, has been an ongoing effort.

A number of diagnostic tools have been proposed to interpret Lagrangian pattern formation in general unsteady flows (see, e.g., Provenzale [55], Boffetta et al. [56], and Peacock and Dabiri [57] for reviews). Among these, finite-time Lyapunov exponents (FTLE) have enjoyed broad popularity in recent years, with ridges of the FTLE field routinely considered as indicators of hyperbolic (i.e., attracting or repelling) LCSs (Haller [22] and Shadden et al. [7]). A closer look, however, reveals that FTLE ridges can produce both false positives and negatives in LCS detection even in simple two-dimensional steady flows, let alone in complex data sets (Haller [44]).

Using LCSs for reliable now-casting and forecasting requires sufficient and necessary conditions that are backed by mathematical theorems. Such conditions were recently obtained in Haller [44], where the original definition of hyperbolic LCSs as locally most repelling or attracting surfaces (see Haller and Yuan [21]) was explored further analytically. Solving this extremum problem, Haller [44] derived a variational LCS theory that provides sufficient and necessary conditions for hyperbolic LCSs in terms of the invariants of the Cauchy–Green strain tensor. For the first time, this theory separates material surfaces generating exponential stretching from those generating shear in a frame-independent fashion, thereby offering a rigorous alternative to previously proposed diagnostic quantities.

In this chapter, we develop a numerical algorithm that implements the variational LCS theory of Haller [44] and Farazmand and Haller [45] for two-

dimensional flows defined over a finite time-interval. The algorithm described here captures hyperbolic LCSs as smoothly parametrized material lines, obtained as trajectories of an autonomous ordinary differential equation for the tensor lines of the Cauchy–Green strain tensor field. We illustrate this variational LCS computation on a model flow and on a velocity field obtained from a two-dimensional turbulence simulation.

1.2 Set-up

We start by recalling the notation and definitions from Haller [44] for the case of two-dimensional flows. We consider dynamical systems of the form

$$\dot{\mathbf{x}} = \mathbf{v}(\mathbf{x}, t), \quad \mathbf{x} \in U, \quad t \in [\alpha, \beta], \tag{1.1}$$

with U denoting an open, bounded subset of $\mathbb{R}^2$, with the the time t varying over the finite interval $[\alpha, \beta]$, and with the two-dimensional velocity field $\mathbf{v}$ assumed to be smooth in its arguments.

If $\mathbf{x}(t, t_0, \mathbf{x}_0)$ denotes the trajectory of (1.1) passing through a point $\mathbf{x}_0$ at time t_0, then the flow map is defined as

$$\mathbf{F}_{t_0}^{t}(\mathbf{x}_0) := \mathbf{x}(t; t_0, \mathbf{x}_0).$$

This is as smooth as the vector field $\mathbf{v}$ (see, e.g., Arnold [47]), enabling us to define the Cauchy–Green strain tensor field as

$$\mathbf{C}_{t_0}^{t_0+T}(\mathbf{x}_0) = \left(\boldsymbol{\nabla}\mathbf{F}_{t_0}^{t_0+T}(\mathbf{x}_0)\right)^{*} \boldsymbol{\nabla}\mathbf{F}_{t_0}^{t_0+T}(\mathbf{x}_0), \tag{1.2}$$

with $\boldsymbol{\nabla}\mathbf{F}_{t_0}^{t_0+T}$ denoting the Jacobian of $\mathbf{F}_{t_0}^{t_0+T}$, and with the star referring to matrix transposition. The tensor $\mathbf{C}_{t_0}^{t_0+T}$ is symmetric and positive definite, and hence admits two real positive eigenvalues and orthogonal real eigenvectors. The eigenvalues λ_i and corresponding unit eigenvectors $\boldsymbol{\xi}_i$ of the tensor $\mathbf{C}_{t_0}^{t_0+T}$ are defined by the relations

$$\mathbf{C}_{t_0}^{t_0+T}(\mathbf{x}_0)\boldsymbol{\xi}_i(\mathbf{x}_0) = \lambda_i(\mathbf{x}_0)\boldsymbol{\xi}_i(\mathbf{x}_0), \qquad |\xi_i(\mathbf{x}_0)| = 1, \qquad i = 1, 2,$$

$$0 < \lambda_1(\mathbf{x}_0) \leq \lambda_2(\mathbf{x}_0). \tag{1.3}$$

We suppress the dependence of λ_i and $\boldsymbol{\xi}_i$ on t_0 and T for notational simplicity.

If the flow is incompressible (i.e. $\boldsymbol{\nabla} \cdot \mathbf{v} \equiv 0$), the eigenvalues of $\mathbf{C}_{t_0}^{t_0+T}$ also satisfy $\lambda_1(\mathbf{x}_0)\lambda_2(\mathbf{x}_0) = 1$ for any $\mathbf{x}_0 \in U$ (see Arnold [47]).

1.2.1 LCSs as most attracting or repelling material surfaces

The variational LCS theory in Haller [44] seeks special material surfaces that act as organizing centers of observed trajectory patterns. Such material surfaces

distinguish themselves by attracting or repelling nearby trajectories at locally the highest rate in the flow.

To quantify normal attraction and repulsion, consider a smooth curve $\mathcal{M}(t_0)$ at time t_0, which is advected by the flow map into a time-evolving material line $\mathcal{M}(t) = \mathbf{F}_{t_0}^t(\mathcal{M}(t_0))$. At each point $\mathbf{x}_0 \in \mathcal{M}(t_0)$, we may select a unit normal $\mathbf{n}_0$ to $\mathcal{M}(t_0)$ and monitor its evolution under the linearized flow map $\boldsymbol{\nabla}\mathbf{F}_{t_0}^t(\mathbf{x}_0)$. To measure how strongly repelling the material line $\mathcal{M}(t_0)$ is, we denote the length of the surface-normal component of the advected vector $\boldsymbol{\nabla}\mathbf{F}_{t_0}^t(\mathbf{x}_0)\mathbf{n}_0$ by $\rho_{t_0}^t(\mathbf{x}_0, \mathbf{n}_0)$, as shown in Fig. 1.1. We refer to $\rho_{t_0}^t(\mathbf{x}_0, \mathbf{n}_0)$ as the *normal repulsion rate* of $\mathcal{M}(t)$ along the trajectory $\mathbf{x}(t, t_0, \mathbf{x}_0)$.

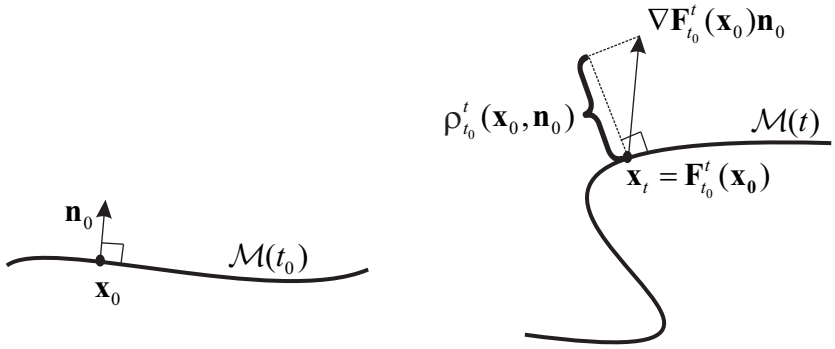

Figure 1.1: The definition of the repulsion rate $\rho_{t_0}^t(\mathbf{x}_0, \mathbf{n}_0)$ at an initial point $\mathbf{x}_0$ of a material line $\mathcal{M}(t)$. The vector $\mathbf{n}_0$ denotes a unit normal to $\mathcal{M}(t_0)$ at $\mathbf{x}_0$.

If $\rho_{t_0}^{t_0+T}(\mathbf{x}_0, \mathbf{n}_0) > 1$ holds, then $\mathcal{M}(t)$ has been overall repelling between t_0 and t_0+T along the trajectory that started from $\mathbf{x}_0$. Similarly, $\rho_{t_0}^{t_0+T}(\mathbf{x}_0, \mathbf{n}_0) < 1$ implies that $\mathcal{M}(t)$ has been overall attracting along the trajectory starting from $\mathbf{x}_0$.

As shown in Haller [44], the normal repulsion rate can be computed in terms of the Cauchy-Green strain tensor as

$$\rho_{t_0}^{t_0+T}(\mathbf{x}_0, \mathbf{n}_0) = \frac{1}{\sqrt{\left\langle \mathbf{n}_0, \left[\mathbf{C}_{t_0}^{t_0+T}(\mathbf{x}_0)\right]^{-1} \mathbf{n}_0 \right\rangle}}, \tag{1.4}$$

where $\langle \cdot, \cdot \rangle$ denotes the Euclidean inner product.

Using this normal repulsion rate, the main LCS definitions from Haller [44] can be summarized as follows:

- *A normally repelling material line* over $[t_0, t_0 + T]$ is a compact material line segment $\mathcal{M}(t)$ on which the normal repulsion rate satisfies

$$\rho_{t_0}^{t_0+T}(\mathbf{x}_0, \mathbf{n}_0) > 1, \qquad \rho_{t_0}^{t_0+T}(\mathbf{x}_0, \mathbf{n}_0) > \left|\boldsymbol{\nabla}\mathbf{F}_{t_0}^{t_0+T}(\mathbf{x}_0)\mathbf{e}_0\right|$$

for any initial point $\mathbf{x}_0 \in \mathcal{M}(t_0)$ and with unit tangent vector $\mathbf{e}_0$ to $\mathcal{M}(t_0)$ at $\mathbf{x}_0$. The second inequality here requires any possible tangential growth within $\mathcal{M}(t)$ to be less than the growth normal to $\mathcal{M}(t)$ over the time interval $[t_0, t_0 + T]$.

- *A repelling LCS* over $[t_0, t_0+T]$ is a normally repelling material line $\mathcal{M}(t)$ whose normal repulsion rate admits a pointwise non-degenerate maximum along $\mathcal{M}(t_0)$ among all locally C^1-close material surfaces. (cf. Fig. 1.2).
- An *attracting LCS* over $[t_0, t_0 + T]$ is defined as a repelling LCS over the backward time interval $[t_0 + T, t_0]$.
- Finally, a *hyperbolic LCS* over $[t_0, t_0 + T]$ is a repelling or attracting LCS over the same time interval.

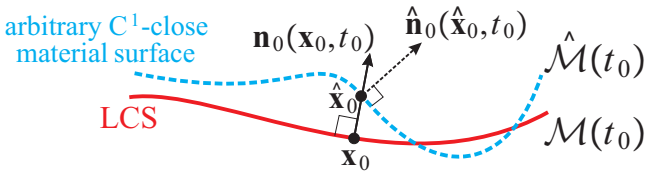

$$\rho_{t_0}^{t_0+T}(\hat{\mathbf{x}}_0, \hat{\mathbf{n}}_0) < \rho_{t_0}^{t_0+T}(\mathbf{x}_0, \mathbf{n}_0)$$

Figure 1.2: Geometry of a repelling LCS as a material line $\mathcal{M}(t_0)$ that pointwise maximizes the repulsion rate $\rho_{t_0}^{t_0+T}(\mathbf{x}_0, \mathbf{n}_0)$ relative to any nearby material line $\hat{\mathcal{M}}(t_0)$.

By the above definitions, a material line is a hyperbolic LCS over a finite time interval I if it is locally the most repelling or attracting over I among all nearby material lines. Hence, an LCS is always associated with a time interval I over which the underlying dynamical system is known, or over which specific questions about the evolution of tracers are to be answered. There is no *a priori* reason why LCSs obtained over one time interval I should continue to exist over different time intervals, unless those intervals are small perturbations of I. Indeed, small perturbations to I translate to small perturbations to the repulsion rate, under which an LCS–as a compact and strict local maximizer of the the repulsion rate–will persist.

We now recall the main existence result on LCSs (Haller [44] and Farazmand and Haller [45]), stated here specifically for two-dimensional flows. We will use the notation $\mathbf{a} \perp \gamma$ to express that a vector field $\mathbf{a}$ is normal to a curve γ at each point of γ.

Theorem 1.1. *[Sufficient and necessary conditions for LCSs in two-dimensional flows] Consider a compact material line $\mathcal{M}(t) \subset U$ evolving over the interval $[t_0, t_0 + T]$. Then $\mathcal{M}(t)$ is a repelling LCS over $[t_0, t_0 + T]$ if and only if all the following hold for all initial conditions $\mathbf{x}_0 \in \mathcal{M}(t_0)$:*

1. $\lambda_1(\mathbf{x}_0) \neq \lambda_2(\mathbf{x}_0) > 1$;
2. $\langle \boldsymbol{\xi}_2(\mathbf{x}_0), \boldsymbol{\nabla}^2 \lambda_2(\mathbf{x}_0) \boldsymbol{\xi}_2(\mathbf{x}_0) \rangle < 0$;
3. $\boldsymbol{\xi}_2(\mathbf{x}_0) \perp \mathcal{M}(t_0)$;
4. $\langle \nabla \lambda_2(\mathbf{x}_0), \boldsymbol{\xi}_2(\mathbf{x}_0) \rangle = 0$.

Condition 1 ensures that the normal repulsion rate $\rho_{t_0}^{t_0+T}(\mathbf{x}_0, \mathbf{n}_0)$ is larger than tangential stretch due to shear along the LCS. Conditions 3 and 4 together guarantee that $\rho_{t_0}^{t_0+T}$ attains a local extremum along the LCS relative to all C^1-close material lines. Finally, condition 2 ensures that this extremum is a stirct local maximum.

To relate this general result to the frequently used FTLE field $\sigma(\mathbf{x}_0) = \frac{1}{2|T|} \log \lambda_2(\mathbf{x}_0)$, note that conditions (2) and (4) are satisfied along height ridges of the $\sigma(\mathbf{x}_0)$ field [44]. Therefore, by Theorem 1.1, such a height ridge of $\sigma(\mathbf{x}_0)$ is a repelling LCS if and only if the remaining two conditions of the theorem hold, i.e.: (1) the values of σ are strictly positive along the ridge, and the minimal and maximal finite-time Lyapunov exponents are not equal along the ridge; (3) the ridge is pointwise normal to the maximal strain eigenvector field $\boldsymbol{\xi}_2(\mathbf{x}_0)$ (see Haller [44] and Farazmand and Haller [45] for details).

Theorem 1.1, however, does *not* say that all LCSs are ridges of the FTLE field, nor that all FTLE ridges mark LCSs. Indeed, simple examples in Haller [44] show that both of these statements would be incorrect even in steady flows (cf. Haller [44]).

1.2.2 Reformulated LCS criterion for numerical implementation

Finding the zero set of the inner product in condition 4 of Theorem 1.1 tends to be numerically sensitive, which prompts us to reformulate this condition in a way that allows robust implementation. Inspecting the proof of Theorem 1.1 in Haller [44], we find that condition 4 serves as a necessary condition for the repulsion rate to attain a maximum on the LCS with respect to locally normal translations in the direction of $\boldsymbol{\xi}_2$. Indeed, the directional derivative of the repulsion rate along the vector field $\boldsymbol{\xi}_2(\mathbf{x}_0)$ vanishes if

$$\frac{d}{d\varepsilon} \rho_{t_0}^{t}(\mathbf{x}_0 + \varepsilon \boldsymbol{\xi}_2, \boldsymbol{\xi}_2)|_{\varepsilon=0} = \frac{1}{2\sqrt{\lambda_2(\mathbf{x}_0)}} \langle \boldsymbol{\nabla} \lambda_2(\mathbf{x}_0), \boldsymbol{\xi}_2(\mathbf{x}_0) \rangle = 0, \tag{1.5}$$

which is equivalent to condition 4 of Theorem 1.1.

Motivated by this observation and by the fact that $\rho_{t_0}^{t}(\mathbf{x}_0, \boldsymbol{\xi}_2(\mathbf{x}_0)) = \sqrt{\lambda_2(\mathbf{x}_0)}$, we relax condition 4 of Theorem 1.1 by requiring that the average of λ_2 along $\mathcal{M}(t_0)$ be locally the largest among all nearby curves that are normal to the vector field $\boldsymbol{\xi}_2(\mathbf{x}_0)$. We also relax condition 2 of the theorem from a strict inequality to one that allows equality as well. This means that we allow an LCS to have finite thickness, but insist that it has a uniquely defined local orientation. Finally, using the orthogonality of the eigenvectors $\boldsymbol{\xi}_2(\mathbf{x}_0)$ and $\boldsymbol{\xi}_1(\mathbf{x}_0)$, we

give an equivalent form of condition 3 that will prove helpful for computational purposes.

The reformulated set of conditions obtained in this fashion are of the form [(A)]

1. $\lambda_1(\mathbf{x}_0) \neq \lambda_2(\mathbf{x}_0) > 1$;
2. $\left\langle \boldsymbol{\xi}_2(\mathbf{x}_0), \boldsymbol{\nabla}^2\lambda_2(\mathbf{x}_0)\boldsymbol{\xi}_2(\mathbf{x}_0)\right\rangle \leq 0$;
3. $\boldsymbol{\xi}_1(\mathbf{x}_0) \parallel \mathcal{M}(t_0)$;
4. $\bar{\lambda}_2(\gamma)$, the average of λ_2 over a curve γ, is maximal on $\mathcal{M}(t_0)$ among all nearby curves γ satisfying $\gamma \parallel \boldsymbol{\xi}_1(\mathbf{x}_0)$.

Relaxing Theorem 1.1 in this fashion is consistent with numerical and laboratory observations of tracer mixing in two-dimensional, time-periodic flows. In such flows, over long enough time intervals, tracers have been observed to form striations with a clearly defined local orientation [see, e.g., 54, 58]. This strict local orientation in the direction of the $\boldsymbol{\xi}_1(\mathbf{x}_0)$ field is still enforced by condition (C) despite the relaxed nature of conditions (B) and (D).

Observe that the relaxed conditions (A)-(D) are efficient enough to allow for the detection of LCSs even in linear flows. For instance, in the saddle-type linear velocity field $\dot{x} = x$, $\dot{y} = -y$, all horizontal lines qualify as attracting LCSs. Indeed, the eigenvalues and eigenvectors of the backward-time Cauchy-Green strain tensor field satisfy $\lambda_2(\mathbf{x}_0) \equiv e^T$ and $\boldsymbol{\xi}_2(\mathbf{x}_0) \equiv (0, 1)$, implying that conditions (A)-(D) hold on any horizontal line $\mathcal{M}(t_0)$. When advected by the flow, any such line will be observed as an attractor for nearby tracer blobs that spread out horizontally, while becoming thinner and thinner vertically. This is to be contrasted with the well-known inability of heuristic Lagrange diagnostic tools (such as plots of FTLE or finite-size Lyapunov exponents) to explain tracer patterns in flows with constant maximal Lyapunov exponents (see Haller[44] for further examples).

1.3 Numerical challenges of LCS detection

According to condition (C), hyperbolic LCSs are formed by material curves that are tangent to the $\boldsymbol{\xi}_1(\mathbf{x}_0)$ vector field, the eigenvector field associated with the smaller eigenvalue field $\lambda_1(\mathbf{x}_0)$ of the Cauchy-Green strain tensor field $\mathbf{C}_{t_0}^{t_0+T}(\mathbf{x}_0)$.

Curves that are everywhere tangent to the larger eigenvector field of a two-dimensional tensor field have traditionally been called tensor lines in scientific visualization (see, e.g., Tricoche et al. [59]). In order to distinguish the tensor lines tangent to $\boldsymbol{\xi}_1$ from those tangent to $\boldsymbol{\xi}_2$, we refer to the lines tangent to $\boldsymbol{\xi}_1(\mathbf{x}_0)$ as *strainlines* computed over the $[t_0, t_0 + T]$ time interval. The subspace $S_{\mathbf{x}_0}$ spanned by the eigenvector $\boldsymbol{\xi}_1(\mathbf{x}_0)$ is referred to as the *strain direction* at the point $\mathbf{x}_0$.

1.3.1 Numerical challenges in computing strainlines

Based on our discussion in Section 1.2.2, hyperbolic LCSs are captured numerically as the subset of all strainlines that satisfy the relaxed conditions (A), (B) and (D) of Theorem 1.1.

The following challenges arise in the numerical computation of strainlines:

(i) *Sensitivity of the strain directions:* The eigenvectors of the Cauchy–Green strain tensor are sensitive to numerical errors. This sensitivity is even more pronounced near hyperbolic LCSs, because large deviations in nearby particles lead to large errors in the computation of the entries of the Cauchy–Green strain tensor (see figure 1.3a). Since the conditions (A)-(D) need to be verified precisely near LCSs, the strain eigenvectors must be calculated accurately.

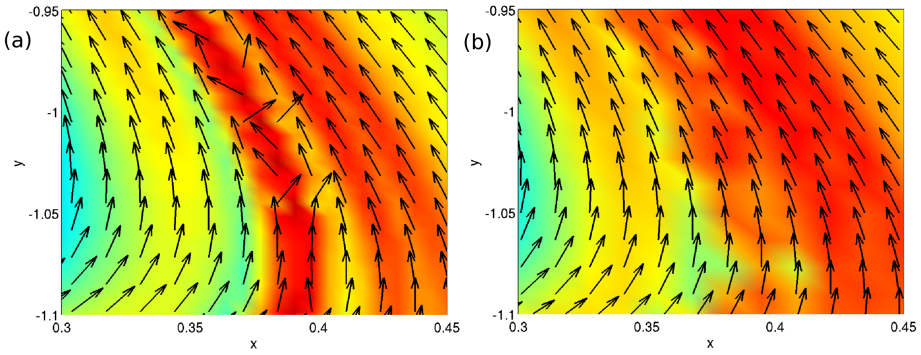

Figure 1.3: (a) Computation of strain eigenvectors for the periodically forced Duffing oscillator near a repelling LCS, calculated over 670×670 grid points in the domain $[-2\ 2] \times [-2\ 2]$ (b) For the same computational effort, use of an auxiliary grid around a sparser initial grid returns more accurate results. The background color is the FTLE field in both plots. Note the loss of resolution for the FTLE field on the sparser grid, while the accuracy of the strain directions has increased

(ii) *Degenerate points:* The points at which the two eigenvalues of the tensor field $\mathbf{C}_{t_0}^{t}(\mathbf{x}_0)$ are equal, i.e., $\lambda_1 = \lambda_2$, are referred to as degenerate points of the tensor field (see Delmarcelle and Hesselink [60]). At such points, $\mathbf{C}_{t_0}^{t}(\mathbf{x}_0)$ becomes a scalar multiple of the identity matrix, and hence $\boldsymbol{\xi}_1$ and $\boldsymbol{\xi}_2$ are ill-defined. As a result, no unique strainline exists at such a point.

(iii) *Non-orientability of strain directions*: The eigenspaces of the Cauchy-Green strain tensor define the directions of maximal and minimal local strain. The orientation of the unit eigenvectors $\boldsymbol{\xi}_1$ and $\boldsymbol{\xi}_2$ within

these subspaces, however, is not uniquely defined. Away from degenerate points, the unit strain eigenvectors can be chosen smoothly varying over open subsets of U. This follows from general results on the parallelizability of vector fields away from their zeros (see, e.g., Arnold [47]). Globally over U, however, the $\boldsymbol{\xi}_1$ and $\boldsymbol{\xi}_2$ vector fields may admit orientational discontinuities, i.e., along curves in the plane, the orientation of the vector field reverses (see, e.g., Fig. 1.4). Such orientational discontinuities are seldom removable globally; removing the discontinuity locally by reversing the sign of strain eigenvectors will only shift the discontinuity elsewhere. In differential-geometric terms, a non-removable orientational discontinuity occurs for the strain directions if the vector bundle $\{(\mathbf{x}, \mathbf{u}) : \mathbf{x} \in U,\ \mathbf{u} \in S_{\mathbf{x}}\}$ is non-trivial (see Abraham, Marsden and Ratiu [61])

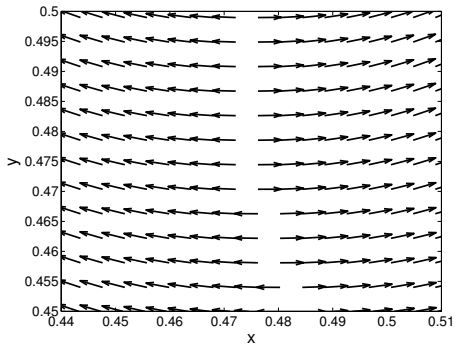

Figure 1.4: An example of an orientational discontinuity of the $\boldsymbol{\xi}_1$ field in the double-gyre example considered in section 1.5.1 below.

In the following sections, we address these computational challenges.

1.3.2 Accurate computation of strain directions

Since the location of LCSs, as defined in section 1.2.1, is not known a priori, using a denser grid near LCSs is not an option. Instead, we shall introduce a finer auxiliary grid around the original grid in order to increase the accuracy of finite differencing over the original grid.

Let $\{\mathbf{x}_j \equiv (x_j, y_j)\}_{j=1}^{N}$ denote the original computational grid over the domain U. To each grid point (x_j, y_j), we assign four neighboring points defined as

$$\begin{aligned} \mathbf{x}_j^r &= (x_j + \delta x, y_j), \quad \mathbf{x}_j^l = (x_j - \delta x, y_j), \\ \mathbf{x}_j^u &= (x_j, y_j + \delta y), \quad \mathbf{x}_j^d = (x_j, y_j - \delta y), \end{aligned} \tag{1.6}$$

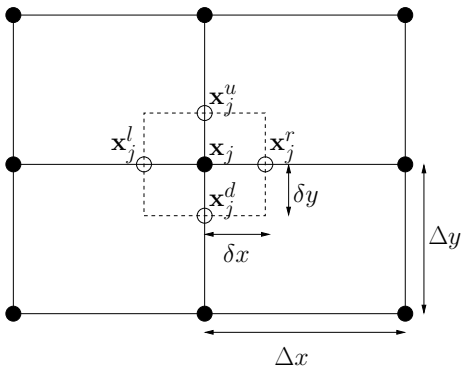

Figure 1.5: Circles indicate the auxiliary grid points used for computing the strain directions with increased accuracy; black dots represent the original grid.

where δx and δy are small increments. Figure 1.5 shows schematically the location of the auxiliary grid points (1.6).

By advecting these auxiliary points in addition to the main grid, we approximate the gradient of the flow map by finite differences as

$$\boldsymbol{\nabla} \mathbf{F}_{t_0}^{t_0+T}(\mathbf{x}_j) \approx \begin{pmatrix} \frac{\mathbf{F}_{t_0}^{t_0+T}(\mathbf{x}_j^r) - \mathbf{F}_{t_0}^{t_0+T}(\mathbf{x}_j^l)}{2\delta x} & \frac{\mathbf{F}_{t_0}^{t_0+T}(\mathbf{x}_j^u) - \mathbf{F}_{t_0}^{t_0+T}(\mathbf{x}_j^d)}{2\delta y} \end{pmatrix}. \tag{1.7}$$

Choosing δx and δy small enough will substantially increase the numerical accuracy of $\nabla \mathbf{F}_{t_0}^{t_0+T}(\mathbf{x}_j)$, and hence of the strain eigenvector $\boldsymbol{\xi}_1$.

By adding four auxiliary grid points to each point in an $N \times N$ grid of initial conditions, we need to compute a total number of $5\,(N \times N)$ trajectories instead of $N \times N$ trajectories. Therefore, in terms of computational cost, introducing the auxiliary grid is equivalent to passing to a denser grid of $\sqrt{5}N \times \sqrt{5}N$ initial conditions. At the same time, the resulting accuracy in computing $\nabla \mathbf{F}_{t_0}^{t_0+T}(\mathbf{x}_j)$ can be controlled independently by the choice of the increments δx and δy. As a result, the accuracy of finite differencing can be increased significantly by using the auxiliary grid as opposed to just passing to a uniform $\sqrt{5}N \times \sqrt{5}N$ grid.

Figure 1.3 illustrates the improvement in the $\boldsymbol{\xi}_1$-field obtained from the use of an auxiliary grid. Figure 1.3a shows the $\boldsymbol{\xi}_1$-field calculated on a uniform base grid of size 670×670, with spacing $\Delta x = \Delta y \approx 0.006$. The computation time in this case is $32.69s$. In figure 1.3b, the same $\boldsymbol{\xi}_1$-field is calculated by adding an auxiliary grid to a sparser base grid of size 300×300, with spacing $\Delta x = \Delta y \approx 0.013$. The spacing between the auxiliary grid points is $\delta x = \delta y = 10^{-5}$. The computation time in this case is $32.44s$, i.e., slightly less than in the case of the denser base grid. The noise apparent in the case of the uniform base grid (Fig. 1.3a) is fully removed, while the computational cost remains the same.

Note that we do not require the original grid to be uniform; the same approach works on unstructured grids as well. We also add that, in our experience,

the spatial distribution of $\lambda_1(\mathbf{x})$ is more noisy than that of $\lambda_2(\mathbf{x})$, even if the same numerical grid and the same explicit eigenvalue formula is used in their computation. Since these numerical errors translate to errors in the computed eigenvectors, we propose computing $\boldsymbol{\xi}_2(\mathbf{x})$ first, then obtaining $\boldsymbol{\xi}_1$ as a unit vector perpendicular to $\boldsymbol{\xi}_2$.

As was pointed out by Lekien and Ross [39], using the auxiliary grid for calculating the eigenvalues of the Cauchy–Green strain tensor is not suitable for measuring the amount of local repulsion (or attraction) of the material lines. This is due to the fact that the auxiliary grids $(\mathbf{x}_j^r, \mathbf{x}_j^u, \mathbf{x}_j^l, \mathbf{x}_j^d)$ around a main grid point $\mathbf{x}_j$ tend to lay on the same side of an LCS because of the small spacings δx and δy. As a result, the auxiliary grids undergo much less stretching compared to the main grid points that lay on different sides of a repelling LCS. Motivated by this observation, we compute the eigenvalues λ_1 and λ_2 using the uniform grid.

1.3.3 Computing smooth strainlines

By definition, strainlines are everywhere tangent to the unit strain eigenvector field $\boldsymbol{\xi}_1$. Away from repeated eigenvalues and orientational discontinuities, therefore, strainlines can be computed as smooth trajectories of the ODE

$$\mathbf{r}' = \boldsymbol{\xi}_1(\mathbf{r}), \qquad |\boldsymbol{\xi}_1(\mathbf{r})| = 1. \tag{1.8}$$

By introducing an appropriate rescaling, we alter this ODE in a fashion so that its numerical solution yields a globally smooth set of strainlines. To achieve this, we follow the scaling suggested in Tchon et al. [62] for general tensor lines by letting

$$\begin{aligned} \mathbf{r}'(s) &= \mathbf{f}\left(\mathbf{r}(s), \mathbf{r}'(s-\Delta)\right), \\ &= \operatorname{sign}\langle \boldsymbol{\xi}_1(\mathbf{r}(s)), \mathbf{r}'(s-\Delta)\rangle\, \alpha(\mathbf{r}(s))\boldsymbol{\xi}_1(\mathbf{r}(s)), \end{aligned} \tag{1.9}$$

where $\Delta > 0$ is the numerical stepsize used in integrating (1.9), and the scalar field $\alpha(\mathbf{x}_0)$ is defined as

$$\alpha(\mathbf{x}_0) = \left(\frac{\lambda_2(\mathbf{x}_0) - \lambda_1(\mathbf{x}_0)}{\lambda_2(\mathbf{x}_0) + \lambda_1(\mathbf{x}_0)}\right)^2. \tag{1.10}$$

The scaling factor $\alpha(\mathbf{x}_0)$ vanishes at degenerate points ($\lambda_1 = \lambda_2$), turning these points into fixed points (trivial strainlines). In addition, the factor $\operatorname{sign}\langle \boldsymbol{\xi}_1(\mathbf{r}(s)), \mathbf{r}'(s-\Delta)\rangle$ in (1.9) locally reverses the orientation of the vector field $\boldsymbol{\xi}_1(\mathbf{r})$ along the strainline $\mathbf{r}(s)$, if needed, for smooth integration through orientational discontinuities.

1.3.4 Extraction of hyperbolic LCSs from strainlines

If $\mathcal{M}(t_0)$ lies within a strainline, then it automatically satisfies condition (C). The strainline segments along which the further conditions (A), (B) and (D) of

section 1.2.2 are also satisfied constitute the set of hyperbolic LCSs in the flow over the time interval $[t_0, t_0 + T]$.

The simplest approach to extracting this set of LCSs is to identify the subset $U_0 \subset U$ on which conditions (A) and (B) hold, then integrate system (1.9) from initial grid points lying in U_0 to construct strainlines. This integration proceeds, in principle, until each strainline reaches the boundary of the domain U, or approaches a fixed point of (1.9) (i.e., a degenerate point of the original $\boldsymbol{\xi}_1$ vector field).

In most cases, however, only a segment of a strainline will be a hyperbolic LCS. Therefore, integration of a given strainline can be stopped when one of the LCS conditions (A) or (B) fails. Numerical noise may cause such failures at isolated points of the strainlines. To avoid such accidental failures, we choose to stop the strainline integration when an LCS condition fails repeatedly over a pre-set length ℓ_f of the strainline.

Having located the strainlines segments satisfying conditions (A) and (B), it remains to identify the strainlines segments that are local maximizers of the averaged maximum strain, as required by condition (D). The simplest way of doing this is to define a set L of uniformly spaced horizontal and vertical lines within the domain U_0, and compare the values of $\bar{\lambda}_2(\gamma_0)$, the average of λ_2 on the curve γ_0, at the neighboring intersections of all close enough strainline segments along each line in L. Intersections of the strainlines with the lines in the set L are found through linear interpolation.

If a strainline segment is found to be a local maximizer along at least one line in L, that strainline segment is labeled as an LCS (see Fig. 1.6). Adjacent intersections whose distance is larger than a preselect threshold, such as those encircled in Fig. 1.6 by a dashed ellipse, are excluded from the local maximization process.

Finally, small-scale LCSs are expected to have a negligible effect on overall pattern formation in the flow. To filter out such small structures from our computations, we discard the LCSs that are shorter than a pre-set small length ℓ_{min}.

1.3.5 Summary of variational LCS extraction algorithm in two dimensions

In Table 1, we summarize the main steps of our variational LCS extraction algorithm in the form of a pseudo code. Note that if the hyperbolic LCSs are computed over a time interval $[t_0, t_0 + T]$, then repelling LCSs will be obtained at time $t = t_0$, while attracting LCSs will be identified at $t = t_0 + T$. Thus additional advection of the attracting LCSs back to $t = t_0$ is required to obtain both attracting and repelling LCSs at the same time.

% ode$[\mathbf{f}(\mathbf{x}_j), \mathbf{x}_j, \Delta]$ refers to an ODE solver that returns the next point $\mathbf{x}_{j+1}$
% along a trajectory of a vector field $\mathbf{f}(\mathbf{x})$, given the current point $\mathbf{x}_j$ and the stepsize Δ
%
% int$[\lambda, \mathbf{R}, \Delta]$ refers to a function that computes the integral of a scalar field λ
% over a planar curve whose adjacent points are the columns of a matrix $\mathbf{R}$;
% the arclength increment is Δ

- fix a grid $\mathcal{G} \subset U$ of initial conditions;
- fix finite time interval $[t_0, t]$ of interest;
- compute the Cauchy-Green strain tensor $\mathbf{C}_{t_0}^{t}(\mathbf{x}_0)$ for all $\mathbf{x}_0 \in \mathcal{G}$;
- compute maximal strain eigenvalue $\lambda_2(\mathbf{x}_0)$ and corresponding unit eigenvector $\boldsymbol{\xi}_2(\mathbf{x}_0)$ for all $\mathbf{x}_0 \in \mathcal{G}$;
- determine sub-grid $\mathcal{G}_0 = \mathcal{G} \cap U_0$ where U_0 is the set over which conditions (A) and (B) hold;
- select integration step Δ along strainlines;
- fix length ℓ_f allowed for continuous failures of conditions (A) or (B) on LCSs;
- fix $\ell_{min} \geq 0$, the minimum length allowed for an LCS.;
- set $k = 0$; This counter will return the total number of strainlines computed.

for $\mathbf{r_0} \in \mathcal{G}_0$
  $k = k + 1$; $L := 0$; $n := 2$;
  $\mathbf{R}(1, k) := \mathbf{r_0}$
  $\boldsymbol{f}^{old} := \alpha(\mathbf{r}_0)\boldsymbol{\xi}_2^{\perp}(\mathbf{r}_0)$
  while $L < \ell_f$ **and** $\mathbf{r}_0 \in U$
    $\boldsymbol{f}^{new} := \alpha(\mathbf{r}_0)\boldsymbol{\xi}_2^{\perp}(\mathbf{r}_0)$
    $\boldsymbol{f}^{new} := \text{sign}\,\langle \boldsymbol{f}^{old}, \boldsymbol{f}^{new} \rangle \boldsymbol{f}^{new}$
    $\mathbf{r}$:=ode$[\boldsymbol{f}^{new}, \mathbf{r}_0, \Delta]$
    if $\mathbf{r} \notin U_0$
      $L := L + |\mathbf{R}(n-1, k) - \mathbf{r}|$
    else
      $L := 0$
    end if
    $\mathbf{R}(n, k) := \mathbf{r}$
    $\mathbf{r}_0 := \mathbf{r}$; $\boldsymbol{f}^{old} := \boldsymbol{f}^{new}$; $n := n + 1$;
  end while
  $\ell(k) = \text{int}[1, \mathbf{R}(\cdot, k), \Delta]$; $\bar{\lambda}_2(k) = \text{int}[\lambda_2, \mathbf{R}(\cdot, k), \Delta]/\ell(k)$
  for $j = 1$ **to** k
    if $(\ell(j) > \ell_{min}$ **and** $\bar{\lambda}_2(j) \geq \bar{\lambda}_2(j-1)$ **and** $\bar{\lambda}_2(j) \geq \bar{\lambda}_2(j+1))$
    % see section 1.3.4 for details
      plot $\mathbf{R}(\cdot, j)$
    end if
  end for
end for

Table 1.1: Algorithm for computing hyperbolic LCSs from their variational theory.

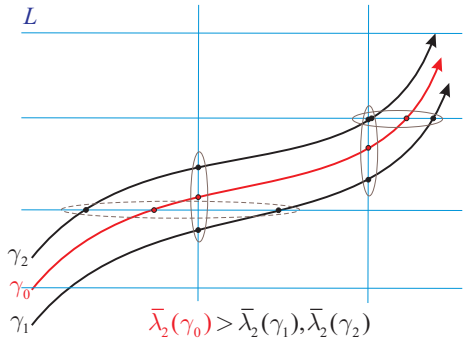

Figure 1.6: Finding local maxima of the function $\bar{\lambda}_2(\gamma)$, the average of λ_2 on the curve γ, along a set L of horizontal and vertical lines. The strainline segment γ_0 is identified as a local maximizer if it is found to have a locally maximal $\bar{\lambda}_2(\gamma)$ value along at least one line in the set L. Solid ellipses indicate adjacent points at which the values of $\bar{\lambda}_2(\gamma)$ are compared. A dashed ellipse indicates points excluded from the local maximization process because of the large distances among them.

1.4 Advection of hyperbolic LCSs as material lines

The variational theory in Haller [44] constructs LCSs as material lines, i.e., fully invariant objects with zero material flux through them. The algorithm sketched in Table 1.1 locates $\mathcal{M}(t_0)$, the $t = t_0$ slice of such an LCS. To obtain the time t slice of the LCS, we need to compute the advected material curve $\mathcal{M}(t) = \mathbf{F}_{t_0}^{t}(\mathcal{M}(t_0))$.

Advecting a locally most repelling material line is challenging, because errors in the advection will grow exponentially and therefore have to be carefully managed via highly accurate numerical integration. Numerical methods have been developed for the high-precision advection of material lines via the insertion of additional material points [63, 64]. As a rule, these methods use interpolation schemes for inserting additional points into a discreetly advected material line when the distance of its two adjacent points exceeds a threshold. This interpolation unavoidably introduces additional errors in the shape of the LCS in the advection process.

Our construction of an LCS as a parametrized trajectory of the strainline ODE (1.8) enables us to insert new points into the LCS in a dynamically consistent manner, using the underlying Lagrangian dynamics captured by the strainline field. Specifically, let γ_0 denote an LCS parametrized by $\mathbf{r} : [0, \bar{s}] \to U,\ s \mapsto \mathbf{r}(s)$. The numerical solution of (1.8) yields a discrete set of parameter values $\{s_i\}_{i=1}^{n}$ at which the set $\{\mathbf{r}(s_i)\}_{i=1}^{n}$ of LCS points has been determined. Increasing the number of points n on γ_0 (or equivalently decreasing the spacings $s_{i+1} - s_i$), increases the smoothness of the advected curve

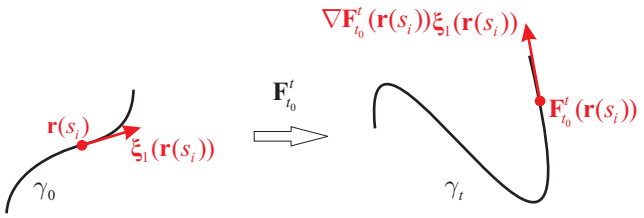

Figure 1.7: High-precision advection of an LCS, using the invariance of its tangent bundle under the linearized flow map. Note that the initial tangent vectors $\boldsymbol{\xi}_1(\mathbf{r}(s_i))$ to the LCS are exactly known from the parametrized construction of the LCS at time t_0.

γ_t.

A further increase in the accuracy of the advection of the LCS is achieved by exploiting the invariance of the tangent space of the LCS under the linearized flow. The key observation is that at a point $\mathbf{r}(s_i) \in \gamma_0$ at time t_0, the unit tangent $\boldsymbol{\xi}_1(\mathbf{r}(s_i))$ to the LCS γ_0 is *exactly* known. Therefore, at an advected point $\mathbf{F}_{t_0}^{t_0+T}(\mathbf{r}(s_i)) \in \gamma_{t_0+T}$, a tangent vector to the advected LCS γ_{t_0+T} is given by $\boldsymbol{\nabla}\mathbf{F}_{t_0}^{t_0+T}(\mathbf{r}(s_i))\boldsymbol{\xi}_1(\mathbf{r}(s_i))$, as shown in Fig. 1.4

The Jacobian $\boldsymbol{\nabla}\mathbf{F}_{t_0}^{t}(\mathbf{r}(s_i))$ can be computed locally using the auxiliary grid points introduced in section 1.3.2. Note that this requires the advection of four additional neighboring points for each point $\mathbf{r}(s_i)$ on the LCS.

A geometric Hermite interpolation scheme [65, 66] of up to 6th order can be applied to the advected LCS to utilize the above invariance property. The goal is to find a cubic polynomial $\mathbf{P} : [0,1] \to U$ satisfying

$$\begin{aligned} \mathbf{P}(0) = \tilde{\mathbf{r}}_i := \mathbf{F}_{t_0}^{t_0+T}(\mathbf{r}(s_i)), \quad \mathbf{P}(1) = \tilde{\mathbf{r}}_{i+1} := \mathbf{F}_{t_0}^{t_0+T}(\mathbf{r}(s_{i+1})), \\ \mathbf{P}'(0) \parallel \tilde{\mathbf{d}}_i := \boldsymbol{\nabla}\mathbf{F}_{t_0}^{t_0+T}(\mathbf{r}(s_i))\boldsymbol{\xi}_1(\mathbf{r}(s_i)), \quad \mathbf{P}'(1) \parallel \tilde{\mathbf{d}}_{i+1} := \boldsymbol{\nabla}\mathbf{F}_{t_0}^{t_0+T}(\mathbf{r}(s_{i+1}))\boldsymbol{\xi}_1(\mathbf{r}(s_{i+1})). \end{aligned} \tag{1.11}$$

This problem generally does not have a unique solution [66], thus additional constraints are needed to obtain a well-defined solution. Here, we use the simplest constraint introduced in Chi et. al. [65] by considering the curve with minimum length among all cubic polynomials that satisfy the constraints (1.11). Other constraints may also be employed and may potentially lead to more accurate results in specific applications.

As shown in Chi et. al. [65], a minimal length Hermite polynomial satisfies

$$\begin{aligned} \mathbf{P}(s) =& (2s+1)(s-1)^2\tilde{\mathbf{r}}_i + (3-2s)s^2\tilde{\mathbf{r}}_{i+1} + \\ & (s-1)^2 s\alpha_0\tilde{\mathbf{d}}_i + (s-1)s^2\alpha_1\tilde{\mathbf{d}}_{i+1}, \end{aligned} \tag{1.12}$$

where

$$\alpha_0 = \frac{12\langle\tilde{\mathbf{r}}_{i+1} - \tilde{\mathbf{r}}_i, \tilde{\mathbf{d}}_i\rangle\|\tilde{\mathbf{d}}_{i+1}\|^2 + 3\langle\tilde{\mathbf{r}}_{i+1} - \tilde{\mathbf{r}}_i, \tilde{\mathbf{d}}_{i+1}\rangle\langle\tilde{\mathbf{d}}_i, \tilde{\mathbf{d}}_{i+1}\rangle}{16\|\tilde{\mathbf{d}}_i\|^2\|\tilde{\mathbf{d}}_{i+1}\|^2 - \langle\tilde{\mathbf{d}}_i, \tilde{\mathbf{d}}_{i+1}\rangle^2}, \tag{1.13a}$$

$$\alpha_1 = \frac{12\langle \tilde{\mathbf{r}}_{i+1} - \tilde{\mathbf{r}}_i, \tilde{\mathbf{d}}_{i+1}\rangle \|\tilde{\mathbf{d}}_i\|^2 + 3\langle \tilde{\mathbf{r}}_{i+1} - \tilde{\mathbf{r}}_i, \tilde{\mathbf{d}}_i\rangle \langle \tilde{\mathbf{d}}_i, \tilde{\mathbf{d}}_{i+1}\rangle}{16\|\tilde{\mathbf{d}}_i\|^2 \|\tilde{\mathbf{d}}_{i+1}\|^2 - \langle \tilde{\mathbf{d}}_i, \tilde{\mathbf{d}}_{i+1}\rangle^2}. \tag{1.13b}$$

The performance of this high-accuracy LCS-advection method is illustrated in section 2.5.2.

1.5 Examples

We now demonstrate the performance of the variational LCS computation summarized in Table 1 on two unsteady velocity fields. The first is an unsteady double-gyre model that has been used extensively as a test case for locating LCSs from various indicators (see Shadden et al. [7]). The second velocity field is obtained from a direct numerical simulation of two-dimensional turbulence.

1.5.1 The double gyre

The double gyre model consists of a pair of counter-rotating gyres, with a time-periodic perturbation. As pointed out in Section 0.1, the double gyre is a perturbation of the cellular flow. The stream-function for the double gyre reads

$$\psi(x, y) = \sin(\pi f(x, t)) \sin(\pi y). \tag{1.14}$$

In terms of the planar variable $\mathbf{x} = (x, y)$, the trajectories of the system satisfy

$$\dot{\mathbf{x}} = \pi A \begin{pmatrix} -\sin(\pi f(x,t)) \cos(\pi y) \\ \cos(\pi f(x,t)) \sin(\pi y) \frac{\partial f}{\partial x} \end{pmatrix}, \tag{1.15}$$

where

$$\begin{aligned} f(x,t) &= a(t)x^2 + b(t)x, \\ a(t) &= \epsilon \sin(\omega t), \\ b(t) &= 1 - 2\epsilon \sin(\omega t). \end{aligned}$$

For our computations, we use the same parameter values as in Shadden et. al. [7], i.e., $\epsilon = 0.1$, $A = 0.1$ and $\omega = 2\pi/10$. The starting time is $t_0 = 0$ and the integration time is $T = 20$ (i.e., two forcing periods). The Cauchy–Green strain tensor is calculated on the domain $U = [0\ 2] \times [0\ 1]$ over a uniform grid $\mathcal{G}$ of 1000×500 points. As a result, the mesh size for the uniform grid is approximately $\Delta x = \Delta y = 0.002$. For computing the eigenvectors of $\mathbf{C}_{t_0}^{t_0+T}$, an auxiliary grid of size $\delta x = \delta y = 10^{-5}$ is used.

Figure 1.8 shows a set of strainlines calculated for system (1.15), with red circles indicating initial positions of the strainlines. Out of all strainlines shown in the figure, only the strainline segments satisfying conditions (A), (B) and (D) will qualify as repelling LCSs.

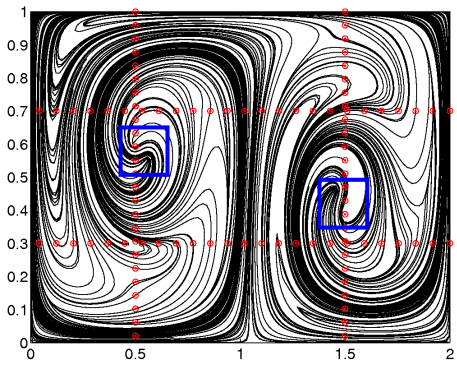

Figure 1.8: Strainlines computed for system (1.15) using the algorithm summarized in Table 1. Blue squares show the approximate location of degenerate points for the $\boldsymbol{\xi}_1$ strain vector field.

We now identify the strainline segments satisfying the LCS conditions (A) and (B) by computing the set $\mathcal{G}_0$ defined in Table 1.1. Shown in Fig. 1.9a, the set $\mathcal{G}_0$ consists of 136607 grid points.

To eliminate redundant computations within this set, we follow an approach similar to the one adopted by Lipinski and Mohseni [67] in a different context. Specifically, we reduce the set of strain initial conditions considered further from $\mathcal{G}_0$ to its intersections with a set of four horizontal and four vertical lines, as shown in Fig. 1.9b. This remaining set of strain initial conditions consists of 1422 grid points, almost two orders of magnitude less than the number of points in $\mathcal{G}_0$.

Among the strainlines initiated from the initial conditions shown in Fig. 1.9b, only the ones along which condition (D) is satisfied qualify as repelling LCSs. For instance, for the filtering parameter values $\ell_f = 0.2$ and $\ell_{min} = 1$, only the single strainline segment shown in Fig. 1.10b qualifies as a repelling LCS over the time interval $[0, 20]$.

Note that the strainline integration stops once it reaches the boundary. In order to obtain longer strainlines (and longer LCSs as a result), a slightly larger domain $U = [-0.02, 2.02] \times [-0.01, 1.01]$ is used in figure 1.10.

This well-studied example demonstrates the advantages of the variational LCS computation over simply using the FTLE field to infer the location of LCSs:

1. The FTLE field in Figure 1.10a gives an intuitive idea about the location of an LCS. By contrast, Figure 1.10b is based on a mathematical existence result (Theorem 1.1) that guarantees the existence of a repelling LCS. Note that none of the strainlines (and hence none of the LCSs) coincide precisely with the FTLE ridge. Instead, a part of an FTLE ridge that remains close to strainlines satisfying conditions (A), (B) and (D) is a good approximation for an LCS.

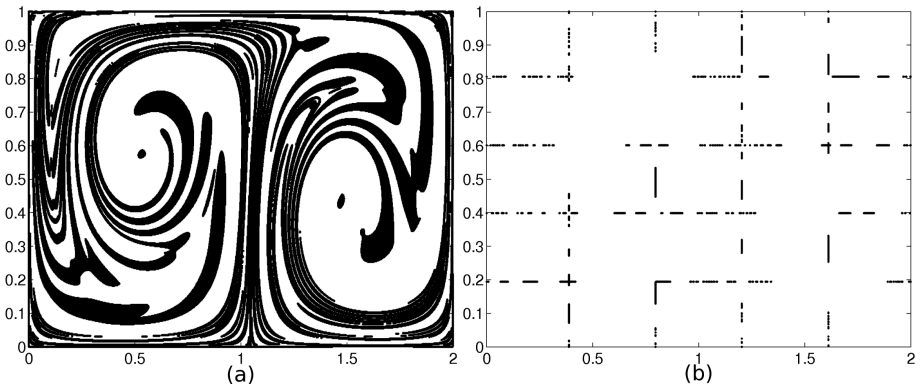

Figure 1.9: (a) The set $\mathcal{G}_0$ for the double gyre of system (1.15). (b) The intersection of the set $\mathcal{G}_0$ with four vertical and four horizontal lines.

2. The ridge of the FTLE field in Figure 1.10a is easy to recognize visually. Extracting such ridges for further analysis, however, leads to an image-processing problem that ultimately yields a set of points approximating the LCS candidate (see Lipinski and Mohseni[67] and Senatore and Ross [68]). By contrast, the strainline segment in Figure 1.10a is given in the form of a smoothly parametrized curve–a trajectory of the ODE (1.8)–with precisely defined repulsion properties. This curve can be obtained at arbitrarily high resolution by selecting a small enough stepsize Δ in solving the scaled strainline ODE (1.9).

3. Even if an FTLE ridge is not well-pronounced, as long as it correctly signals a nearby LCS, the strainlines will capture that LCS sharply. Indeed, the FTLE ridge shown in 1.10a fades away in the black rectangle, yet the corresponding LCS is captured without interruption by the strainline shown in figure 1.10b.

Similar results and conclusions hold for attracting LCSs, with the computations performed in backward time.

1.5.2 Randomly forced turbulent flow

In our second example, we test our numerical algorithm for variational LCS detection on a direct numerical simulation of two-dimensional turbulence. The velocity field $\mathbf{v}$ is obtained as the numerical solution of the modified Navier–Stokes equation

$$\partial_t \mathbf{v} + \mathbf{v} \cdot \boldsymbol{\nabla} \mathbf{v} = -\boldsymbol{\nabla} p - \nu_u \Delta^2 \mathbf{v} + \nu_i \Delta^{-1} \mathbf{v} + \mathbf{f}, \quad \boldsymbol{\nabla} \cdot \mathbf{v} = 0, \tag{1.16}$$

by a pseudo-spectral method with 1024^2 Fourier modes. We use a Krylov-subspace method [69] for temporal integration. We set the hyperviscosity as

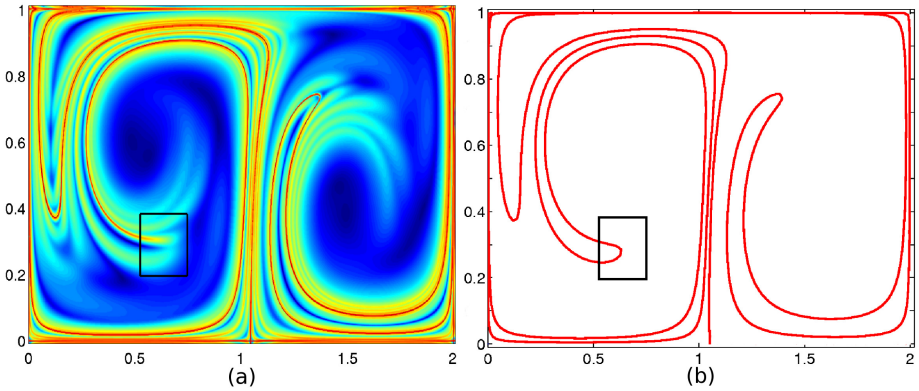

Figure 1.10: (a) The forward time FTLE field for the double-gyre model; integration time is $T = 20$. (b) The red curve is a strainline segment that qualifies as a repelling LCS by satisfying conditions (A), (B) and (D). The filtering parameters are chosen as $\ell_f = 0.2$, $\ell_{min} = 1$.

$\nu_u = 2 \times 10^{-9}$ to shift the dissipation to smaller scales while keeping the resolution relatively low. Energy is removed from large scales by the hypoviscosity $\nu_i = 1$ to prevent energy accumulation at the largest available scales. The forcing $\mathbf{f}$ is mono-scale (active at the wavenumber $k = 2$) with random phase. The amplitude of the forcing changes in time, ensuring statistically stationary state. Equation (5.7) is solved on the spatial domain $[0\ 2\pi] \times [0\ 2\pi]$ with periodic boundary conditions, over the time interval $[0\ 100]$ (see Refs. [70, 71] for similar simulations of the same equation).

The hyperbolic LCS extraction algorithm again follows Table 1.1. To implement condition (D), we fix L as a set of 20 equally spaced vertical and 20 horizontal lines. Local minima of $\bar{\lambda}_2(\gamma)$ are only kept if the neighboring strainline segments with weaker $\bar{\lambda}_2$ values are no more than 0.05 apart along the horizontal or vertical lines.

Figure 1.11 shows attracting LCSs extracted at time $t_0 = 70$ from a backward-time calculation with integration time $T = -30$ over a grid of 512×512 points.

Figure 1.12 shows the red attracting LCSs of Figure 1.11 in black, but now with the FTLE field superimposed for comparison. A closeup demonstrates how strainlines yield sharp LCSs, while the FTLE field remains blurry. More importantly, while the FTLE produces an attractive picture, its ridges tend to turn into spiraling shear maxima near vortex cores, as revealed by the inset in Figure 1.12. These ridges, therefore, constitute false predictions of hyperbolic LCSs. By contrast, the strainline segments shown in the inset satisfying conditions (A), (B) and (D), and hence are guaranteed to act as material lines shaping the skeleton of tracer patterns.

Finally, we demonstrate the performance of the advection scheme introduced in section 1.4 on this example. Figure 1.13a shows the initial location (dashed

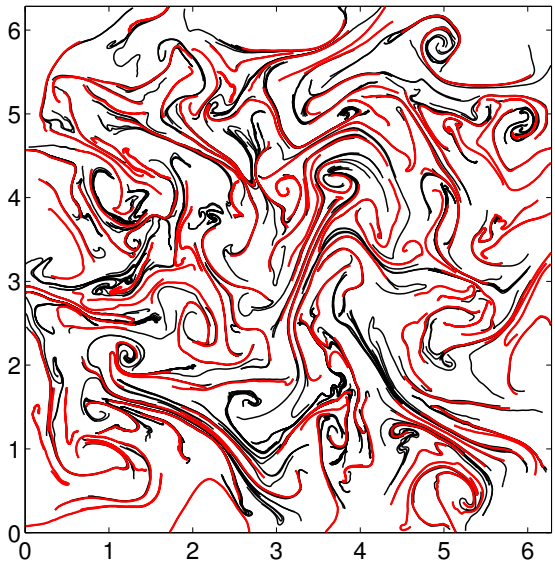

Figure 1.11: Attracting LCSs at $t_0 = 70$ with integration time $T = -30$ in the flow generated by the turbulent velocity field solving equation (5.7). The black strainline segments satisfying the LCS conditions (A) and (B) are extracted by the algorithm described in Table 1.1. The filtering parameter values in this computation are set to $\ell_f = 0.1$ and $\ell_{min} = 0.3 \max(\ell) = 1.19$. The red strainline segments also satisfy condition (D), and hence are attracting LCSs that serve as cores of tracer patterns

curve) of an attracting LCS at time $t_0 = 70$. The length of an attracting LCS shrinks exponentially in backward-time advection. As a result, comparing the performance of different interpolation schemes for inserting new points into the LCS would be challenging. For this reason, we choose to advect the LCS forward to $t = 90$. No claims about the hyperbolicity of this material line can be made over the interval $[40,\ 90]$, give that its hyperbolicity was only established over the interval $[40,\ 70]$. A total number of 222 equidistant points on the LCS are advected forward to time $t = 90$ (solid curve in figure 1.13a). Note that the number of points on the advected LCS can be arbitrarily increased by reducing the integration step size of the strainline equation (1.8).

In order to examine the Hermite interpolation scheme of section 1.4, we advect a subset of the above mentioned LCS with 23 equidistant points from time $t_0 = 70$ to $t = 90$. The Hermite interpolation (1.12) is then applied to each two consecutive points. Figure 1.13b shows the advected image of these 23 points together with the Hermite interpolant (red curve). The "ground truth" advected LCS with 222 points (black curve) is given for comparison. The blue line is the linearly interpolated curve. This example shows that the Hermite interpolation scheme introduced in section 1.4 produces a smooth curve that

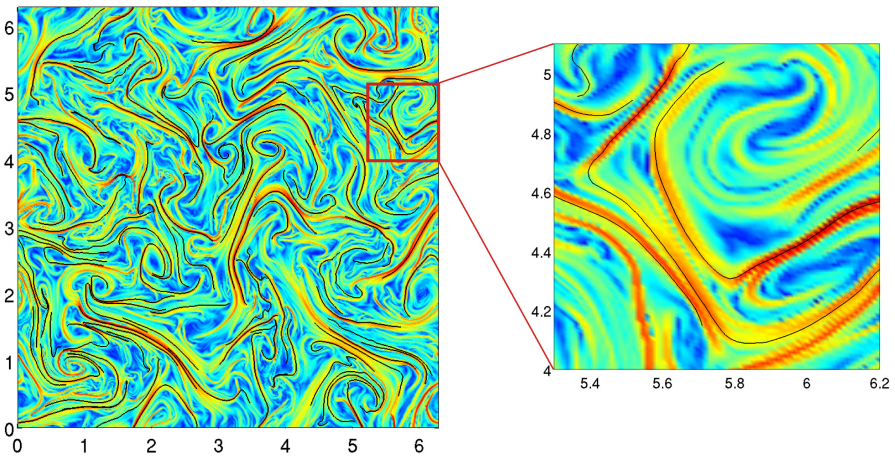

Figure 1.12: Attracting LCSs for the turbulent velocity field, with the FTLE field is shown in the background.

closely mimics the actual evolving LCS, although the interpolation is based on a sparse subset of the full LCS.

Finally, note that the error in the advected position of the LCS leads to non-zero material flux through the LCS. If the exact zero-flux property of the LCS is of importance, a sufficient number of points on the LCS must be advected with an accurate interpolation scheme to minimize this inevitable, numerically generated flux.

1.6 Conclusions

We have discussed a numerical implementation of the recent variational theory of hyperbolic Lagrangian Coherent Structures (LCSs) for two-dimensional flows (Haller [44]; Farazmand and Haller [45]). Based on exact mathematical theorems, the algorithm developed here renders attracting and repelling LCSs in the form of smoothly parametrized strainlines.

The strainlines $\mathcal{M}(t_0)$ are a subset of the tensor lines associated with the Cauchy-Green strain tensor field $\mathbf{C}_{t_0}^{t_0+T}(\mathbf{x}_0)$, and hence are trajectories of an ordinary differential equation. As ODE trajectories, the strainlines can be obtained with arbitrarily high precision at relatively low numerical cost. Well-resolved strainlines can further be advected by the flow map to yield LCSs as material lines $\mathcal{M}(t) = \mathbf{F}_{t_0}^{t}(\mathcal{M}(t_0))$. We have shown how the known tangents of $\mathcal{M}(t)$ can be used as input to a higher-order Hermite interpolation scheme that further increases the precision of LCS advection. The evolving LCS, $\mathcal{M}(t)$, obtained in this fashion is fully Lagrangian (i.e., the material flux through it

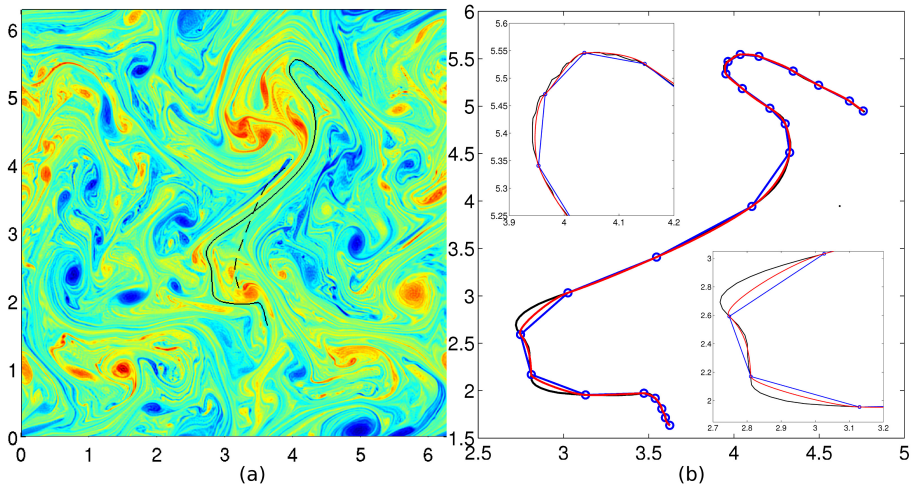

Figure 1.13: (a) An attracting LCS at time $t_0 = 70$ (dashed) and its advected image at time $t_0 + T = 90$ (solid). The vorticity field at time $t_0 + T = 90$ is given in the background. (b) Black: the advected image of the LCS with 222 points; Red: the advected image with 23 points and Hermite interpolation; Blue: the advected image with 23 points and linear interpolation. The insets show closeups of the same curves.

is zero), and acts as a core of observed mixing patterns by its locally most attracting or repelling nature.

Our approach is different from available Lagrangian diagnostic tools (FTLE, finite-size Lyapunov exponents, relative or absolute dispersion, etc), whose outputs are plots of scalar distributions (as opposed to parametrized curves) that are yet to be connected to LCSs mathematically. Such tools detect shear and strain together, and hence may produce false positives for hyperbolic behavior (cf. Haller [44] and the example in Section 2.5.2 above).

Clearly, additional effort is required in the numerical implementation of variational LCS theory compared to plotting diagnostic fields, even though the final computation times are roughly equal, given the absolute dominance of trajectory-advection in all Lagrangian calculations. In a number of applications, illustration of coherent features through diagnostic quantities is sufficient, and the details and exact nature of coherent structures, including false positives and negatives, are unimportant. By contrast, the present numerical algorithm is geared towards using LCSs in critical situations, where accurate now-casting and short-term forecasting without false positives or negatives is a must. An example is the short-term prediction of instabilities in environmental contamination patterns, such as an oil spill. In that context, the algorithm described here has delivered highly accurate short-term forecasts without any reliance

on future velocities obtained from Eulerian forecasting models (Olascoaga and Haller [72]).

The theorems in Haller [44] and Farazmand and Haller [45] are stated for general n-dimensional flows, and hence the extension of the present algorithm to higher-dimensional flows is, in principle, possible. In three-dimensional flows, for instance, the role of strainlines is taken over by two-dimensional strainsurfaces that are everywhere normal to the eigenvector field $\boldsymbol{\xi}_3(\mathbf{x})$ of the largest Cauchy-Green eigenvector field $\lambda_3(\mathbf{x})$. Strainsurfaces, however, no longer satisfy ODEs: they have to be located as solutions of a PDE. A unique solution to these PDEs is often impossible to find as pointed out by Palmerius et al. [73], but numerical algorithms providing self-consistent solutions have been developed (see, e.g., Frankot and Chellappa [74]).

Beyond a generalization to higher dimensions, the extension of the present algorithm to extract non-hyperbolic LCSs (such as shear jets and eddies) is of great practical interest. Developments in the underlying theory and computational approach will appear in Haller, Farazmand and Beron-Vera [75].

Chapter 2

Self-consistent hyperbolic Lagrangian coherent structures

2.1 Introduction

The differential equations governing a number of physical processes are only known as observational or numerical data sets. Examples include oceanic and atmospheric particle motion, whose velocity field is only known at discrete locations, evolving aperiodically over a finite time-interval of availability. For such temporally aperiodic data sets, classic dynamical concepts–such as fixed points, periodic orbits, stable and unstable manifolds or chaotic attractors–are either undefined or nongeneric.

Instead of relying on classic concepts, one may seek influential surfaces responsible for the formation of observed trajectory patterns over a finite time frame of interest. Such a surface is necessarily a material surface, i.e., a codimension-one set of initial conditions evolving with the flow. Among material surfaces, an attracting Lagrangian Coherent Structure (LCS) is defined as a locally most attracting material surface in the phase space [76, 44]. Repelling LCSs are defined as locally most repelling material surfaces, i.e., attracting LCSs in backward-time. Repelling and attracting LCSs together are referred to as hyperbolic LCSs. Both heuristic detection methods [57] and rigorous variational algorithms [44, 48, 23] are now available for their extraction from flow data.

All available hyperbolic LCS methods fundamentally seek locations of large particle separation. They will highlight repelling LCS positions at some initial time $t = a$ from a forward-time analysis of the flow over a finite time-interval $[a, b]$. Similarly, these methods reveal attracting LCSs at the final time $t = b$ from a backward-time analysis of the flow over $[a, b]$. The complete hyperbolic LCS distribution at a fixed time $t \in [a, b]$ is, therefore, not directly available.

Two main approaches have been employed to resolve this issue (see figure 2.1 for an illustration):

1. Approach I: Divide the finite time interval of interest as $[a, b] = [a, t_0] \cup [t_0, b]$. Compute repelling LCSs from a forward run over $[t_0, b]$, and attracting LCSs from the backward run over $[a, t_0]$ (see, e.g., Lekien and Ross [39], Lipinski and Mohseni [67]). Both repelling and attracting LCSs are then obtained at the same time slice t_0. However, they correspond to two different finite-time dynamical systems: one defined over $[a, t_0]$ and the other over $[t_0, b]$. This approach works well for a roughly T-periodic system, when $t_0 - a$ and $b - t_0$ are integer multiples of T. In general, however, hyperbolic LCSs computed over $[a, t_0]$ and over $[t_0, b]$ do not evolve into each other as t_0 is varied, and hence the resulting structures are not dynamically consistent. In addition, one cannot identify attracting LCSs at time a or repelling LCSs at time b from this approach.

2. Approach II: Extract repelling LCSs at the initial time a from a forward run over $[a, b]$; extract attracting LCSs at the final time b from a backward run over $[a, b]$. Obtain repelling LCSs at any time $t_0 \in [a, b]$ by advecting repelling LCSs from a to t_0 under the flow. Similarly, obtain attracting LCSs at any time $t_0 \in [a, b]$ by advecting attracting LCSs from b to t_0 under the flow. This approach identifies LCSs based on the full available data, and provides dynamically consistent surfaces that evolve into each other as t_0 varies [44, 48]. Since the forward-time advection of a repelling LCS (as well as the backward-time advection of an attracting LCS) is numerically unstable (see figure 2.2), this approach requires extra care to suppress growing instabilities [48]. Even under well-controlled instabilities, however, a further issue arises in near-incompressible flows: repelling LCSs shrink exponentially under forward-advection, and attracting LCSs shrink exponentially under backward-advection. Therefore, while the LCSs obtained in this fashion are dynamically consistent, they require substantial numerical effort to extract and may still reveal little about the dynamics.

Here we develop a new approach that keeps the dynamical consistency of Approach II but eliminates the instability and shrinkage of advected LCSs. Our key observation is that attracting LCSs can also be recovered as codimension-one hypersurfaces normal to the weakest eigenvector field of the forward Cauchy-Green strain tensor. These *stretch-surfaces* are obtained from the same forward-time calculation that reveals repelling LCSs as *strain-surfaces,* i.e., codimension-one surfaces normal to the dominant eigenvector of the forward Cauchy-Green strain tensor [48]. The locally most compressing strain-surfaces and the locally most expanding stretch-surfaces then reveal repelling and attracting LCSs at the same initial time a based on a single forward-time calculation over $[a, b]$.

We demonstrate the results on three examples: an autonomous Duffing oscillator (§2.5.1), a direct numerical simulation of two-dimensional turbulence (§2.5.2) and the three-dimensional classic ABC flow (§2.5.3).

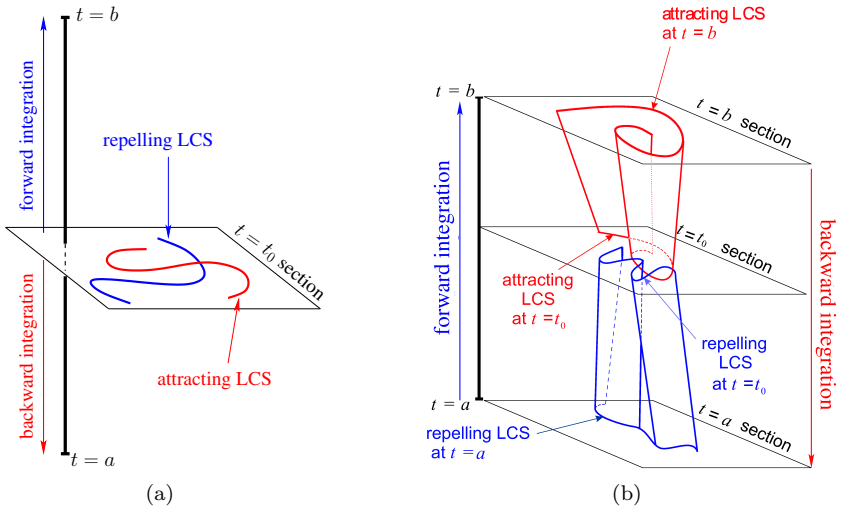

Figure 2.1: Schematic illustration of Approach I (a) and Approach II (b) in the extended phase space.

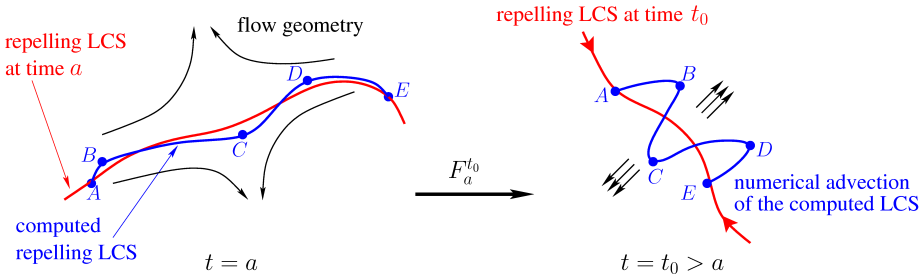

Figure 2.2: The errors in the computation of a repelling LCS grow exponentially as the LCS is advected forwards in time. The same statement holds for the backward-time advection of an attracting LCS.

2.2 Preliminaries and notation

Consider the dynamical system

$$\dot{x} = u(x,t), \quad x \in U \subset \mathbb{R}^n, \quad t \in I = [a,b], \tag{2.1}$$

where $u : U \times I \to \mathbb{R}^n$ is a sufficiently smooth velocity field. For $t_0, t \in I$, define the flow map

$$\begin{aligned} F_{t_0}^{t} &: U \to U \\ &x_0 \mapsto x(t; t_0, x_0), \end{aligned} \tag{2.2}$$

as the unique one-to-one map that takes the initial condition x_0 to its time-t position $x(t; t_0, x_0)$ under system (6.1).

The *forward Cauchy–Green strain tensor* over the time interval I is defined in terms of the flow gradient ∇F_a^b as

$$C^f = \left(\nabla F_a^b\right)^\top \nabla F_a^b. \tag{2.3}$$

At each initial condition $x_0 \in U$, the tensor $C^f(x_0)$ is represented by a symmetric, positive definite, $n \times n$ matrix with an orthonormal set of eigenvectors $\{\xi_k^f(x_0)\}_{1 \le k \le n}$, and with a corresponding set of eigenvalues $\{\lambda_k^f(x_0)\}_{1 \le k \le n}$ satisfying

$$C^f(x_0)\xi_k^f(x_0) = \lambda_k^f(x_0)\xi_k^f(x_0), \quad k \in \{1, 2, \cdots, n\}, \tag{2.4a}$$

$$0 < \lambda_1^f(x_0) \le \lambda_2^f(x_0) \le \cdots \le \lambda_n^f(x_0). \tag{2.4b}$$

These invariants of the Cauchy–Green strain tensor characterize the deformation experienced by trajectories starting close to x_0. If a unit sphere is placed at x_0, its image under the linearized flow map ∇F_a^b will be an ellipsoid whose principal axes align with the eigenvectors $\{\xi_k^f(x_0)\}_{1 \le k \le n}$ and have corresponding lengths $\{\lambda_k^f(x_0)\}_{1 \le k \le n}$.

Similarly, the *backward Cauchy–Green strain tensor* over the time interval I is defined as

$$C^b = \left(\nabla F_b^a\right)^\top \nabla F_b^a. \tag{2.5}$$

Its eigenvalues $\{\lambda_k^b(x_0)\}_{1 \le k \le n}$ and orthonormal eigenvectors $\{\xi_k^b(x_0)\}_{1 \le k \le n}$ satisfy similar properties as those in equation (2.4). Their geometric meaning is similar to that of the invariants of C^f, but in backward time.

2.3 Repelling and attracting LCSs

A repelling LCS over the time interval I is a codimension-one material surface that is pointwise more repelling over I than any nearby material surface. If $\mathcal{R}(t)$ represents the time-t position of such an LCS, then the initial LCS position $\mathcal{R}(a)$ must be everywhere orthogonal to the most-stretching eigenvector ξ_n^f of the forward Cauchy–Green strain tensor C^f [44, 23]. Specifically, we must have

$$T_{x_a}\mathcal{R}(a) \perp \xi_n^f(x_a), \tag{2.6}$$

for any point $x_a \in \mathcal{R}(a)$, where $T_{x_a}\mathcal{R}(a)$ denotes the tangent space of $\mathcal{R}(a)$ at point x_a.

Similarly, an attracting LCS over the time interval I is a codimension-one material surface that is pointwise more attracting over I than any nearby material surface. If $\mathcal{A}(t)$ is the time-t position of an *attracting* LCS, its final position $\mathcal{A}(b)$ satisfies

$$T_{x_b}\mathcal{A}(b) \perp \xi_n^b(x_b), \tag{2.7}$$

for all points $x_b \in \mathcal{A}(b)$. That is, the time-b position of attracting LCS is everywhere orthogonal to the eigenvector ξ_n^b of the backward Cauchy–Green strain tensor C^b.

The relation (2.6) enables the construction of repelling LCS candidates at time $t = a$, while (2.7) enables the construction of attracting LCS candidates at the final time $t = b$ (see, e.g., Farazmand and Haller [48], Hadjighasem et al. [53]). Since LCSs are constructed as material surfaces, they move with the flow. Therefore, LCS positions at an intermediate time $t_0 \in [a, b]$ are, in principle, uniquely determined by their end-positions:

$$\mathcal{R}(t_0) = F_a^{t_0}(\mathcal{R}(a)), \qquad \mathcal{A}(t_0) = F_b^{t_0}(\mathcal{A}(b)). \tag{2.8}$$

As discussed in the introduction, however, using the advection formulae (2.8) leads to numerical instabilities. This is because the material surfaces involved are unstable in the time direction they are advected in. This instability can only be controlled by employing a high-end numerical integrator which refines the advected surface when large stretching develops. Even under high-precision advection, however, the end-result is an exponentially shrinking surface which only captures subsets of the most influential material surfaces.

2.4 Main result

Here we present a direct method to identify both attracting and repelling LCSs at the same time instance, using the same finite time-interval. These surfaces, therefore, are based on the assessment of the same finite-time dynamical system, avoiding the dynamical inconsistency we reviewed for Approach I in the Introduction.

In particular, we show that the initial position of an attracting LCS, $\mathcal{A}(a)$, is everywhere orthogonal to the weakest eigenvector ξ_1^f of the tensor C^f. This, together with the orthogonality of the initial repelling LCS position $\mathcal{R}(a)$ to the dominant eigenvector ξ_n^f of C^f, allows for the simultaneous construction of attracting and repelling LCSs at time $t = a$, utilizing the same time interval $[a, b]$. All this renders the computation of the backward Cauchy–Green strain tensor C^b unnecessary.

Definition 2.1 (Strain-surface)**.** Let $\mathcal{M}(t)$ be an $(n-1)$-dimensional smooth material surface in U, evolving under the flow map over the time interval $I = [a, b]$ as $\mathcal{M}(t) = F_a^t(\mathcal{M}(a))$. Denote the tangent space of $\mathcal{M}$ at a point $x \in \mathcal{M}$ by $T_x\mathcal{M}$.

(i) $\mathcal{M}(t)$ is called a *forward strain-surface* if $\mathcal{M}(a)$ is everywhere normal to the eigenvector field ξ_n^f, i.e.,

$$T_{x_a}\mathcal{M}(a) \perp \xi_n^f(x_a), \quad \forall x_a \in \mathcal{M}(a).$$

(ii) $\mathcal{M}(t)$ is called a *backward strain-surface* if $\mathcal{M}(b)$ is everywhere normal to the eigenvector field ξ_n^b, i.e.,

$$T_{x_b}\mathcal{M}(b) \perp \xi_n^b(x_b), \quad \forall x_b \in \mathcal{M}(b).$$

Strain-surfaces are generalizations of the strainlines introduced in Farazmand and Haller [48] and Haller and Beron-Vera [23] in the theory of hyperbolic LCSs for two-dimensional flows. By contrast, the stretch-surfaces appearing in the following definition have not yet been used even in two-dimensional LCS detection.

Definition 2.2 (Stretch-surface)**.** Let $\mathcal{M}(t)$ be an $(n-1)$-dimensional material surface as in definition 2.1.

(i) $\mathcal{M}(t)$ is called a *forward stretch-surface* if $\mathcal{M}(a)$ is everywhere normal to the eigenvector field ξ_1^f, i.e.,

$$T_{x_a}\mathcal{M}(a) \perp \xi_1^f(x_a), \quad \forall x_a \in \mathcal{M}(a).$$

(ii) $\mathcal{M}(t)$ is called a *backward stretch-surface* if $\mathcal{M}(b)$ is everywhere normal to the eigenvector field ξ_1^b, i.e.,

$$T_{x_b}\mathcal{M}(b) \perp \xi_1^b(x_b), \quad \forall x_b \in \mathcal{M}(b).$$

By definition, the local orientation of a forward strain-surface is known at the initial time $t = a$. The following theorem determines the local orientation of the same strain-surface at the final time $t = b$, rendering the forward-advection of the surface unnecessary. The same theorem provides the local orientation of backward strain-surfaces at the initial time $t = a$ (see figure 2.3 for an illustration).

Theorem 2.1.

(i) *Forward strain-surfaces coincide with backward stretch-surfaces.*

(ii) *Backward strain-surfaces coincide with forward stretch-surfaces*

Proof. See Appendix 2.A. □

The following corollary summarizes the implications of Theorem 2.1, along with known results from Haller [44] and Farazmand and Haller [48].

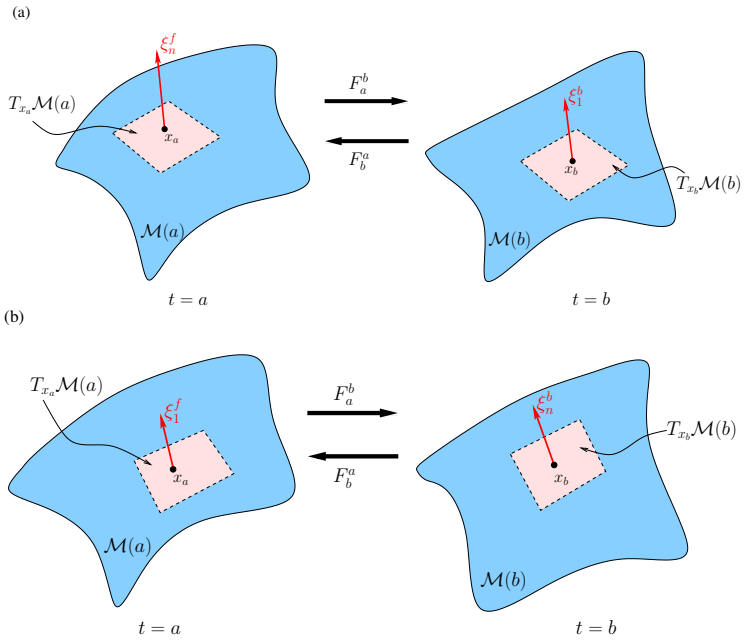

Figure 2.3: (a) A forward strain-surface evolves into a backward stretch-surface. (b) A forward stretch-surface evolves into a backward strain-surface.

Corollary 2.1. Let $\mathcal{R}(t)$ and $\mathcal{A}(t)$ be, respectively, repelling and attracting LCSs of the dynamical system (6.1). Then the following hold:

(i) A repelling LCS, $\mathcal{R}(t)$, is a forward strain-surface, i.e., $\mathcal{R}(a)$ is everywhere orthogonal to the eigenvector field ξ_n^f. Furthermore, $\mathcal{R}(t)$ is also a backward stretch-surface, i.e., $\mathcal{R}(b)$ is everywhere orthogonal to the eigenvector field ξ_1^b.

(ii) An attracting LCS, $\mathcal{A}(t)$, is a forward stretch-surface, i.e., $\mathcal{A}(a)$ is everywhere orthogonal to the eigenvector field ξ_1^f. Furthermore, $\mathcal{A}(t)$ is also a backward strain-surface, i.e., $\mathcal{A}(b)$ is everywhere orthogonal to the eigenvector field ξ_n^b.

Among other things, the above corollary enables the visualization of attracting and repelling LCSs simultaneously at the initial time $t = a$ of a finite time-interval $[a, b]$ over which the underlying dynamical system is known (see section §2.5 below for examples). This only requires the computation of the forward-time Cauchy–Green strain tensor C^f, rendering backward-time computations unnecessary.

2.5 Examples

Here we demonstrate the application of corollary 2.1 on three examples: the classic Duffing oscillator, a two-dimensional turbulence simulation, and the classic ABC flow. In the two-dimensional case (i.e., $n = 2$), we refer to strain- and stretch-surfaces as *strainlines* and *stretchlines*, respectively.

2.5.1 Duffing oscillator

Here we show that even for a two-dimensional autonomous system, stretchlines and strainlines act as *de facto* stable and unstable manifolds over finite time intervals. Indeed, over such intervals, sets of initial conditions will be seen to follow stretchlines in forward time. Only asymptotically do these initial conditions align with the well-known classic unstable manifolds.

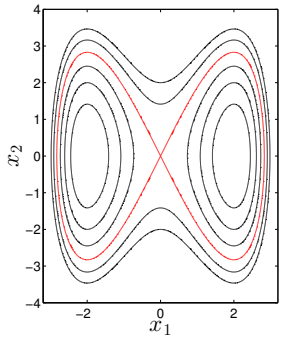

Figure 2.4: Trajectories of system (2.9). The homoclinic orbits are shown in red.

Consider the unforced and undamped Duffing oscillator

$$\begin{aligned} \dot{x}_1 &= x_2, \\ \dot{x}_2 &= 4x_1 - x_1^3, \end{aligned} \tag{2.9}$$

whose Hamiltonian $H(x_1, x_2) = \frac{1}{2}x_1^4 - 4x_1^2 + x_2^2$ is conserved along the trajectories (see figure 2.4). The hyperbolic fixed point $(0, 0)$ of the system admits two homoclinic orbits (shown in red), which coincide with the stable and unstable manifolds of the fixed point.

By Definition 2.1, forward strainlines over a finite time interval are everywhere orthogonal to the eigenvector field ξ_2^f of the forward strain tensor C^f. As a result, strainlines are trajectories of the autonomous ordinary differential equation (ODE)

$$r'(s) = \xi_1^f(r(s)), \quad r(0) = r_0, \tag{2.10}$$

where $r : s \mapsto r(s)$ denotes parametrization by arc-length. Similarly, forward stretchlines are trajectories of the ODE

$$p'(s) = \xi_2^f(p(s)), \quad p(0) = p_0, \tag{2.11}$$

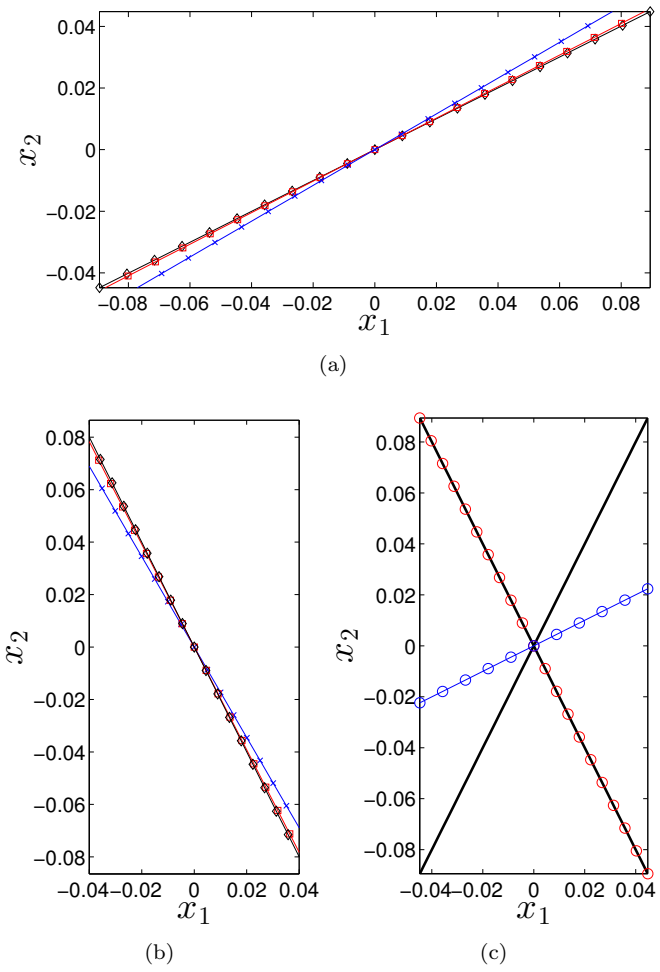

Figure 2.5: (a) Forward stretchline through the origin for three integration times $T = 0.5$ ($- \times -$), $T = 1$ ($-\square-$) and $T = 2$ ($- \diamond -$). (b) Forward strainline for the same integration times, as in panel (a). (c) The asymptotic position of the strainline ($- \circ -$) and the stretchline ($- \circ -$) compared to the classic stable and unstable manifolds (black).

with $p : s \mapsto p(s)$ denoting an arclength-parametrization. Since we are interested in the *de facto* finite-time stable and unstable manifolds passing through the hyperbolic fixed point $(0, 0)$, we set $r_0 = p_0 = (0, 0)$.

We observe that as the integration time T increases, the unique strainline and the unique stretchline through the origin converge to their asymptotic limits. Figure 2.5 shows the convergence of these curves around the hyperbolic fixed point $(0, 0)$. For integration times $T \geq 2$, the computed strainlines and

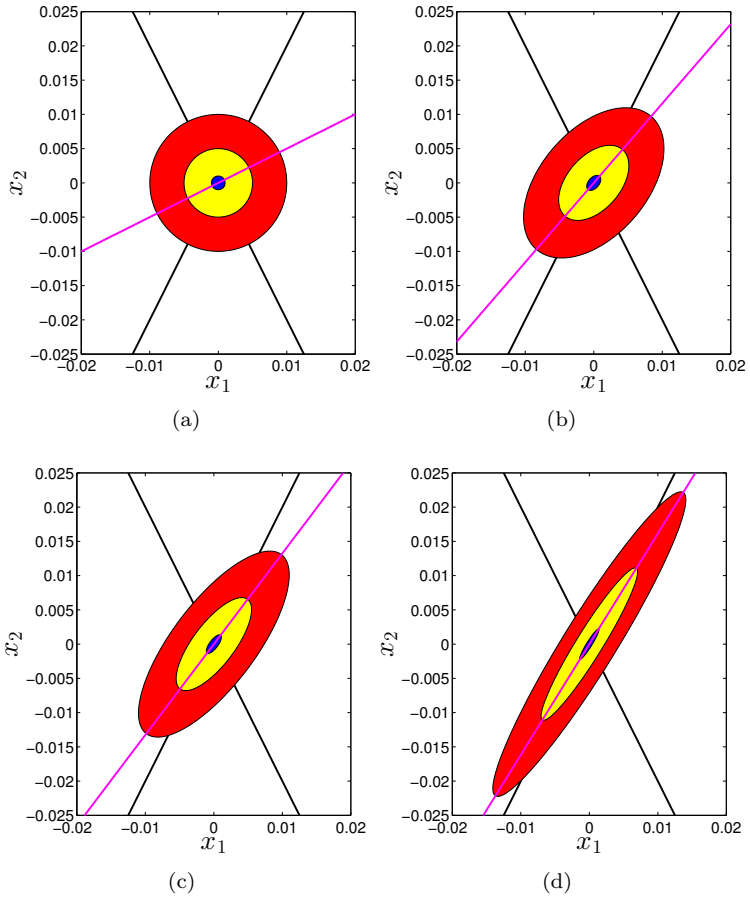

Figure 2.6: (a) Classical stable and unstable manifolds (black) are shown together with the stretchline through the origin (magenta). Three blobs of tracers with radii 10^{-3} (blue), 5×10^{-3} (yellow) and 10^{-2} (red) are centered at the origin. The tracers and the manifolds are then advected to time $t = 0.1$ (b) $t = 0.2$ (c) and $t = 0.4$ (d). Over the time interval $[0, 2]$, the stretchline is the de facto unstable manifold for spreading tracers. For larger advection times, this de facto unstable manifold practically coincides the classic unstable manifold of the origin

stretchlines are virtually indistinguishable from their asymptotic limits. Therefore, in the following, we fix the integration time $T = b - a = 2$ with $a = 0$ and $b = 2$.

Note that while the strainline is indistinguishable from the stable manifold, the stretchline differs from the unstable manifold (see figure 2.5c). Stretchlines as *de facto* finite-time unstable manifolds define the directions along which pas-

sive tracers are observed to stretch. To demonstrate this, in figure 2.6, three disks with radii 10^{-3}, 5×10^{-3} and 10^{-2} are initially centered at the origin. For short advection times, the tracers elongate in the direction of the stretchline, not the unstable manifold. Unlike the classic unstable manifold, stretchlines evolve in time and only become invariant when viewed in the extended phase space of the (x,t) variables. For longer advection times (not presented here), the stretchline converges to the unstable manifold and becomes virtually indistinguishable from it.

2.5.2 Two-dimensional turbulence

We consider a two-dimensional velocity field $u : U \times \mathbb{R}^+ \to \mathbb{R}^2$, obtained as a numerical solution of the Navier–Stokes equations

$$\begin{aligned} \partial_t u + u\cdot\nabla u &= -\nabla p + \nu\Delta u + f,\\ \nabla\cdot u &= 0,\\ u(x,0) &= u_0(x). \end{aligned} \tag{2.12}$$

The domain $U = [0,2\pi]\times[0,2\pi]$ is periodic in both spatial directions. The non-dimensional viscosity ν is equal to 10^{-5}. The forcing f is random in phase and active over the wave numbers $3.5 < k < 4.5$. The initial condition u_0 is the instantaneous velocity field of a decaying turbulent flow. We solve equations (5.7) by a standard pseudo-spectral method with 512×512 modes. The time integration is carried out by a 4th order Runge–Kutta method with adaptive step-size (MATLAB's ODE45). Equation (5.7) is solved over the time interval $I = [0,50]$.

One can, in principle, compute an attracting LCS at the beginning of a time interval $I = [a,b]$ by advecting the attracting LCS extracted at $t = b$ back to $t = a$. As mentioned in the Introduction, however, this process is numerically unstable since attracting LCSs become unstable in backward time. Their instability is apparent in figure 2.7, where an attracting LCS (red) is advected backwards from $t = 50$ to the initial time $t = 0$. The advected curve is noisy and deviates from the true pre-image (blue curve). The true pre-image, the stretchline, is computed as a trajectory of the eigenvector filed ξ_2^f of the forward Cauchy–Green strain tensor C^f.

We now extract the set of attracting LCSs that shape observed global tracer patterns in this turbulent flow. Corollary 2.1 establishes that such LCSs are necessarily forward stretchlines, i..e, trajectories of (2.11). It then remains to select the trajectories of this ODE that stretch more under forward advection than any neighboring stretchline [23].

The relative stretching of a material line is defined as the ratio of its length at the final time $t = b$ to its initial length at time $t = a$. For a forward-time stretchline γ, one can show (see Appendix 2.B) that the relative stretching is given by

$$q(\gamma) = \frac{1}{\ell(\gamma)}\int_\gamma \sqrt{\lambda_2^f}\,\mathrm{d}s, \tag{2.13}$$

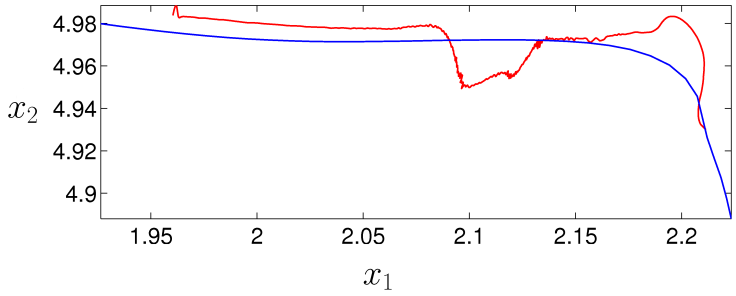

Figure 2.7: Stretchline (blue) and the advected image of an attracting LCS (red) at $t = 0$. The exponential growth of errors in backward-time advection of the LCS results in a jagged curve that deviates from the true attracting LCS.

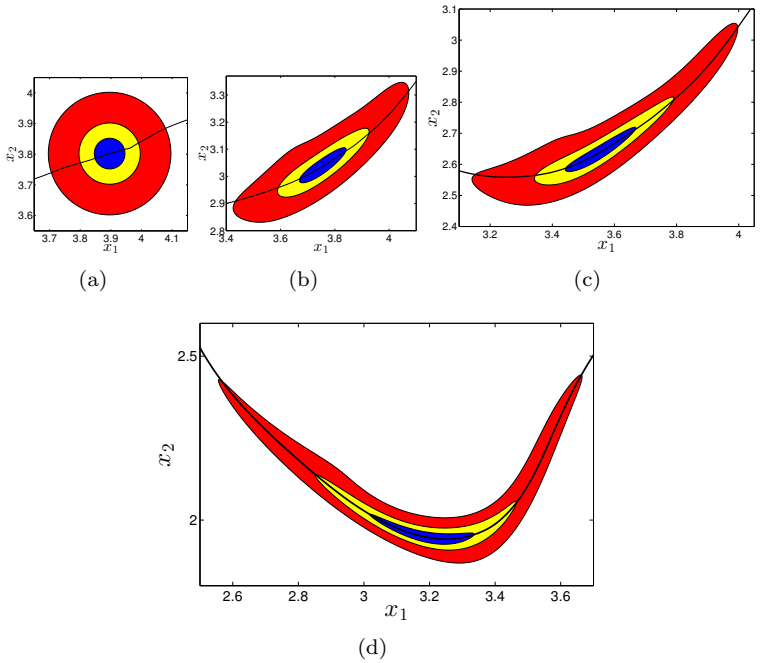

Figure 2.8: (a) The concentric tracers with radii 0.05 (blue), 0.1 (yellow) and 0.2 (red). The stretchline (black) passing through the center is computed from the time interval $[0, 50]$ (i.e., $a = 0$ and $b = 50$). The tracers and the stretchline are then advected forward in time to $t = 10$ (b), $t = 15$ (c), $t = 25$ (d).

where $\ell(\gamma)$ is the length of γ at time $t = a$. Note that no material line advection is required for computing the relative stretching in (2.13).

In order to locate the stretchlines that locally maximize the relative stretch-

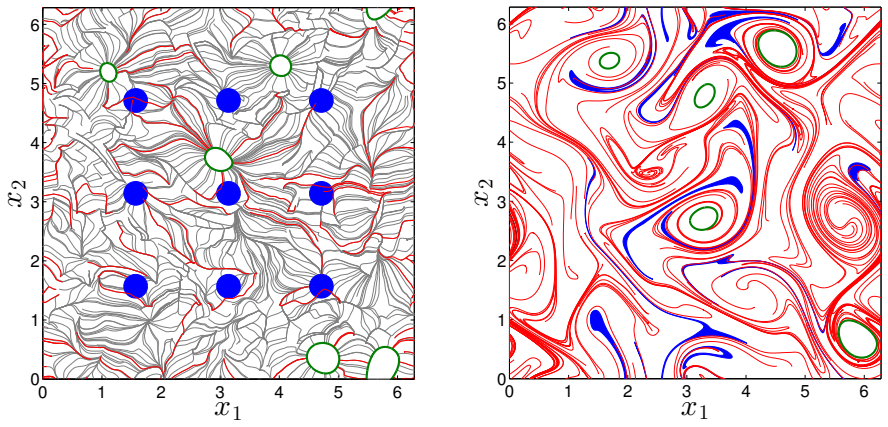

Figure 2.9: (a) Forward stretchlines at $t = 0$. The attracting LCSs (i.e., locally most-stretching stretchlines) are highlighted in red. The green closed curves show the boundaries of elliptic regions. Tracers (blue circles) are used to visualize the overall mixing patterns. (b) Advected image of the attracting LCSs, tracers and elliptic barriers at time $t = 50$.

ing (2.13), we adopt the numerical procedure outlined in Haller and Beron-Vera [23] for locating the locally least-stretching strainlines. Specifically, we first compute a dense enough set of stretchlines as the trajectories of ODE (2.11). We stop the integration once the stretchline reaches a singularity of the tensor field C^f or crosses an elliptic transport barrier.

A *singularity* of C^f is a point where C^f equals the identity tensor, and hence its eigenvectors are not uniquely defined (see Delmarcelle and Hesselink [60] and Tricoche et al. [77] for more details). An *elliptic barrier* is the outermost member of a nested set of closed curves that preserve their initial length (at time $t = a$) under advection up to time $t = b$ [23]. In an incompressible flow, an elliptic barrier also preserves its enclosed area under advection, and hence the elliptic domain it encloses remains highly coherent. For this reason, elliptic barriers can be considered as generalizations of outermost KAM curves generically observed in temporally periodic two-dimensional flows [23].

We locate elliptic barriers using the detection algorithm developed in Haller and Beron-Vera [23] and Hadjighasem et al. [53]. With the location of these barriers and of the singularities of C^f at hand, stretchlines are truncated to compact line segments, rendering the integral in (2.13) well-defined. Attracting LCSs at $t = a$ are then located as stretchline segments that have higher relative stretching (2.13) than any of their C^1-close neighbors. This process is briefly summarized in the following algorithm:

Algorithm 2.1.

1. Compute the Cauchy–Green strain tensor C^f over a uniform grid.
2. Locate elliptic barriers by the procedure described in [23] and [53].
3. Compute stretchlines as trajectories of (2.11). The initial conditions p_0 are chosen from a uniform grid over the phase space.
4. Stop the stretchline integration once the stretchlines reach either a singular point or an elliptic region bounded by an elliptic barrier.
5. For each stretchline so obtained, compute the relative stretching (2.13).
6. Locate attracting LCSs as the stretchlines with locally maximal relative stretching.

To illustrate the defining role of stretchlines in the formation of turbulent mixing patterns, we consider three concentric circles of tracers with radii 0.05, 0.1 and 0.2 at the initial time $t = a = 0$ (see figure 2.8). The circles are centered on a stretchline with locally largest relative stretching (black curve). Then the stretchlines and tracers are advected to times $t_0 = 10$, $t_0 = 15$ and $t_0 = 25$. In each case, we find that the tracer pattern stretches and alines with the evolving stretchline, as expected.

We now turn to the global geometry of the attracting LCSs. Figure 2.9a shows stretchlines computed from a uniform grid of 30×30 points. Attracting LCSs at time $t = 0$, extracted as stretchlines with the locally largest relative stretching, are highlighted in red. Also shown are the elliptic barriers (greed closed curves), as well as a select set of blue tracer disks that will be used to illustrate the role of attracting LCSs. The advected positions of attracting LCSs, elliptic barriers and tracer disks are shown in figure 2.9b. Note how the attracting LCSs govern the deformation of the tracer disks in the turbulent mixing region. Meanwhile, the elliptic barriers keep their coherence by preserving their arclength and enclosed area.

2.5.3 ABC flow

In two dimensions, stretchlines are constructed as trajectories of the eigenvector field ξ_2^f. The resulting curves are, by construction, everywhere orthogonal to the eigenvector field ξ_1^f. In higher dimensions, however, constructing stretch-surfaces that are everywhere orthogonal to the eigenvector ξ_1^f is nontrivial. In fact, for a given eigenvector field, such a surface may only exists locally if a Frobenius condition is satisfied [78]. This condition requires the eigenvectors spanning the tangent space of the manifold (here, $\{\xi_k^f\}_{2\leq k\leq n}$) to be in involution, i.e., their Poisson brackets $[\xi_i^f, \xi_j^f]$ should be in the tangent space of the manifold for any $i, j \in \{2, 3, \cdots, n\}$.

Even when the subset of the phase space satisfying this Frobenius condition is known, constructing stretch-surfaces globally as smooth parametrized manifolds normal to a specific vector field is challenging [73, 79]. Here we only

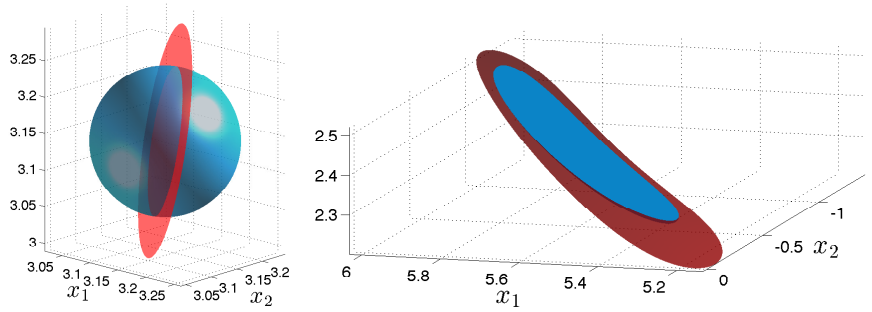

(a) (b)

Figure 2.10: (a) A spherical tracer surface (blue) at time $t = 0$ and the corresponding approximate stretch-surface (red) passing through its origin. (b) The advected positions of these surfaces at the final time $t = 4$.

illustrate that locally constructed stretch-surfaces do govern the formation of tracer patterns in three-dimensional flows as well.

We use the classic ABC flow [15]

$$\begin{aligned} \dot{x}_1 &= A\sin(x_3) + C\cos(x_2), \\ \dot{x}_2 &= B\sin(x_1) + A\cos(x_3), \\ \dot{x}_3 &= C\sin(x_2) + B\cos(x_1), \end{aligned} \tag{2.14}$$

with $A = 1$, $B = \sqrt{2/3}$ and $C = \sqrt{1/3}$. The C^f strain tensor is computed over the time interval $I = [0, 4]$ (i.e., $a = 0$ and $b = 4$). We release a spherical blob of initial conditions centered at (π, π) with radius 0.1. We approximate the stretch-surface passing through this point by the plane normal to the first eigenvector ξ_1^f of C^f. Figure 2.10a shows this plane together with the sphere of tracers at time $t = 0$. The advected images of the tracer and the plane at time $t = 4$ are shown in figure 2.10b, demonstrating that the stretch-surface through the center of the tracer blob acts as a *de facto* unstable manifold in this three-dimensional example as well.

2.6 Conclusions

We have shown that both repelling and attracting LCSs (finite-time stable and unstable manifolds) at a time instance $t = a$ can be extracted from a single forward-time computation over a time interval $I = [a, b]$. This extraction requires the computation of the eigenvectors of the forward Cauchy–Green strain tensor C^f. It has been found previously [44, 23] that at time $t = a$, the position of repelling LCSs are strain-surfaces, i.e., are everywhere orthogonal to the dominant eigenvector of C^f. Here we proved that the $t = a$ positions of attract-

ing LCSs are stretch-surfaces, i.e., are everywhere orthogonal to the weakest eigenvector of C^f.

The attracting LCSs obtained in this fashion are observed as centerpieces around which tracer patterns develop. Even in autonomous dynamical systems, these evolving centerpieces of trajectory evolution differ from classic unstable manifolds, forming *de facto* unstable manifolds over finite times.

In two-dimensional dynamical systems, stretchlines can be directly computed as most-stretching trajectories of the autonomous ODE (2.11). In higher dimensions, stretch-surfaces satisfy linear systems of partial differential equations (PDEs), as any surface normal to a given vector field does [73]. While a self-consistent global solution of these PDEs remains numerically challenging, here we have illustrated the local organizing role of stretch-surfaces through the advection of their tangent spaces in the classic ABC flow. Results on the construction of attracting LCSs from globally computed stretch-surfaces will be reported elsewhere.

Appendix 2.A Proof of Theorem 2.1[1]

In order to prove Theorem 2.1, we need two lemmas. The first lemma draws a connection between eigenvalues of the forward- and backward-time Cauchy–Green strain tensors. The second lemma establishes a relation between their eigenvectors.

Lemma 2.1. *The largest eigenvalue λ_n^f of the forward-time strain tensor C^f at a point $x_a \in U$ coincides with the reciprocal of the smallest eigenvalue λ_1^b of the backward-time strain tensor C^b at the point $x_b = F_a^b(x_a)$, i.e.,*

$$\lambda_n^f(x_a) = \frac{1}{\lambda_1^b(x_b)}. \tag{2.15}$$

Similarly, we have

$$\lambda_n^b(x_b) = \frac{1}{\lambda_1^f(x_a)}. \tag{2.16}$$

Proof. This follows directly from equation (13) in Haller and Sapsis [81]. □

Lemma 2.2. *For any $x_a \in U$, the following identities hold for any $k \in \{1, 2, \cdots, n\}$.*

$$\langle \xi_n^f(x_a), \nabla F_b^a(x_b)\xi_k^b(x_b)\rangle = \lambda_n^f(x_a)\lambda_k^b(x_b)\langle \xi_n^f(x_a), \nabla F_b^a(x_b)\xi_k^b(x_b)\rangle, \tag{2.17}$$

$$\langle \xi_n^b(x_b), \nabla F_a^b(x_a)\xi_k^f(x_a)\rangle = \lambda_n^b(x_b)\lambda_k^f(x_a)\langle \xi_n^b(x_b), \nabla F_a^b(x_a)\xi_k^f(x_a)\rangle, \tag{2.18}$$

where $\langle \cdot, \cdot \rangle$ is the Euclidean inner product between two vectors.

[1] Recently, a shorter proof was proposed by Karrasch [80]

Proof. We prove identity (2.17). The proof of (2.18) is similar and will be omitted.

First, note that since the flow map is invertible, we have $F_b^a\left(F_a^b(x_a)\right) = x_a$ for any $x_a \in U$. Differentiating this identity with respect to x_a, we obtain

$$\nabla F_b^a(x_b) = \left[\nabla F_a^b(x_a)\right]^{-1}. \tag{2.19}$$

The result then follows from the identity

$$\begin{aligned}
\langle \xi_n^f(x_a), \nabla F_b^a(x_b)\xi_k^b(x_b)\rangle &= \langle \xi_n^f(x_a), [\nabla F_b^a(x_b)]^{-\top}[\nabla F_b^a(x_b)]^{\top}\nabla F_b^a(x_b)\xi_k^b(x_b)\rangle \\
&= \langle [\nabla F_b^a(x_b)]^{-1}\xi_n^f(x_a), C^b(x_b)\xi_k^b(x_b)\rangle \\
&= \lambda_k^b(x_b)\langle \nabla F_a^b(x_a)\xi_n^f(x_a), \xi_k^b(x_b)\rangle \\
&= \lambda_k^b(x_b)\langle [\nabla F_a^b(x_a)]^{-\top}[\nabla F_a^b(x_a)]^{\top}\nabla F_a^b(x_a)\xi_n^f(x_a), \xi_k^b(x_b)\rangle \\
&= \lambda_k^b(x_b)\langle C^f(x_a)\xi_n^f(x_a), [\nabla F_a^b(x_a)]^{-1}\xi_k^b(x_b)\rangle \\
&= \lambda_n^f(x_a)\lambda_k^b(x_b)\langle \xi_n^f(x_a), \nabla F_b^a(x_b)\xi_k^b(x_b)\rangle,
\end{aligned}$$

where we have used identity (2.19) twice. □

Now we turn to the proof of Theorem 2.1.

Proof of Theorem 2.1:

(i) Assume that $\mathcal{M}(t)$ is a backward stretch-surface. Then, by definition, $\mathcal{M}(b)$ is everywhere orthogonal to the eigenvector field ξ_1^b. In order to show that $\mathcal{M}(t)$ is a forward strain-surface, it suffices to show that $\mathcal{M}(a) = F_b^a(\mathcal{M}(b))$ is everywhere normal to the eigenvector field ξ_n^f. Since $T_{x_b}\mathcal{M}(b) = \text{span}\{\xi_k^b(x_b)\}_{2\le k\le n}$ for any $x_b \in \mathcal{M}(b)$, we have

$$T_{x_a}\mathcal{M}(a) = \text{span}\{\nabla F_b^a(x_b)\xi_k^b(x_b)\}_{2\le k\le n},$$

for all $x_a := F_b^a(x_b) \in \mathcal{M}(a)$. Therefore, it suffices to show that $\xi_n^f(x_a) \perp \nabla F_b^a(x_b)\xi_k^b(x_b)$ for any $x_a \in \mathcal{M}(a)$ and $k \in \{2, 3, \cdots, n\}$.

From Lemma 2.2, we have

$$\langle \xi_n^f(x_a), \nabla F_b^a(x_b)\xi_k^b(x_b)\rangle = \lambda_n^f(x_a)\lambda_k^b(x_b)\langle \xi_n^f(x_a), \nabla F_b^a(x_b)\xi_k^b(x_b)\rangle, \tag{2.20}$$

for any $x_a \in \mathcal{M}(a)$ and $k \in \{2, 3, \cdots, n\}$.

Using identity (2.15), we obtain

$$\langle \xi_n^f(x_a), \nabla F_b^a(x_b)\xi_k^b(x_b)\rangle = \frac{\lambda_k^b(x_b)}{\lambda_1^b(x_b)}\langle \xi_n^f(x_a), \nabla F_b^a(x_b)\xi_k^b(x_b)\rangle. \tag{2.21}$$

Hence, if

$$\lambda_1^b(x_b) \neq \lambda_k^b(x_b), \quad k \in \{2, 3, \cdots, n\}, \tag{2.22}$$

then we have

$$\langle \xi_n^f(x_a), \nabla F_b^a(x_b)\xi_k^b(x_b)\rangle = 0, \tag{2.23}$$

for any $k \in \{2, 3, \cdots, n\}$. But since $\lambda_1^b \le \lambda_2^b \le \cdots \le \lambda_n^b$, conditions (2.22) hold if and only if $\lambda_1^b(x_b) \neq \lambda_2^b(x_b)$. This condition holds away from repeated eigenvalues of C^b.

In short, if $\xi_1^b(x_b) \perp T_{x_b}\mathcal{M}(b)$ for all $x_b \in \mathcal{M}(b)$ then $\xi_n^f(x_a) \perp T_{x_a}\mathcal{M}(a)$ for any $x_a \in \mathcal{M}(a)$ which implies that $\mathcal{M}(a)$ is a forward strain-surface. This concludes the sufficiency condition of Theorem 2.1-(i).

As for the necessity of the same condition, let $\mathcal{M}(t)$ be a forward strain-surface, i.e. $T_{x_a}\mathcal{M}(a) = \text{span}\{\xi_k^f(x_a)\}_{1\le k\le n-1}$ for any $x_a \in \mathcal{M}(a)$. Therefore, the tangent space of its advected image $\mathcal{M}(b)$ is given by

$$T_{x_b}\mathcal{M}(b) = \text{span}\{\nabla F_a^b(x_a)\xi_k^f(x_a)\}_{1\le k\le n-1}.$$

To show that $\mathcal{M}(t)$ is a backward stretch-surface, it suffices to show that $\xi_1^b(x_b) \perp \nabla F_a^b(x_a)\xi_k^f(x_a)$ for any $x_b \in \mathcal{M}(b)$ and $k \in \{1, 2, \cdots, n-1\}$. Similarly to equation (2.21), one can show that

$$\langle \xi_1^b(x_b), \nabla F_a^b(x_a)\xi_k^f(x_a)\rangle = \frac{\lambda_k^f(x_a)}{\lambda_n^f(x_a)}\langle \xi_1^b(x_b), \nabla F_a^b(x_a)\xi_k^f(x_a)\rangle, \tag{2.24}$$

which implies that $\langle \xi_1^b(x_b), \nabla F_a^b(x_a)\xi_k^f(x_a)\rangle = 0$ for $k \in \{1, 2, \cdots, n-1\}$ away from the degenerate points where $\lambda_n^f = \lambda_{n-1}^f$.

(ii) The proof is identical to that of part (i).

□

Appendix 2.B Relative stretching of stretchlines

Here, we derive formula (2.13) for the relative stretching of forward stretchlines. Let γ_t be a smooth material line. Denote its time-a and time-b positions by γ_a and γ_b, respectively. Then, the relative stretching of the material line γ_t over the time interval $I = [a, b]$ is defined as

$$q(\gamma_t) := \frac{\ell(\gamma_b)}{\ell(\gamma_a)}, \tag{2.25}$$

where ℓ denotes the length of a curve.

Let $r : s \mapsto r(s)$ be the parametrization of γ_a by arc-length, i.e., let $|r'(s)| = 1$ for all $s \in [0, \ell(\gamma_a)]$. Since $\gamma_b = F_a^b(\gamma_a)$, the mapping $F_a^b \circ r : s \mapsto F_a^b(r(s))$ is a parametrization of the curve γ_b. Therefore, its length $\ell(\gamma_b)$ is given by

$$\begin{aligned}\ell(\gamma_b) &= \int_0^{\ell(\gamma_a)} |\nabla F_a^b(r(s))r'(s)|\mathrm{d}s \\ &= \int_0^{\ell(\gamma_a)} \sqrt{\langle r'(s), C^f(r(s))r'(s)\rangle}\mathrm{d}s.\end{aligned} \tag{2.26}$$

Now, if the material line γ_t is a forward stretchline, we have $r'(s) = \xi_2^f(r(s))$ for all $s \in [0, \ell(\gamma_a)]$. Substituting this in equation (2.26), we obtain

$$\ell(\gamma_b) = \int_0^{\ell(\gamma_a)} \sqrt{\lambda_2^f(r(s))}\mathrm{d}s := \int_{\gamma_a} \sqrt{\lambda_2^f}\mathrm{d}s.$$

Therefore, by definition (2.25), the relative stretching of a forward-time stretchline γ_t is given by

$$q(\gamma_t) = \frac{1}{\ell(\gamma_a)} \int_{\gamma_a} \sqrt{\lambda_2^f}\mathrm{d}s.$$

Chapter 3

Shearless transport barriers in unsteady two-dimensional flows and maps

3.1 Introduction

Consider a two-dimensional dynamical system with a family of invariant closed curves that are formed by periodic or quasi-periodic trajectories. The trajectories trace the invariant curves at specific frequencies. A shearless transport barrier then is generally defined as the invariant curve whose frequency admits a local extremum within the family. This definition ties shearless barriers fundamentally to recurrent (i.e., steady, periodic or quasiperiodic) flows where the necessary frequencies are well-defined. Here we extend the notion of a shearless transport barrier to two-dimensional flows and maps with general time-dependence.

In steady and time-periodic problems of fluid dynamics and plasma physics, shearless (or non-twist) barriers have been found to be particularly robust inhibitors of phase space transport [82–85]. For illustration, consider a steady, parallel shear flow

$$\begin{aligned} \dot{x} &= u(y), \qquad u'(y_0) = 0. \\ \dot{y} &= 0, \end{aligned} \tag{3.1}$$

on a domain periodic in x. The $y = y_0$ line marks a jet core, whose impact on tracer patterns is shown in Fig. 3.1 in a particular example with $y_0 = 0$. Note the unique material signature of the shearless barrier, deforming the tracer blob initialized along it into a boomerang-shaped pattern, By contrast, another tracer blob simply stretches under shear.

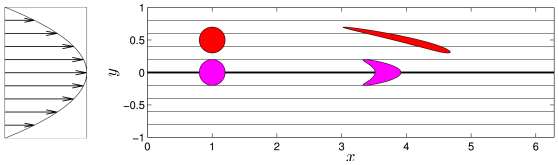

Figure 3.1: Left: The velocity profile of the steady flow (3.1) for $u(y) = 1 - y^2$. Right: Streamlines for the same flow. The thick line at $y = 0$ marks the shearless streamline that acts as a jet core. The tracer disk located on the shearless line (magenta circle) deforms into a blunt arrow shape symmetrically under advection to time $t = 9$. The tracer disk located away from the shearless line (red circle) has a markedly different deformation pattern. The boundary condition in the x-direction is taken to be periodic with period 2π.

The flow (3.1) is an idealized model of the velocity field inside atmospheric or oceanic zonal jets, or helical magnetic field lines in a tokamak [86]. As a dynamical system, (3.1) represents an integrable system with the Hamiltonian $H(y) = \int_0^y u(\eta)d\eta$. Its horizontal trajectories along which the Eulerian shear $u'(y)$ vanishes are referred to as shearless barriers. Along these barriers, $H''(y_0) = 0$ holds, thus the circle $y = y_0$ does not satisfy the twist condition of classic KAM theory [87].

Yet numerical studies of [82–84, 88] show that such barriers are more robust under steady or time-periodic perturbations than any other nearby KAM tori. Related theoretical results for two-dimensional maps were given in [89]. More recently, degenerate tori for steady 3D maps were considered in [90]. In addition, a general *a posteriori* result on non-twist tori of arbitrary dimension that are potentially far from integrable has been obtained by [91]. However, no general theory of shearless transport barriers for unsteady flows has been established.

The need for such a general theory of unsteady shearless barriers clearly exists. In plasma physics, computational and experimental studies suggest that shearless barriers enhance the confinement of plasma in magnetic fusion devices [92–95], which generate turbulent velocity fields with general time dependence. In this context, a description of shearless barriers is either understood in models for steady magnetic fields [95] or inferred from scalar quantities (e.g. temperature, density) in more complex unsteady scenarios [92–94].

In fluid dynamics, shearless barriers are of interest in the context of zonal jets. Rossby waves are the best known and most robust transport barriers in geophysical flows [96–99], yet only recent work attempts to describe their attendant unsteady jet cores in the Lagrangian frame of an unsteady flow. The method put forward in [100] seeks such Lagrangian shearless barriers as trenches of the finite-time Lyapunov exponent (FTLE) field. However, just as the examples in [44] show that FTLE ridges do not necessarily correspond to hyperbolic Lagrangian structures, FTLE trenches may also fail to mark zonal jet cores (see Example 3.1 in Section 3.7.2 below).

Here we develop a variational principle for shearless barriers as centerpieces of material strips showing no leading order variation in Lagrangian shear. This variational principle shows that shearless barriers are composed of tensorlines of the right Cauchy–Green strain tensor associated with the flow map. Most stretching or contracting Cauchy–Green tensorlines have previously been identified as best candidates for hyperbolic Lagrangian Coherent Structures (LCSs) [23, 49], but no underlying global variational principle has been known to which they would be solutions. The present work, therefore, also advances the theory of hyperbolic LCS, establishing them as shearless transport barriers under fixed (Dirichlet-type) boundary conditions.

Our main result is that parabolic transport barriers (jet cores) are also solutions of the same shearless Lagrangian variational principle, satisfying variable-endpoint boundary conditions. They are formed by minimally hyperbolic, structurally stable chains of tensorlines that connect singularities of the Cauchy–Green strain tensor field. We develop and test a numerical procedure that detects such tensorline chains, thereby finding generalized Lagrangian jet cores in an arbitrary, two-dimensional unsteady flow field in an automated fashion.

3.2 Notation and definitions

Let $u(x,t)$ denote a two-dimensional velocity field, with x labeling positions in a two-dimensional region U, and with t referring to time. Fluid trajectories generated by this velocity field satisfy the differential equation

$$\dot{x} = u(x,t), \tag{3.2}$$

whose solutions are denoted by $x(t;t_0,x_0)$, with x_0 referring to the initial position at time t_0. The evolution of fluid elements is described by the flow map

$$F_{t_0}^{t}(x_0) := x(t;t_0,x_0), \tag{3.3}$$

which takes any initial position x_0 to its current position at time t.

Lagrangian strain in the flow is often characterized by the right Cauchy–Green strain tensor field $C(x_0) = \left[\nabla F_{t_0}^{t}(x_0)\right]^{\top} \nabla F_{t_0}^{t}(x_0)$, whose eigenvalues $\lambda_i(x_0)$ and eigenvectors $\xi_i(x_0)$ satisfy

$$C\xi_i = \lambda_i \xi_i, \quad |\xi_i| = 1, \quad i = 1,2; \qquad 0 < \lambda_1 \leq \lambda_2, \qquad \xi_1 \perp \xi_2.$$

The tensor C, as well as its eigenvalues and eigenvectors, depend on the choice of the times t and t_0, but we suppress this dependence for notational simplicity.

3.3 Stability of material lines

Consider a material line (i.e., a smooth curve of initial conditions) γ at time t_0, parametrized as $r(s)$ with $s \in [0,\sigma]$. If $n(s)$ denotes a smoothly varying

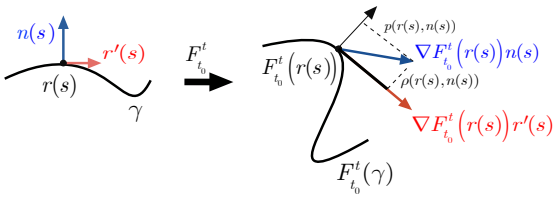

Figure 3.2: The evolution of a unit normal vector $n(s)$ of a material line γ under the linearized flow map $\nabla F^t_{t_0}$.

unit normal vector field along γ, then the *normal repulsion* ρ of γ over the time interval $[t_0, t]$ is given by [44]

$$\rho(r,n) = \frac{1}{\sqrt{\langle n, C^{-1}(r)n\rangle}}, \tag{3.4}$$

measuring at time t the normal component of the linearly advected normal vector $\nabla F^t_{t_0}(r)n$ (see Fig. 3.2). If $\rho > 1$ pointwise along γ, then the evolving material line $F^t_{t_0}(\gamma)$ is repelling. Similarly, if $\rho < 1$ holds pointwise along γ, then the evolving material line $F^t_{t_0}(\gamma)$ is attracting.

Hyperbolic Lagrangian coherent structures (LCSs) are pointwise most repelling or most attracting material lines with respect to small perturbations to their tangent spaces [44, 45, 49]. Repelling and attracting LCSs, respectively, are obtained as special trajectories of the differential equations

$$\dot r = \xi_1(r), \qquad \dot r = \xi_2(r), \tag{3.5}$$

that stay bounded away from points where ξ_i cease to be well-defined. These degenerate points x_0 are singularities of the Cauchy–Green tensor field, satisfying $C(x_0) = \lambda I$ for some $\lambda > 0$. (For an incompressible flow we have $\lambda = 1$.) The trajectories of the differential equations in (3.5) are called strainlines and stretchlines, respectively [48, 49]. From the definition of ρ in (3.4), we obtain that strainlines repel at a local rate of $\rho(r,n) = \sqrt{\lambda_2(r)}$, and stretchlines attract at a rate of $\rho(r,n) = \sqrt{\lambda_1(r)}$. Following the terminology used in the scientific visualization community [101, 102], we will refer to strainlines and stretchlines collectively as *tensorlines*.

A pointwise measure of how close a material curve is to being neutrally stable is the *neutrality* $\mathcal{N}(r,n)$, defined as

$$\mathcal{N}(r,n) = \big(\rho(r,n) - 1\big)^2. \tag{3.6}$$

Given the explicit normals known for tensorlines, their neutrality can be computed as a sole function of the location r, and can be written as

$$\mathcal{N}_{\xi_1}(r) = \Big(\sqrt{\lambda_2(r)} - 1\Big)^2, \qquad \mathcal{N}_{\xi_2}(r) = \Big(\sqrt{\lambda_1(r)} - 1\Big)^2,$$

respectively, for strainlines and stretchlines.

Here, we will be seeking generalized non-twist curves (or jet-cores) that are as close to neutral ($\mathcal{N} \equiv 0$) as possible. Requiring strictly zero neutrality along a material curve γ would, however, lead to an overdetermined problem. Indeed, a material line with neutral stability at all its points would be non-generic in an unsteady flow. Instead, we will be interested in material lines that are close to minimizing the neutrality, while also satisfying a minimal-shearing principle to be discussed later (see section §3.5).

Here we only work out a close-to-neutral condition for tensorlines, as they will turn out to have special significance in our search for shearless barriers. First, we define the convexity sets $\mathcal{C}_{\xi_i}$ of strainlines and stretchlines, respectively, as

$$\mathcal{C}_{\xi_i} = \left\{ x_0 \in U : \left\langle \partial_r^2 \mathcal{N}_{\xi_i}(x_0)\xi_j(x_0), \xi_j(x_0) \right\rangle > 0, \qquad i \neq j \right\}, \qquad i = 1, 2.$$

These sets are simply composed of points where the corresponding neutrality is a convex function. We say that a compact tensorline segment γ *is a weak minimizer* of its corresponding neutrality $\mathcal{N}_{\xi_i}(r)$ if both γ and the nearest trench of $\mathcal{N}_{\xi_i}(r)$ lie in the same connected component of $\mathcal{C}_{\xi_i}$. More specifically, a weak minimizer γ of $\mathcal{N}_{\xi_i}$, with parametrization $r_0(s)$ and smooth unit normal vector field $n_0(s)$, satisfies the condition

$$r_0(s) + \epsilon n_0(s) \in \mathcal{C}_{\xi_i}, \qquad s \in [0, \sigma], \quad \epsilon \in [0, \epsilon_0(s)], \tag{3.7}$$

where

$$\epsilon_0(s) = \min \left\{ |\epsilon| \in (0, \infty) : \partial_\epsilon \mathcal{N}_{\xi_i}\left(r_0(s) + \epsilon n_0(s)\right) = 0, \quad \partial_\epsilon^2 \mathcal{N}_{\xi_i}\left(r_0(s) + \epsilon n_0(s)\right) > 0 \right\}.$$

3.4 Eulerian and Lagrangian shear

For the two-dimensional steady flow shown in Fig. 3.1, the classic Eulerian shear in the x direction is defined as the derivative of the horizontal velocity field in the vertical direction, i.e.,

$$\frac{\partial u}{\partial y} = -2y, \tag{3.8}$$

which vanishes on the line $y_0 = 0$. This line plays the role of a jet core with a distinguished impact on tracer blobs in comparison to other horizontal streamlines (see Figure 3.1).

The Eulerian shear, as the normal derivative of a velocity component of interest, can certainly be computed for unsteady flows as well, and is indeed broadly used in fluid mechanics [103]. However, instantaneously shearless curves no longer act as invariant manifolds in the flow, and thus will generally not create the characteristic tracer patterns seen in Fig. 3.1. As a result, the mathematical description and systematic extraction of jet-core type material barriers in unsteady flows has been an open problem, despite their ubiquitous presence in plasma and geophysics.

To set the stage for a general description of jet-core-type structures, we first need a Lagrangian definition of shear that captures the type of material evolution seen in Fig. 3.1 even in an unsteady flow. For an arbitrary material curve $\gamma(t)$, we select a parametrization $r(s)$ with $s \in [0, \sigma]$ for γ at time t_0, and with the tangent vectors denoted as $r'(s)$.

We denote by $p(s)$ the pointwise tangential shear experienced over the time interval $[t_0, t]$ along the trajectory starting at time t_0 from the point $r(s)$. Following [23], we define $p(s)$ by first picking $n(s) = [r'(s)]^\perp / \left|[r'(s)]^\perp\right|$ as a unit vector normal to the curve γ at the point $r(s)$. The tangential shear $p(s)$ is then defined as the projection of the linearly advected normal $\nabla F_{t_0}^t(r(s))n(s)$ on the tangent space of the advected curve $F_{t_0}^t(\gamma)$ at the point $F_{t_0}^t(r(s))$ (see Fig. 3.2). Specifically, the *Lagrangian shear* $p(s)$ is given by

$$\begin{aligned} p(s) &= \left\langle \frac{\nabla F_{t_0}^t(r(s))r'(s)}{\left|\nabla F_{t_0}^t(r(s))r'(s)\right|}, \nabla F_{t_0}^t(r(s)) \frac{[r'(s)]^\perp}{\left|[r'(s)]^\perp\right|} \right\rangle \\ &= \frac{\langle r'(s), D(r(s))r'(s)\rangle}{\sqrt{\langle r'(s), C(r(s))r'(s)\rangle \langle r'(s), r'(s)\rangle}}, \end{aligned} \tag{3.9}$$

where $\langle \cdot, \cdot \rangle$ denotes the Euclidean inner product, and the tensor field D is defined as

$$D(x_0) = \frac{1}{2}[C(x_0)\Omega - \Omega C(x_0)], \qquad \Omega = \begin{pmatrix} 0 & -1 \\ 1 & 0 \end{pmatrix}. \tag{3.10}$$

Note that the tensor D is the symmetric part of the tensor $C\Omega$.

3.5 Variational principle for shearless barriers

We seek generalized shearless curves as centerpieces of regions with no observable change in the averaged material shear. More precisely, assume that $\epsilon > 0$ is a minimal threshold above which we can physically observe differences in material shear over the time interval $[t_0, t]$. By smooth dependence on initial fluid positions, we will typically observe an $\mathcal{O}(\epsilon)$ change in shear within an $\mathcal{O}(\epsilon)$-thick strip around a randomly chosen material curve γ. Our interest, however, is in exceptional γ curves around which $\mathcal{O}(\epsilon)$-thick coherent strips show no observable change in their average shearing.

The averaged Lagrangian shear experienced along γ over the time interval $[t_0, t]$ can be written as

$$P(\gamma) = \frac{1}{\sigma} \int_0^\sigma p(s)\, \mathrm{d}s, \tag{3.11}$$

where $p(s)$ is given by (3.9).

As we argued above, if an observable non-shearing material strip exists around γ, then on ϵ-close material curves we must have $P(\gamma+\epsilon h) = P(\gamma)+\mathcal{O}(\epsilon^2)$, where $\epsilon h(s)$ denotes a small perturbation to $r(s)$. This is only possible if the first variation of P vanishes on γ:

$$\delta P(\gamma) = 0. \tag{3.12}$$

This condition leads to the following weak form of the Euler-Lagrange equation:

$$\delta P(\gamma) = \frac{1}{\sigma}\left[\langle \partial_{r'} p, h\rangle\right]_0^\sigma + \frac{1}{\sigma}\int_0^\sigma \left[\partial_r p - \frac{d}{ds}\partial_{r'} p\right] h(s)\, ds = 0. \tag{3.13}$$

3.6 Boundary conditions

We are interested in two types of boundary conditions for the variational problem (3.13):

3.6.1 Variable endpoint boundary conditions

Variable endpoint boundary conditions mean that γ is a stationary curve with respect to all admissible perturbations, i.e., it is the most observable type of centerpiece for a shearless coherent strip. As we show in Appendix 3.A, the only possible locations for variable endpoint boundary conditions are those satisfying

$$C\left(r(0)\right) = C\left(r(\sigma)\right) = \lambda I, \tag{3.14}$$

for some $\lambda > 0$. For an incompressible flow, we have $\lambda = 1$.

For completeness, we also consider another variable boundary condition in Appendix 3.A which results in non-zero Lagrangian shear (3.9) and hence are not discussed here.

3.6.2 Fixed endpoint boundary conditions

Fixed endpoint boundary conditions mean that γ is a stationary curve with respect to all perturbations that leave its endpoints fixed. In this case, we have

$$h(0) = h(\sigma) = 0. \tag{3.15}$$

These boundary conditions do not place restrictions on the admissible endpoints of γ. At the same time, a stationary curve under these boundary conditions is generally expected to be less robust or prevalent as a transport barrier than its variable-endpoint counterparts, given that it only prevails as a stationary curve under a smaller class of perturbations.

3.7 Equivalent geodesic formulation

Under the above two boundary conditions, we obtain from (3.13) the classic strong form of the Euler–Lagrange equations:

$$\partial_r p - \frac{d}{ds}\partial_{r'} p = 0, \tag{3.16}$$

a complicated second-order differential equation for $r(s)$.

As we show in Appendix 3.B, however, any γ satisfying (3.16) also satisfies

$$\delta\mathcal{P}_\mu(\gamma) = 0, \qquad \mathcal{P}_\mu(\gamma) = \int_\gamma H_\mu(r(s), r'(s))\,\mathrm{d}s, \qquad H_\mu(r(s), r'(s)) \equiv 0, \tag{3.17}$$

and hence represents a zero-energy stationary curve for the shear-energy-type functional

$$H_\mu(r, r') = \langle r', D(r)r'\rangle - \mu\sqrt{\langle r', C(r)r'\rangle\,\langle r', r'\rangle} \tag{3.18}$$

for some choice of the parameter μ.

Of special interest to us is the case of pointwise shearless curves, which we call *perfect shearless barriers*. Such barriers should prevail as influential transport barriers at arbitrarily small scales. Using the definition of the Lagrangian shear in (3.9), we conclude that curves with pointwise zero shear within the $H_\mu(r(s), r'(s)) \equiv 0$ energy surface all correspond to the parameter value $\mu = 0$.

For this value of μ, zero-energy stationary curves of the functional $\mathcal{P}_0(\gamma)$ are null-geodesics of the Lorentzian metric

$$g(u, v) = \langle u, D(x_0)v\rangle, \tag{3.19}$$

which has metric signature $(-, +)$ [104]. The metric g vanishes on its null-geodesics, and hence these null-geodesics satisfy the implicit first-order differential equation

$$\langle r'(s), D(r(s))r'(s)\rangle \equiv 0. \tag{3.20}$$

A direct calculation shows that all solutions of(3.20) satisfy

$$r'(s) \parallel \xi_i(r(s)), \qquad i = 1 \text{ or } 2, \tag{3.21}$$

therefore we obtain the following result.

Theorem 3.1. *Perfect shearless barriers are null-geodesics of the Lorentzian metric g, which are in turn composed of tensorlines of the Cauchy–Green strain tensor C.*

3.7.1 Hyperbolic barriers

The geodesic transport barrier theory developed in [23] proposed that hyperbolic LCS are individual strainlines and stretchlines that are most closely shadowed by locally most compressing and stretching geodesics, respectively, of the Cauchy–Green strain tensor C.

By contrast, here we have obtained from our shearless variational principle (3.12) that tensorlines of C are null-geodesics for the tensor D. Instead of comparing tensorlines to Cauchy–Green geodesics, therefore, one may simply locate hyperbolic LCSs as null-geodesics of D that

H1 stay bounded away from Cauchy–Green singularities (i.e., points where $C = I$), elliptic LCSs (see [23]) and parabolic LCSs (see below).

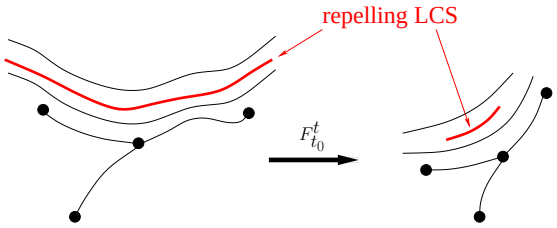

Figure 3.3: Schematic representation of the properties of a repelling LCS (red) among nearby strainlines (black) and Cauchy–Green singularities (dots). The repelling LCS stays away from singularities of Cauchy–Green singularities. While the length of any strainline shrinks as advected under the flow map $F^t_{t_0}$, the length of a repelling LCS shrinks more than any C^1-close strainline.

H2 admit an extremum for the averaged compression or stretching, respectively, among all their neighbors. These averages can be computed by averaging $\sqrt{\lambda_1(x_0)}$ and $\sqrt{\lambda_2(x_0)}$, respectively, along strainlines and stretchlines.

Condition (H1) is required to hold because material curves crossing Cauchy–Green singularities have zero tangential and normal stretching rates at the singularities, and hence lose their strict normal attraction or repulsion property. It implies that hyperbolic LCSs must satisfy Dirichlet boundary conditions, and none of their interior points can be Cauchy-Green singularities either. As a result, individual hyperbolic LCS are expected to fall in the less robust and prevalent class of shearless barriers, as discussed in Section 3.6.

Condition (H2) simply implements the definition of LCS as locally most repelling or attracting material curves, reducing an originally infinite-dimensional extremum problem to maximization within a one-dimensional family of strainlines or stretchlines. We summarize the implications of our shearless variational principle for hyperbolic LCS detection.

Proposition 3.1. [Hyperbolic LCS as shearless barriers] Hyperbolic LCSs at time t_0 are null-geodesics of the Lorentzian metric g that are bounded away from $C(x_0) = I$ singularities of the Cauchy–Green strain tensor. In addition, repelling LCSs have an average stretching smaller than that of any C^1 close null-geodesic of g (see Fig. 5.7 for an illustration). Furthermore, attracting LCSs have an average stretching larger than that of any C^1 close null-geodesic of g.

3.7.2 Parabolic barriers

Our main focus is to find generalized jet cores in the Lagrangian frame for unsteady flows of arbitrary time dependence. We shall refer to such generalized jet cores here as *parabolic transport barriers*.

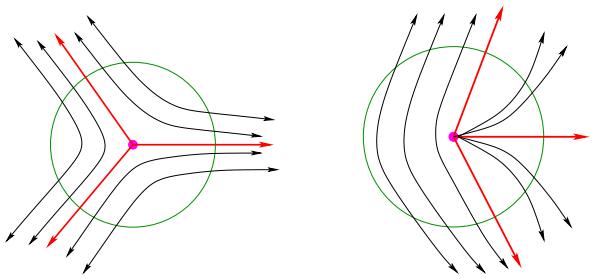

Figure 3.4: Topology of tensorlines (black) around a trisector (left) and a wedge (right) singularity (magenta). The tensorlines shown in red form the separatrices.

The general solution (3.21) of our variational principle certainly allows for further types of shearless barriers beyond hyperbolic LCSs. These further barriers are also composed of strainlines and stretchlines, but contain Cauchy–Green singularities and hence fail to be hyperbolic material lines. As discussed in section (3.6), such non-hyperbolic barriers are the most influential if they satisfy variable-endpoint boundary conditions for our shearless variational principle, i.e., their endpoints are Cauchy–Green singularities.

In addition, in order to provide a generalization of jet cores, we are interested in non-hyperbolic shearless barriers that have no distinct (repelling or attracting) stability type along their interior points. To this end, we require parabolic barriers to be also weak minimizers of their neutrality in the sense of Section 3.3.

Finally, for reasons of physical relevance and observability, our definition of a parabolic barrier will further restrict our consideration to strainline–stretchline chains that are unique between the two singularities they connect, and are also structurally stable with respect to small perturbations. Based on our review of tensorline singularities in Appendix 3.C, strainlines connecting singularities are only structurally stable and unique if they connect a *trisector* singularity to a *wedge* singularity (see Fig. 3.4). An identical requirement holds for stretchlines.

We then have the following definition.

Definition 3.1. [Parabolic barriers] Let γ denote the time t_0 position of a compact material line. Then this material line is a *parabolic transport barrier* over the time interval $[t_0, t]$ if the following two conditions are satisfied:

P1 γ is an alternating chain of strainlines and stretchlines, which is a unique connection between a wedge- and a trisector-type singularity of the tensor field $C(x_0)$ (see Fig. 3.5).

P2 Each strainline and stretchline segment in γ is a weak minimizer of its associated neutrality.

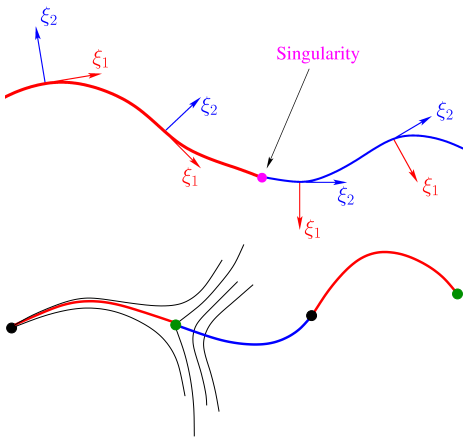

Figure 3.5: Top: Smooth connection of strainlines (red curve) and stretchlines (blue curve) only occurs at Cauchy–Green singularities. Bottom: An alternating chain of strainlines (red) and stretchlines (blue) connecting trisectors (green) and wedges (black). A schematic phase portrait of strainlines (thin black lines) is shown around one of the trisector singularities. The strainline marked by red color is the unique connection between that trisector and the wedge on its left.

Example 3.1. [*An FTLE trench is not necessarily a parabolic barrier*] Since our notion of a parabolic barrier requires a minimality condition on λ_2, one may speculate whether a trench of the Finite-Time Lyapunov Exponent (FTLE) field will always be a shearless barrier. Such an approach of detecting jet cores by trenches of the combined forward and backward FTLE field was considered in [100]. As advised in [100], the FTLE field should be used with caution for detecting parabolic barriers. While the trench of the FTLE field can indeed be an indicator of a jet core, the following example of a steady two-dimensional incompressible flow shows that this is not necessarily the case. Consider the incompressible flow

$$\begin{aligned} \dot{x} &= x\left(1+3y^2\right), \\ \dot{y} &= -(y+y^3). \end{aligned} \tag{3.22}$$

The line $y = 0$ is an invariant, attracting set, yet numerical simulations show that it is also a trench of the forward-time and backward-time FTLE field. Figure 3.6 shows the forward-time FTLE field and the tracer evolution around the line $y = 0$. The FTLE trench is a hyperbolic (attracting) LCS, as opposed to a parabolic barrier acting as a jet core.

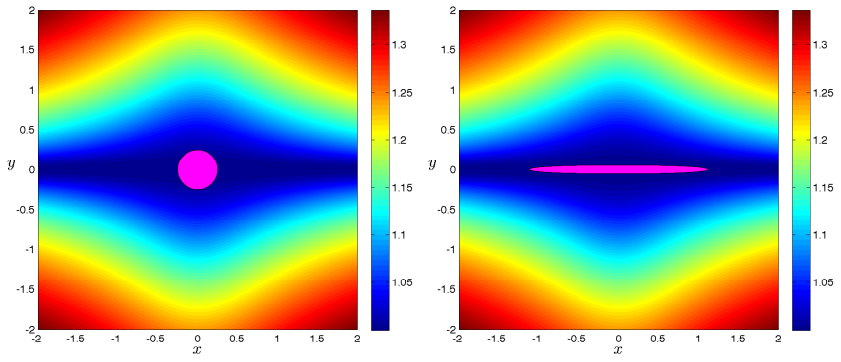

Figure 3.6: The tracer evolution for system (3.22). Left: Initial circular blob of tracers centered at the origin at time $t = 0$. Right: The advected tracer at time $t = 1.5$. The forward-time FTLE field with integration time $T = 10$ is shown in the background.

3.8 Automated numerical detection

Definition 3.1 provides the basis for the identification of parabolic barriers in finite-time flow data. Using the numerical details surveyed in Appendix 3.C, we implement conditions P1 and P2 of Definition 3.1 as follows:

1. Compute the Cauchy–Green strain tensor C on a two-dimensional grid in the (x_1, x_2) variables.

2. Detect the singularities of C by finding the common zeros of $f = C_{11} - C_{22}$ and $g = C_{12}$.

3. For any trisector singularity of the ξ_1 vector field, follow strainlines emanating from the singularity and identify among them the separatrices connecting the trisectors to wedges. Repeat the same procedure for the ξ_2 vector field to find trisector-wedge separatrices among stretchlines.

4. Out of the computed separatrices, keep the strainline separatrices satisfying
$$\left\langle \partial_r^2 \mathcal{N}_{\xi_1}(x_0)\xi_2(x_0), \xi_2(x_0) \right\rangle > 0,$$
and the stretchline separatrices satisfying
$$\left\langle \partial_r^2 \mathcal{N}_{\xi_2}(x_0)\xi_1(x_0), \xi_1(x_0) \right\rangle > 0.$$

5. Build smoothly connecting, alternating stretchline-strainline heteroclinic chains form the separatrices so obtained.

6. Finally, keep only the heteroclinic chains whose individual components are weak minimizers of their neutralities.

3.9 Numerical examples

3.9.1 Standard non-twist map

We first consider the standard non-twist map (SNTM)

$$\begin{aligned} x_{n+1} &= x_n + a\left(1 - y_{n+1}^2\right), \\ y_{n+1} &= y_n - b\sin(2\pi x_n), \end{aligned} \tag{3.23}$$

which was first studied in detail in [82], and has since become a generally helpful model in understanding shearless KAM curves in two-dimensional steady or temporally periodic incompressible flows.

For $b = 0$, the map (3.23) is a discretized version of the canonical parallel shear flow (3.1) with vanishing Eulerian shear along $y = 0$. For steady perturbations of (3.1), one still has a steady streamfunction whose dynamics is integrable and the shearless barriers can be understood as the lack of Hamiltonian twist. For $b \neq 0$, the SNTM corresponds to the evolution of a time-periodic perturbation of (3.1).

For the parameter values $a = 0.08$, $b = 0.125$, the SNTM is integrable and well-understood. We choose these parameters to illustrate the performance of our theory and extraction methodology for parabolic barriers. Figure 3.7 (left panel) shows the orbits of SNTM for these integrable parameters.

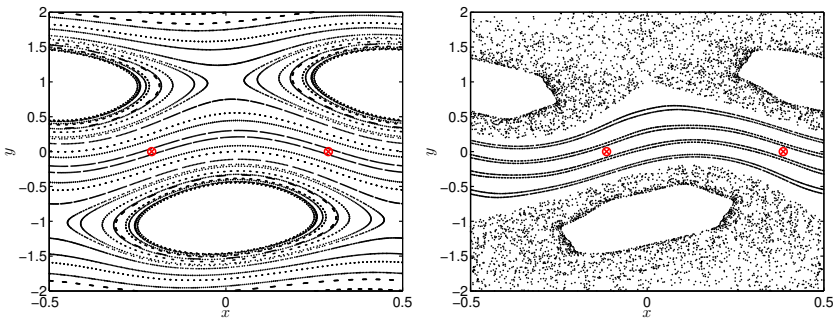

Figure 3.7: The Poincaré map for the standard non-twist map. Left: Integrable parameters: $a = 0.08$, $b = 0.125$ Right: Chaotic parameters: $a = 0.27$, $b = 0.38$. In both panels the red symbols $\otimes$ mark the indicator points (3.24).

In this integrable case, the location of shearless barriers is no longer trivial, but can be found by the theory of indicator points [105]. Specifically, initial conditions for the shearless barrier are given by

$$x = \frac{a}{2} \pm \frac{1}{4} \quad \text{and} \quad y = 0, \tag{3.24}$$

and the full barrier can be constructed by iterating these initial condition under the map (3.23). These initial conditions are referred to as indicator points

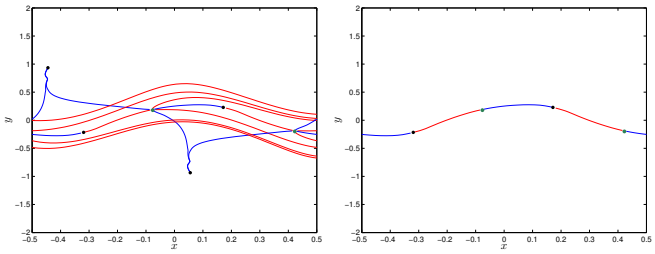

Figure 3.8: Left: Heteroclinic tensorlines between trisector and wedge singularities of the Cauchy–Green strain tensor in the integrable SNTM: strainlines (red) and stretchlines (blue). The black and green dots mark the wedge and trisector singularities, respectively. Right: The extracted parabolic barrier consists of the single alternating sequence of tensorlines that satisfy conditions P1-P2 of Definition 3.1.

and are shown in figure 3.7 for two choices of parameters (a, b). Therefore, we can compare the parabolic barrier computed from finitely many iterations of the SNTM using the steps in Section 3.8 with the exact asymptotic shearless barrier of the map given by indicator points.

Figure 3.8 shows all heteroclinic tensorlines connecting trisectors to wedges (left panel). In the domain $[-0.5, 0.5] \times [-2, 2]$ and for 100 iterations of the SNTM, we find 6 singularities: 2 trisectors (green dots) and 4 wedges (black dots). Only 4 alternating sequence of tensorlines satisfy conditions P1 and P2 of Definition 3.1. Figure 3.8 also shows the extracted parabolic barrier, i.e., a heteroclinic chain formed by four tensorlines (note the periodicity in x). This parabolic barrier represents the finite-time version of the exactly known asymptotic shearless KAM curve.

One can also compute the parabolic barrier for higher iterations of the SNTM map with the same procedure. As the number of iterations increase, the computed parabolic barrier converges to the exact asymptotic barrier. In Fig. 3.9, we show this convergence up to 300 iterations. For higher iterations, the two barriers become practically indistinguishable. The exact barrier (black curve) in Fig. 3.9 is computed from 200 iterations of the indicator points (3.24).

The evolution of circular tracers off and on the computed parabolic barriers is shown in Fig. 3.10 The purple tracer in the left plot of Fig. 3.10 is located on the computed parabolic barrier (red). The magenta and green tracers are centered on a tensorline (blue) that does not satisfy condition P2 of Definition 3.1. The images of all the tracers after 100 iterations of SNTM are shown in the right panel of Fig. 3.10. While the purple tracer undergoes a small boomerang-like deformation expected along parabolic barriers (jet cores), the other two tracer blobs experience substantial stretching. This illustrates that condition P2 is indeed essential in identifying parabolic barriers.

The SNTM (3.23) becomes chaotic for parameters $a = 0.27$, $b = 0.38$ (see

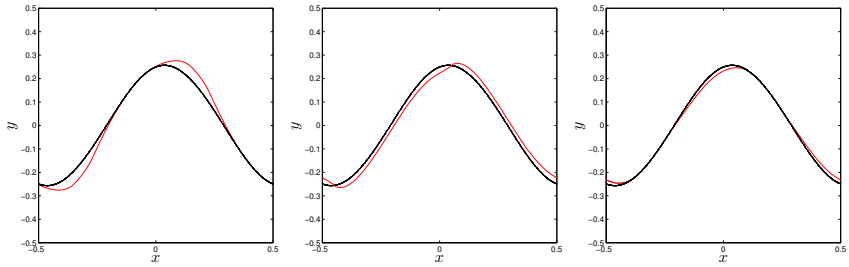

Figure 3.9: The red curve shows the computed finite-time shearless barrier from 100 (left), 200 (middle) and 300 (right) iterations of the integrable SNTM with parameters $a = 0.08$ and $b = 0.125$. The black curve marks the exact location of the barrier.

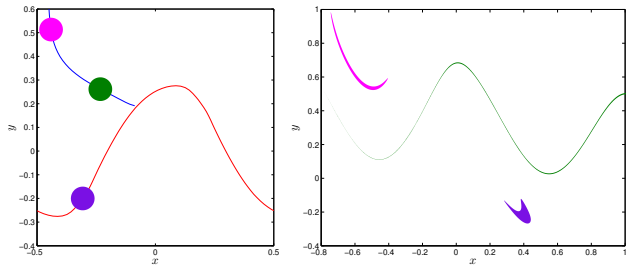

Figure 3.10: Parabolic barrier and its impact on tracers in the integrable SNTM.

figure 7, right panel). The theory of indicator points (see Eq. (3.24)) still applies and gives the exact asymptotic barrier for comparison. Figure 3.11 compares the computed parabolic barrier with the asymptotic shearless barrier. The parabolic barrier is constructed from 100 iterations of the SNTM while the exact barrier is computed from 200 iterations of the indicator point.

3.9.2 Passive particles in mean-field coupled non-twist maps

Following [106, 107], we consider the self-consistent mean field interaction of N coupled standard non-twist maps

$$\begin{aligned} x_{n+1}^k &= x_n^k + a\left(1 - \left(y_{n+1}^k\right)^2\right), \\ y_{n+1}^k &= y_n^k - b_{n+1}\sin(2\pi x_n^k - \theta_n), \end{aligned} \tag{3.25}$$

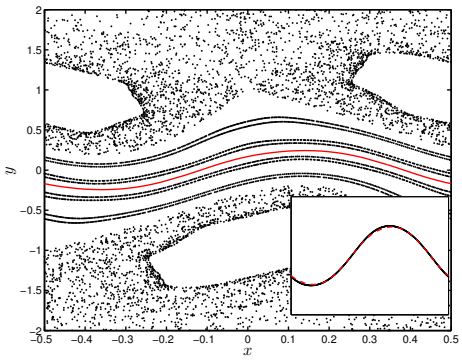

Figure 3.11: The chaotic SNTM with parameters $a = 0.27$, $b = 0.38$. The red curve shows the parabolic barrier computed from 100 iterations of SNTM. The inset compares the parabolic barriers with the exact asymptotic barrier (black curve) obtained by 200 iterations of the indicator points.

where $k = 1, \ldots, N$ is an index for the particles and n is the iteration number. The variables θ_n and b_n are given by

$$\begin{aligned} \theta_{n+1} &= \theta_n + \frac{1}{b_{n+1}} \frac{\partial \eta_n}{\partial \theta_n}, \\ b_{n+1} &= \sqrt{(b_n)^2 + (\eta_n)^2} + \eta_n, \end{aligned} \tag{3.26}$$

where

$$\eta_n = \sum_{i=1}^{N} \gamma_i \sin\left(x_n^i - \theta_n\right). \tag{3.27}$$

We refer to the particles x_n^i as *active* particles since they influence the mean field. The coefficients γ_i are the coupling constants.

Mean field models such as (3.25)-(3.27) take into account the fields that particles themselves generate, e.g. vorticity, charge or gravity. Such self-consistent models serve a middle ground between adding ad-hoc time dependence to a kinematic model and solving a PDE transport equation, and have been used to study problems in fluids [108, 106] and one-dimensional beam plasmas [106, 109].

The full mean-field system is $2N$-dimensional, and we consider the behavior of a *passive* particle, whose non-autonomous evolution is given by

$$\begin{aligned} x_{n+1} &= x_n + a\left(1 - y_{n+1}^2\right), \\ y_{n+1} &= y_n - b_{n+1} \sin(2\pi x_n - \theta_n), \end{aligned} \tag{3.28}$$

where b_n and θ_n are determined by the mean field of active particles. The evolution of a passive particle is similar to that of the SNTM considered in Section 3.9.1, but the parameters b_n and θ_n change under each iteration according to

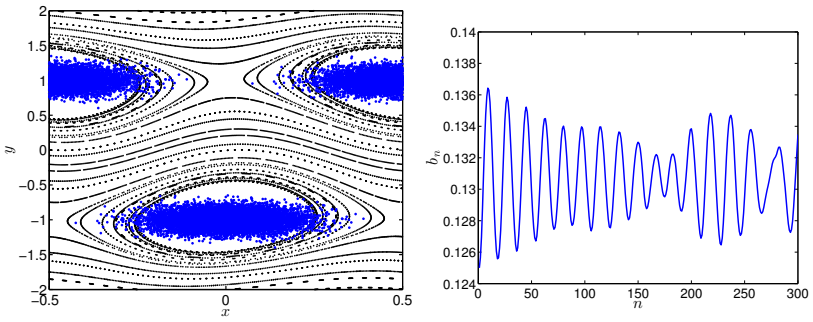

Figure 3.12: The evolution of coefficients b_n in equation (3.26) generated by the mean field interaction of $N = 2 \times 10^4$ active particles (x_n^k, y_n^k). Left: Initial conditions of the active particles. Right: Aperiodic evolution of b_n.

the mean field interaction of the active particles. When the coupling constants γ_i are zero, system (3.28) coincides with the autonomous SNTM (3.23).

We take $a = 0.08$ and $b_0 = 0.125$ and $\theta_0 = 0.0$. The corresponding dynamics for the SNTM (3.23) are integrable as described in the previous section. With these initial parameters, we place $N = 2 \times 10^4$ active particles localized near the islands (see Fig. 3.12) and compute their mean field evolution. The coupling constants γ_i are 2×10^{-5} for all i. The evolution of the parameter b_n is shown in Figure 3.12, and one thus sees that the evolution of a passive particle is aperiodic with respect to the iteration number.

With this setting, we compute all heteroclinic tensorlines using the automated algorithm described in Section 3.8. Shown in the left plot of Figure 3.13, the extracted heteroclinic tensorline geometry is more complicated than what we found for the SNTM. However, as seen in the right-side plot of the figure, the final subset of connections satisfying conditions P1-P2 of Definition 3.1 is similar to that of the integrable system. This implies the persistence of a parabolic shearless barrier for a passive tracer in a self-consistent mean-field model.

The evolution of tracers around the parabolic barrier is similar to that shown in Figure 3.10. Instead of presenting the tracer evolution, however, we illustrate the role of the parabolic barrier by placing two horizontal lines of particles above and two below the parabolic barrier (cf. left plot of Fig. 3.14). The middle and right plots in the same figure show the advected images of these lines after 50 and 100 iterations, respectively. We conclude that despite the generally chaotic mixing prevalent in the map, the extracted parabolic barrier provides a sharp and coherent dividing surface that inhibits transport of passive particles.

3.9.3 Bickley jet

As our last example, we consider an idealized model of an eastward zonal jet known as the Bickley jet [96, 97] in geophysical fluid dynamics. This model

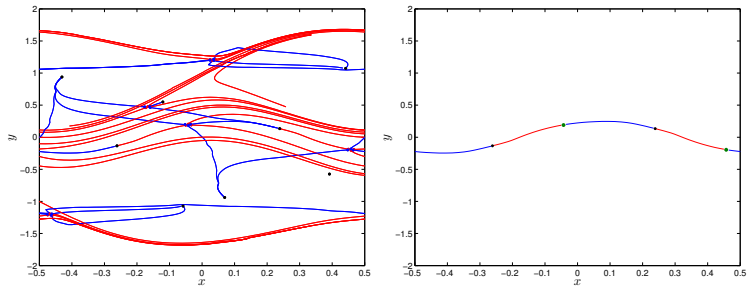

Figure 3.13: Left: Tensorlines for passive tracers in the mean-field coupled non-twist map (3.28): strainlines (red) and stretchlines (blue). Right: Parabolic barrier as an alternating sequence of tensorlines satisfying conditions P1-P2 of Definition 3.1. The black dots mark the wedge singularities where the tensorlines end and the green dots mark the trisector singularities.

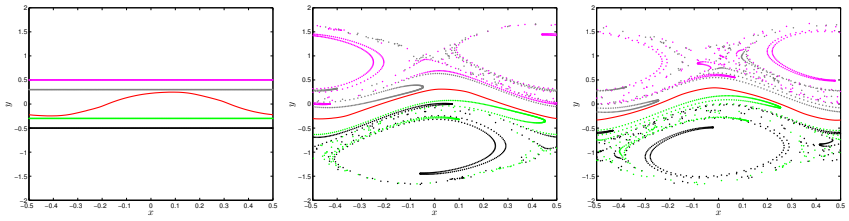

Figure 3.14: Tracer advection in the mean-field coupled non-twist map (3.28). Left: Parabolic barrier (red) and tracer particles (straight lines) at the initial time. Advected images of the parabolic barrier and tracer particles are shown after 50 iterations (middle) and 100 iterations (right)

consists of a steady background flow subject to a time-dependent perturbation. The time-dependent Hamiltonian for this model reads

$$\psi(x,y,t) = \psi_0(y) + \psi_1(x,y,t), \tag{3.29}$$

where

$$\psi_0(y) = -UL\tanh\left(\frac{y}{L}\right), \tag{3.30}$$

is the steady background flow and

$$\psi_1(x,y,t) = UL\mathrm{sech}^2\left(\frac{y}{L}\right)\mathrm{Re}\left[\sum_{n=1}^{3} f_n(t)\exp(\mathrm{i}k_n x)\right], \tag{3.31}$$

is the perturbation. The constants U and L are characteristic velocity and characteristic length scale, respectively. For the following analysis, we apply

the set of parameters used in [97]:

$$U = 62.66 \text{ ms}^{-1}, \quad L = 1770 \text{ km}, \quad k_n = 2n/r_0, \tag{3.32}$$

where $r_0 = 6371$ km is the mean radius of the earth.

Quasiperiodic Bickley jet

For $f_n(t) = \epsilon_n \exp(-\mathrm{i}k_n c_n t)$, the time-dependent part of the Hamiltonian consists of three Rossby waves with wave-numbers k_n traveling at speeds c_n. The amplitude of each Rossby wave is determined by the parameters ϵ_n. For small constant values of the parameters ϵ_n, the Bickley jet is known to have a closed, shearless jet core. In [100], it is shown numerically that this jet core is marked by a trench of the forward- and backward-time FTLE fields. This finding is a consequence of temporal quasi-periodicity of Rossby waves, which renders the forward- and backward-time dynamics as similar. In general, however, the time-dependence $f_n(t)$ can be any smooth signal [23] with no particular recurrence. We focus here on the existence of the shearless jet core under such general forcing functions.

First, however, we compare our results with those of [100] for the quasi-periodic forcing $f_n(t) = \epsilon_n \exp(-\mathrm{i}k_n c_n t)$, with constant amplitudes $\epsilon_1 = 0.075$, $\epsilon_2 = 0.4$ and $\epsilon_3 = 0.3$. The top plot of Fig. 3.15 shows automatically extracted heteroclinic tensorlines initiated from trisectors and ending in wedges. Out of all these connections, three satisfy conditions P1-P2 of Definition 3.1 and hence qualify as parabolic barriers (bottom plot of Fig. 3.15).

The closed (x-periodic) parabolic barrier in red has also been obtained in [100] as a trench of both the forward and the backward FTLE field. The other two open parabolic barriers (blue and black), however, have remained undetected in previous studies to the best of our knowledge. These two open barriers do not appear as the trenches of forward-time plus backward-time FTLE fields (see [100], figure 2). Yet these open parabolic barriers do serve as cores of smaller-scale jets, as demonstrated by the distinct boomerang-shaped patterns developed by tracer blobs initialized along them (see Fig. 3.16).

Such shearless material curves do not exist in the steady or time-periodic counterpart of the Bickley jet, and thus perturbative theories, such as KAM-type arguments, would not predict the existence of such a jet core. Moreover, since these curves are not closed barriers separating the phase space they cannot be detected as almost-invariant coherent sets [110].

Chaotically forced Bickley jet

To generate chaotic forcing for the Bickley jet, we let the forcing amplitudes ϵ_n be a chaotic signal for $n = 1, 2$. The forcing amplitude $\epsilon_3 = 0.3$ remains constant. Figure 3.17, shows the chaotic signals $\epsilon_1(t)$ and $\epsilon_2(t)$.

Figure 3.18 shows the single parabolic barrier obtained from the automated extraction procedure described in Section 3.8. The additional open parabolic

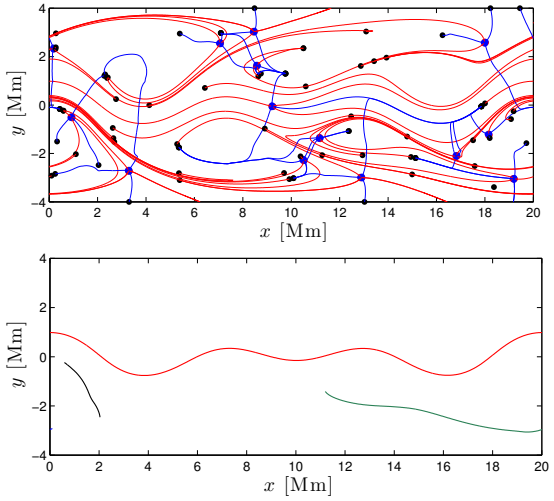

Figure 3.15: Top: Tensorlines for the quasi-periodically forced Bickley jet: strainlines (red) and stretchlines (blue). The black dots mark the wedge singularities where the tensorlines end while the blue dots mark the trisectors where the tensorlines are initiated from. Bottom: Automatically extracted parabolic barriers in the quasiperiodic Bickley jet.

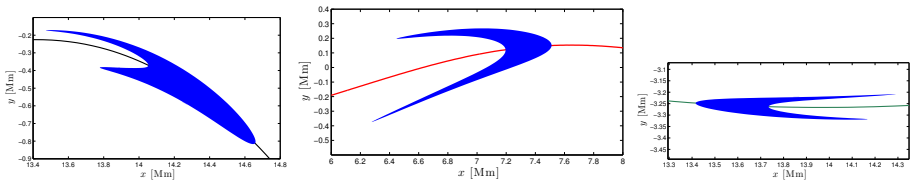

Figure 3.16: The deformation of initially circular tracers (of radii 0.2 Mm) centered on the shearless curves after 11 days. The color of the curves correspond to those of Fig. 3.15.

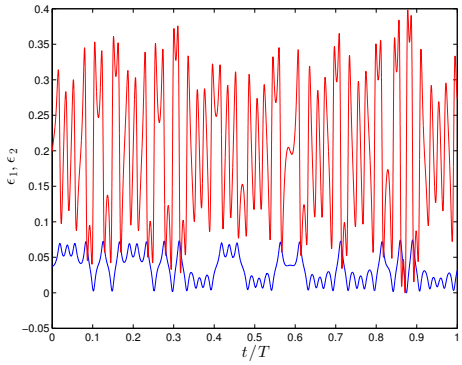

Figure 3.17: The chaotic signals ϵ_1 (blue) and ϵ_2 (red) used as the amplitude of the forcing in equation (3.31). The integration time T is 11 days.

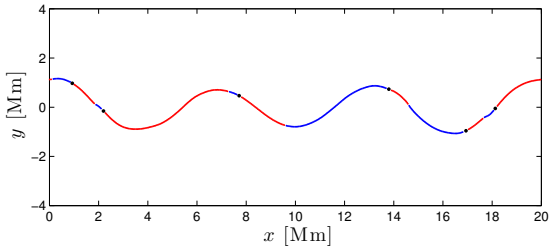

Figure 3.18: The shearless curve for the chaotically forced Bickley jet. The shearless curve consists of alternating sequence of strainlines (red) and stretchlines (blue). The wedge singularities are marked by black dots.

barriers found in the quasi-periodically forced case are, therefore, destroyed under chaotic forcing.

The dynamic role of the remaining single barrier is illustrated in Fig. 3.19, where initially straight lines of passive particles are advected for 6, 9 and 11 days. Despite widespread chaotic mixing, the parabolic barrier preserves its coherence, showing no stretching, folding, or smaller-scale filamentation. Therefore, the extracted parabolic barrier is a sharp separator between two invariant mixing regions. This shows that beyond the almost-invariant sets located for the Bickley jet by set-theoretical methods [111, 110], actual invariant sets with sharp, coherent boundaries also exist for the parameter values considered here.

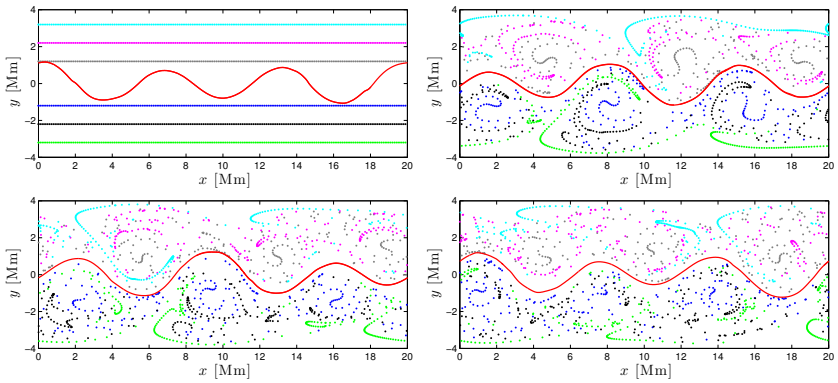

Figure 3.19: Chaotically forced Bickley jet. The closed shearless curve (red) and tracer particles (dots) at time $t = 0$ (top left). Their advected images are shown after 6 days (top right) 9 days (bottom left) and 11 days (bottom right).

3.10 Conclusion

We have developed a variational principle for shearless material lines in two-dimensional, non-autonomous dynamical systems. Solutions to this principle turn out to be composed of tensorlines of the Cauchy–Green strain tensor. Locally most stretching or contracting tensorlines staying away from singularities of the Cauchy–Green strain tensor are found to be hyperbolic Lagrangian Coherent Structures (LCSs). Thus, the present results give the first global variational description of hyperbolic LCS as shearless material curves.

By contrast, special chains of alternating tensorlines between Cauchy–Green singularities define another class of shearless barriers, which we call parabolic barriers (or parabolic LCSs). These barriers satisfy variable-endpoint boundary conditions in the underlying Euler-Lagrange equation, which make them exceptionally robust with respect to a broad class of perturbations. This explains the broadly reported robustness of shearless barriers observed in physical systems.

We have devised an algorithm for the automated numerical detection of parabolic barriers in two-dimensional unsteady flows. We illustrated this algorithm on the standard non-twist map (SNTM), passive tracers in mean-field coupled SNTMs and a model of the zonal jet (known as the Bickley jet). For the SNTM, we showed that under increasing iterations, our parabolic barrier converges to the exact shearless curve predicted by the theory of indicator points.

For the Bickley jet, we have recovered the results of [100] on closed zonal jet cores under quasi-periodic forcing. We have also found, however, other open jet cores in the same setting that were not revealed by previous studies. A zonal jet was also detected in a chaotically forced Bickley jet.

Jet streams are known to exist and play an important role in geophysical flows [112]. The temporal aperiodicity and spatially complicated meandering

shape of these jets have impeded their accurate detection. Our variational method provides a general framework for their extraction from numerical or observational geophysical flow data.

While higher-dimensional shearless barriers have not yet been studied extensively, the variational methods developed here should extend to higher-dimensional flows. Such an extension of the concept of a parabolic barrier appears to be possible via the approach developed recently for elliptic and hyperbolic transport barriers in three-dimensional unsteady flows [25].

Appendix 3.A Derivation of variable-endpoint boundary conditions

Note that

$$\partial_{r'}p = \frac{[2\langle r', Cr'\rangle\langle r', r'\rangle D - \langle r', Dr'\rangle\langle r', r'\rangle C - \langle r', Dr'\rangle\langle r', Cr'\rangle I]r'}{\sqrt{\langle r', Cr'\rangle\langle r', r'\rangle}^3} \tag{3.33}$$

Defining

$$M := \frac{2\langle r', Cr'\rangle\langle r', r'\rangle D - \langle r', Dr'\rangle\langle r', r'\rangle C - \langle r', Dr'\rangle\langle r', Cr'\rangle I}{\sqrt{\langle r', Cr'\rangle\langle r', r'\rangle}^3}, \tag{3.34}$$

we have

$$\partial_{r'}p = Mr'.$$

Any perturbation h can be written as $h = h_\parallel + h_\perp$ where $h_\parallel$ and $h_\perp$ are, respectively, the tangential and orthogonal components of h with respect to r'. Therefore, the boundary term in (3.13) can be written as

$$\langle \partial_{r'}p, h\rangle = \langle Mr', h_\perp\rangle. \tag{3.35}$$

Note that the term $\langle Mr', h_\parallel\rangle$ vanishes since $\langle Mr', r'\rangle = 0$.

Since $h_\perp$ is a scalar multiple of $\Omega r'$, the boundary term $\langle \partial_{r'}p, h\rangle$ vanishes if and only if $\langle Mr', \Omega r'\rangle = 0$. Now expanding r' in the Cauchy–Green eigenbasis as $r' = \alpha\xi_1 + \beta\xi_2$, we get

$$\langle Mr', \Omega r'\rangle = \frac{(\alpha^2\lambda_1 + \beta^2\lambda_2)(\alpha^2 - \beta^2)(\lambda_2 - \lambda_1) - \alpha^2\beta^2(\lambda_2 - \lambda_1)^2}{(\alpha^2 + \beta^2)^{1/2}(\alpha^2\lambda_1 + \beta^2\lambda_2)^{3/2}}, \tag{3.36}$$

where we used the fact that $C\xi_i = \lambda_i\xi_i$ for $i = 1, 2$. Without loss of generality, we may assume that the tangent vector r' is normalized such that $\alpha^2 + \beta^2 = 1$.

Clearly if $\lambda_2 = \lambda_1$, $\langle Mr', \Omega r'\rangle$ vanishes and so does the boundary term $\langle \partial_{r'}p, h\rangle$. By definition, the eigenvalues λ_1 and λ_2 only coincide at the Cauchy–Green singularities, where $C = \lambda I$. This proves the condition (3.14).

Alternatively, assuming $\lambda_1 \neq \lambda_2$, we find that $\langle Mr', \Omega r'\rangle = 0$ if and only if

$$\alpha = \pm\sqrt{\frac{\sqrt{\lambda_2}}{\sqrt{\lambda_1} + \sqrt{\lambda_2}}}, \quad \beta = \pm\sqrt{\frac{\sqrt{\lambda_1}}{\sqrt{\lambda_1} + \sqrt{\lambda_2}}}.$$

In other words, for the boundary term $\langle \partial_{r'} p, h \rangle$ to vanish, the tangent vectors r' at the endpoints of γ must satisfy

$$r' = \sqrt{\frac{\sqrt{\lambda_2}}{\sqrt{\lambda_1}+\sqrt{\lambda_2}}}\,\xi_1 \pm \sqrt{\frac{\sqrt{\lambda_1}}{\sqrt{\lambda_1}+\sqrt{\lambda_2}}}\,\xi_2.$$

The above linear combination of the Cauchy–Green eigenvectors is referred to as the *shear vector field* [23]. *Shearlines*, i.e. the solution curves of the shear vector field, have been shown to mark boundaries of coherent regions of the phase space [23, 53, 113], e.g., generalized KAM tori and coherent eddy boundaries.

Shear vector fields, however, do not result in shearless transport barriers; in fact, they are local maximizers of Lagrangian shear [23].

Appendix 3.B Equivalent formulation of the variational principle

With the shorthand notation

$$A(r,r') = \langle r', C(r) r' \rangle, \quad B(r') = \langle r', r' \rangle, \quad G(r,r') = \langle r', D(r) r' \rangle, \tag{3.37}$$

P can be rewritten as

$$P(\gamma) = \frac{1}{\sigma}\int_0^\sigma p(r,r')\,\mathrm{d}s = \frac{1}{\sigma}\int_0^\sigma \frac{G(r,r')}{\sqrt{A(r,r')B(r')}}\,\mathrm{d}s, \tag{3.38}$$

and its Euler–Lagrange equations (3.16) can be re-written as

$$\partial_r \frac{G}{\sqrt{AB}} - \frac{\mathrm{d}}{\mathrm{d}s}\partial_{r'}\frac{G}{\sqrt{AB}} = 0. \tag{3.39}$$

Since the integrand of $P(\gamma)$ has no explicit dependence on the parameter s, Noether's theorem [114] guarantees the existence of a first integral for (3.39). This integral can be computed as

$$I = \frac{G}{\sqrt{AB}} - \left\langle r', \partial_{r'}\frac{G}{\sqrt{AB}} \right\rangle = \frac{G}{\sqrt{AB}} = \mu = \text{const.}, \tag{3.40}$$

where we have used the specific form of the functions A and B from (3.37), as well as the second equation from (4.6). We further used the fact that $\langle r', \partial_{r'}\frac{G}{\sqrt{AB}}\rangle = \langle r', \partial_{r'} p\rangle = \langle r', Mr'\rangle = 0$ where the last identity follows from the definition (3.34) of the tensor M.

We therefore have the identity

$$G(r(s), r'(s)) \equiv \mu\sqrt{A(r(s), r'(s))B(r'(s))}, \tag{3.41}$$

for any solution of (3.39) for some appropriate value of the constant μ .

Note that

$$\partial_r \frac{G}{\sqrt{AB}} = \frac{\partial_r G}{\sqrt{AB}} - \frac{G\left(B\partial_r A + A\partial_r B\right)}{2\sqrt{AB}^3}, \quad \partial_{r'} \frac{G}{\sqrt{AB}} = \frac{\partial_{r'} G}{\sqrt{AB}} - \frac{G\left(B\partial_{r'} A + A\partial_{r'} B\right)}{2\sqrt{AB}^3}. \tag{3.42}$$

Using the identity (3.41), we rewrite the expressions (4.6) as

$$\partial_r \frac{G}{\sqrt{AB}} = \frac{1}{\sqrt{AB}} \partial_r \left[G - \mu\sqrt{AB}\right], \quad \partial_{r'} \frac{G}{\sqrt{AB}} = \frac{1}{\sqrt{AB}} \partial_{r'} \left[G - \mu\sqrt{AB}\right]. \tag{3.43}$$

Substituting these expressions in the Euler–Lagrange equation (3.39), we get

$$\frac{1}{\sqrt{AB}} \partial_r \left[G - \mu\sqrt{AB}\right] - \frac{\mathrm{d}}{\mathrm{d}s} \frac{1}{\sqrt{AB}} \partial_{r'} \left[G - \mu\sqrt{AB}\right] = 0. \tag{3.44}$$

In order to further simplify equation (3.44), one would ideally want to remove the common denominator $\sqrt{AB}$ from the equation by an appropriate rescaling of the independent variable s. This suggests the introduction of a new independent variable τ via the formula

$$\frac{\mathrm{d}\tau}{\mathrm{d}s} = \sqrt{A(r(s), r'(s))B(r'(s))}, \tag{3.45}$$

which, by the chain rule, implies

$$\sqrt{A(r(s), r'(s))B(r'(s))} = \frac{1}{\sqrt{A(r(\tau), \dot{r}(\tau))B(\dot{r}(\tau))}}, \tag{3.46}$$

with the dot referring to differentiation with respect to the new variable τ. Note that $\sqrt{A(r(s), r'(s))B(r'(s))}$ is non-vanishing on smooth curves with well-defined tangent vectors, and hence the change of variables (3.45) is well-defined.

After the $s \mapsto \tau$ rescaling and the application of (3.46), the expressions in (3.43) imply

$$\partial_r \frac{G(r, r')}{\sqrt{A(r, r')B(r')}} = \frac{\partial_r \left[G(r, \dot{r}) - \mu\sqrt{A(r, \dot{r})B(\dot{r})}\right]}{\sqrt{A(r(\tau), \dot{r}(\tau))B(\dot{r}(\tau))}} \tag{3.47}$$

$$\frac{\mathrm{d}}{\mathrm{d}s} \partial_{r'} \frac{G(r, r')}{\sqrt{A(r, r')B(r')}} = \frac{\frac{\mathrm{d}}{\mathrm{d}\tau} \partial_{\dot{r}} \left[G(r, \dot{r}) - \mu\sqrt{A(r, \dot{r})B(\dot{r})}\right]}{\sqrt{A(r(\tau), \dot{r}(\tau))B(\dot{r}(\tau))}}. \tag{3.48}$$

Based on these identities, equation (3.39) can be re-written as

$$\frac{1}{\sqrt{A(r(\tau), \dot{r}(\tau))B(\dot{r}(\tau))}} \left\{ \partial_r \left[G(r, \dot{r}) - \mu\sqrt{A(r, \dot{r})B(\dot{r})}\right] - \frac{\mathrm{d}}{\mathrm{d}\tau} \partial_{\dot{r}} \left[G(r, \dot{r}) - \mu\sqrt{A(r, \dot{r})B(\dot{r})}\right] \right\} = 0. \tag{3.49}$$

Since $1/\sqrt{A(r(\tau),\dot{r}(\tau))B(\dot{r}(\tau))}$ is non-vanishing we obtain from (3.49) that all solutions of (3.39) must satisfy the Euler–Lagrange equation derived from the Lagrangian

$$\mathcal{H}_\mu(r,\dot{r}) = \frac{1}{2}\left[G(r,\dot{r}) - \mu\sqrt{A(r,\dot{r})B(\dot{r})}\right]. \tag{3.50}$$

Therefore, all stationary functions of the functional P are also stationary functions of the functional $\mathcal{H}_\mu$ for an appropriate value of μ. This value of μ can be determined from formula (3.41), which also shows that the corresponding stationary functions of $\mathcal{H}_\mu$ all satisfy

$$\langle \dot{r}(\tau), D(r(\tau))\dot{r}(\tau)\rangle = \mu\sqrt{A(r,\dot{r})B(\dot{r})}. \tag{3.51}$$

For $\mu = 0$, these solutions are null-geodesics of the Lorentzian metric (3.19) induced by the tensor D.

Conversely, assume that $r(\tau)$ satisfies both equations (3.49) and (3.51). Reversing the steps leading to (3.51), and employing the inverse rescaling of the independent variable as,

$$\frac{\mathrm{d}s}{\mathrm{d}\tau} = \sqrt{A(r(\tau),\dot{r}(\tau))B(\dot{r}(\tau))}, \tag{3.52}$$

we obtain that any rescaled solution $r(s)$ is also a solution of the Euler–Lagrange equation (3.39). Therefore, each solution of (3.49) lying in the zero energy surface $\mathcal{H}_\mu(r,\dot{r}) = 0$ is also a stationary curve of the functional $P(\gamma)$, lying on the energy surface $I(r,r') = \mu$, and hence satisfying the identity (3.41).

Appendix 3.C Tensorline singularities

In the numerical detection of shearless barriers described in Section 3.8, it is crucial to detect singularities of the Cauchy-Green strain tensor, and to classify the singularity type as either a wedge or a trisector. This Appendix elaborates on the numerical methods for singularity detection and classification that were used in the preceding computations.

3.C.1 Tensorline singularities

Singularities of tensorlines, such as the tensorlines of the Cauchy–Green strain tensor, are points where the tensor field becomes the identity tensor, and hence ceases to admit a well-defined pair of eigenvectors. As a consequence, tensorlines, as curves tangent to ξ_1 and ξ_2 eigenvector fields, are no longer defined at singularities. Still, the behavior of tensorlines near a singularity has some analogies, as well as notable differences, with the behavior of trajectories of a two-dimensional vector field near fixed point. In the absence of symmetries, there are two structurally stable singularities of a tensorline field: trisectors and wedges.

Trisector singularities are similar to saddle points in two-dimensional flows, except that they have three (as opposed to two) distinguished strainlines asymptotic to them (Fig. 3.4).

Wedge singularities are a mix between a saddle and a source or a sink. On the one hand, there is a continuous family of infinitely many neighboring tensorlines asymptotic to a wedge. At the same time, a wedge also has discrete tensorlines asymptotic to it, resembling the stable and unstable manifolds of a saddle (Fig. 3.4).

3.C.2 Numerical detection of singularities

At a singularity in an incompressible flow, the elements of the Cauchy–Green strain tensor satisfy

$$C_{11} - C_{22} = 0 \quad \text{and} \quad C_{12} = 0, \tag{3.53}$$

where C_{ij} is the (i,j) the entry of C. The singularities are, therefore, precisely points where the zero level-curves of the scalar functions $f = C_{11} - C_{22}$ and $g = C_{12}$ intersect.

The discrete values of f and g are available on the computational grid. In order to find the intersection of the zero level-curves $f = 0$ and $g = 0$, one needs to perform some interpolation (bilinear, bicubic, etc.) to approximate f and g inside each grid.

A computationally faster approach is to restrict the function f to the edges of the computational grid (i.e., the straight lines connecting the neighboring grid points). This restriction is a scalar function of a single variable. Then using a linear interpolation, we approximate the functions along each edge. This allows us to approximate the intersection of the contour $f = 0$ and each edge (if it exists). Repeating the same procedure for g, we approximate the intersection of the level curve $g = 0$ and the edges. From this information, we decide whether the zero level-curves of f and g intersect inside the grid cell.

In regions of high mixing and chaos, the numerical values of the entries of the Cauchy–Green strain tensor can be large and noisy, due to the exponential growth of numerical errors. These noisy points result in spurious intersection of the zero level-curves of f and g, and hence spurious singularity detection.

An indication of noise in an incompressible flow is that the determinant of C, i.e. $\lambda_1\lambda_2$, is far from its theoretical value of 1. To discard these regions (that are not of interest in the present study), we examine the deviation of $|\lambda_2\lambda_1 - 1|$ from zero. If this deviation is large (here, $|\lambda_2\lambda_1 - 1| > 1$) around a detected singularity, we render the singularity as spurious and discard it.

3.C.3 Numerical classification of singularities

Once the singularities are located, we need a robust procedure to classify each of these singularities as a wedge or a trisector. The existing methods for distinguishing trisector singularities of a tensor field from its wedge singularities

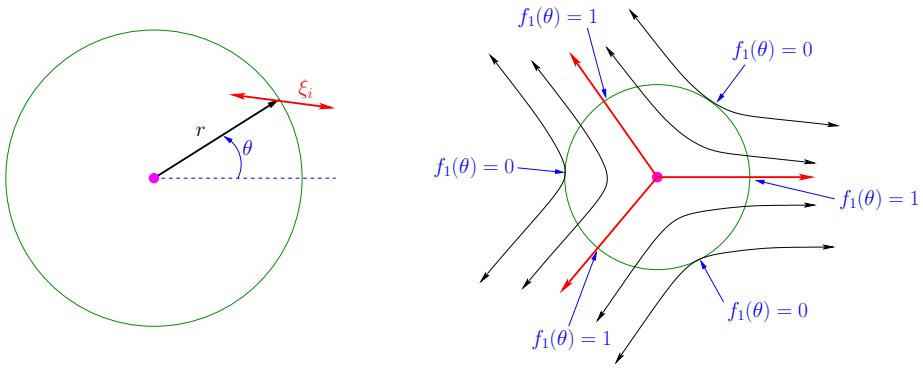

Figure 3.20: Left: In equation (3.54), $f_i(\theta)$ is defined, around a singularity, as the normalized inner product of r and ξ_i. Right: The strainlines (black and red curves) around a trisector singularity. The function $f_1(\theta)$ assumes the values 0 and 1 three times, with 0's and 1's alternating. The θ-values with $f_1(\theta) = 1$ correspond to the direction of separatrices (red). Similar statements hold for stretchlines and the function $f_2(\theta)$ around a trisector.

require further differentiation of the tensor field [102]. In our experience, this introduces further noise affecting the robustness of the results. Here, we introduce a differentiation-free method for identifying trisectors and wedges. This method also is used to find the direction of the separatrices emanating from a trisector.

A distinguishing geometric feature of a trisector singularity is the three separatrices emanating from it. Close enough to the singularity, these separatrices are close to straight lines. Therefore, the separatrices will be approximately perpendicular to a small circle centered at the singularity. Consequently, the intersection of the trisectors with the circle approximately maximizes the quantity

$$f_i(\theta) = \frac{|\langle \xi_i, r \rangle|}{|\xi_i|\,|r|}, \quad i = 1, 2 \tag{3.54}$$

associated with the vector field ξ_i, where r is the vector from the singularity pointing towards the point θ on the small circle (Figure 3.20, left panel).

For a trisector, $f_i(\theta)$ assumes the value 0 and 1 three times, with 0's and 1's alternating, as θ increases from 0 to 2π (Figure 3.20, right panel). In contrast, for a wedge, f_i assumes 1 three times, and assumes a zero value only once. We use this difference between wedges and trisectors in identifying them numerically.

Moreover, for a trisector, the θ values for which $f_i(\theta) = 1$ indicate the direction of its separatrices corresponding to the vector field ξ_i.

3.C.4 Structurally stable heteroclinic tensorlines and their numerical detection

As seen in Fig. 3.4, the set of orbits asymptotic to any wedge form a closed set of nonzero area. If two such sets intersect, the intersection is either structurally unstable (i.e., involves just the boundary of the two sets), or it includes a nonzero area filled by curves. The former intersection can be broken by small perturbations, whereas the latter intersection necessarily contains infinitely many orbits. Therefore, there can be no unique, structurally stable connection between two wedges.

As also seen in Fig. 3.4, there are always precisely three distinct orbits asymptotic to a given trisector. Any possible heteroclinic connection between two trisectors, therefore, lies in the non-transverse intersection of two one-dimensional curves, which can be broken by small perturbations. As a result, trisector-trisector connections are necessarily structurally unstable.

We conclude that the only types of tensorlines connecting two singularities of the Cauchy–Green strain tensor in a locally unique and structurally stable fashion are trisector-wedge connections. Such a connection backward asymptotes to a trisector and forward asymptotes into the attracting set of a wedge. Small perturbations keep the trisector, and deform its outgoing orbit by a small amount. Therefore, the deformed orbit still hits the (slightly deformed) attracting set of the wedge under small enough perturbations.

The numerical detection of trisector-wedge connections proceeds by tracking the separatrices leaving a trisector (see figure 3.20, right panel), and monitoring whether they enter the attracting sector of a small circle surrounding a wedge (see figure 3.5).

Chapter 4

The Maxey–Riley Equation: Existence, Uniqueness and Regularity of Solutions

4.1 Introduction

The Maxey–Riley (MR) equation [115–117] describes the motion of a small but finite-sized rigid sphere through a fluid. The equation is widely used to study the motion of a finite-size (or inertial) particle immersed in a non-uniform fluid. The behavior of such particles is of interest in various environmental and engineering problems, e.g., clustering of garbage patches in the oceans [118] and dispersion of airborne pollutants [119].

To recall the exact form of the MR equation, we let $u : \mathcal{D} \times \mathbb{R}^+ \to \mathbb{R}^n$ denote the velocity field describing the flow of a fluid in an open spatial domain $\mathcal{D} \subseteq \mathbb{R}^n$, where $n = 2$ or $n = 3$ for two- or three-dimensional flows, respectively. A fluid trajectory is then the solution of the differential equation $\dot{x} = u(x, t)$ with some initial condition $x(0) = x_0$. A spherical inertial particle, however, follows a different trajectory $y(t) \in \mathcal{D}$, which satisfies the MR equation

$$\begin{aligned}\ddot{y} = &\frac{R}{2}\frac{D}{Dt}\left(3u(y,t) + \frac{\gamma}{10}\mu^{-1}\Delta u(y,t)\right) + \left(1 - \frac{3R}{2}\right)g \\ &- \mu\left(\dot{y} - u(y,t) - \frac{\gamma}{6}\mu^{-1}\Delta u(y,t)\right) \\ &- \kappa\mu^{1/2}\left\{\int_0^t \frac{\dot{w}(s)}{\sqrt{t-s}}\mathrm{d}s + \frac{w(0)}{\sqrt{t}}\right\},\end{aligned} \tag{4.1}$$

where

$$w(t) = \dot{y}(t) - u(y(t), t) - \frac{\gamma}{6}\mu^{-1}\Delta u(y(t), t). \tag{4.2}$$

The initial conditions for the inertial particle are given as $y(0) = y_0$ and $\dot{y}(0) = v_0$. The material derivative $\frac{D}{Dt} \doteq \partial_t + u \cdot \nabla$ denotes the time derivative along a fluid trajectory.

The dimensionless parameters in (4.1) are

$$R = \frac{2\rho_f}{\rho_f + 2\rho_p}, \ \mu = \frac{R}{St}, \ \kappa = \sqrt{\frac{9R}{2\pi}}, \ \gamma = \frac{9R}{2\mathrm{Re}}, \tag{4.3}$$

where ρ_f and ρ_p are the density of the fluid and the particle, respectively; the constant of gravity is denoted by g. The Stokes (St) and Reynolds (Re) numbers are defined as

$$\mathrm{St} = \frac{2}{9}\left(\frac{a}{L}\right)^2 \mathrm{Re}, \quad \mathrm{Re} = \frac{UL}{\nu}, \tag{4.4}$$

where a is the radius of the particle, U and L refer, respectively, to characteristic velocity and characteristic length scale of the fluid and ν denotes the kinematic viscosity of the fluid.

Equation (4.1) is a second-order, nonlinear system of implicit integro-differential equations with a singular kernel and with a term that grows unbounded as $t \to 0$. The implicit nature of the equation is due to the *memory (or Basset–Boussinesq) term*, whose integrand is a function of the particle acceleration $\ddot{y}$. The integral also has a singular but integrable kernel. Physically, the memory term accounts for the effect of the boundary layer development around the particle, as it moves through the fluid [120].

Without the memory term and for $w(0) = 0$, the MR equation is an ordinary differential equation, whose solutions are well known to be regular for any smooth ambient velocity field $u(x, t)$. The memory term, however, introduces complications in the analysis and numerical solution of the equation. For this reason, this term has routinely been neglected in studies of inertial particle dynamics (see, e.g., Maxey [121], Babiano et al. [122], Haller and Sapsis [123]), until recent studies [124, 125] demonstrated convincingly the quantitative and qualitative importance of the memory term.

The full MR equation, however, represents a complicated problem, even for $w(0) = 0$. Because of its implicit nature, it is not a priori clear if the MR differential equation defines a dynamical system, i.e., a process with a well-defined flow map. The equation is certainly not solvable with standard numerical schemes such as Runge–Kutta algorithms. To this end, involved schemes have been developed for numerical treatment of the memory term (see Daitche [126] and the references therein).

All these numerical schemes implicitly assume the existence and uniqueness of solutions of the MR equation. The solutions can indeed be found explicitly for certain simple velocity fields [127, 124]. To the best of our knowledge, however, general existence and uniqueness results have not been proven, and cannot be directly concluded from existing results on broader classes of evolution equations (see [128–131] for related but not applicable results on integro- and fractional-order differential equations). In the absence of such results, the existence and regularity of solutions for an implicit integro-differential equation with a singular kernel, such as the MR equation, is far from obvious.

When nonzero, the unbounded term $w(0)/\sqrt{t}$ further complicates equation (4.1), imparting an instantaneously infinite force at the initial time. This term is also routinely ignored for convenience, even though its omission imposes a special constraint on the initial particle velocity that is hard to justify physically [132].

Here, we present the first proof of local existence and uniqueness of weak solutions to the full MR equation. The solutions become classical (strong) solutions to (4.1) for initial conditions satisfying $w(0) = 0$. Moreover, we show that both the weak and the strong solutions are continuously differentiable with respect to their initial conditions. As a consequence, coherent-structure detection methods utilizing the derivative of the flow map in the absence of the memory term [133] can also be employed in the present, more general context.

We start with re-writing the MR equation as a system of differential equations (see Eq. (4.7) bellow) in terms of the particle position y and the function w defined in (4.2). Multi-dimensional reformulations of the MR equation have appeared before [127, 126] but remained inaccessible to general mathematical analysis due to the implicit dependence of their right-hand sides on $\dot{y}$.

Our formulation turns the MR equation into a nonlinear system of fractional-order differential equations in terms of y and w. The standard techniques for the proof of existence and uniqueness of solutions of such equations assume Lipschitz continuity of the right hand side with respect to the (y, w) variable [130, 131]. This assumption fails for the MR equation (see the term $M_u(y,t)w$ in Eq. (4.7) below). Therefore, as discussed in Section §4.3, modifications to the standard function spaces, estimates and assumptions are required.

4.2 Preliminaries

We start by letting the velocity of the inertial particle be $v : \mathbb{R}^+ \to \mathbb{R}^n$, and use this notation to rewrite (4.1) as a first-order system of equations

$$\begin{aligned}
\dot{y} &= v \\
\dot{v} &= R\frac{Du}{Dt} + \left(1 - \frac{3R}{2}\right) g + \frac{R}{2}\frac{D}{Dt}\left(u + \frac{\gamma}{10}\mu^{-1}\Delta u\right) \\
&\quad - \mu\left(v - u - \frac{\gamma}{6}\mu^{-1}\Delta u\right) \\
&\quad - \kappa\mu^{1/2}\left\{\int_0^t \frac{\dot{w}(s)}{\sqrt{t-s}}\mathrm{d}s + \frac{w(0)}{\sqrt{t}}\right\},
\end{aligned} \tag{4.5}$$

with the function $w(t)$ defined as in (4.2). As earlier, the material derivative $\frac{D}{Dt} \doteq \partial_t + u \cdot \nabla$ denotes a time derivative along a fluid trajectory. Also $\frac{d}{dt} \doteq \partial_t + v \cdot \nabla$ denotes temporal differentiation along the inertial trajectory $y(t)$. The two derivatives are related by the identity

$$\frac{d}{dt} = \frac{D}{Dt} + (v - u) \cdot \nabla. \tag{4.6}$$

For notational simplicity, we will also use the dot symbol for the derivative $\frac{d}{dt}$.

In the original derivation of the MR equation [117], it is implicitly assumed that the initial velocity of the particle v_0 is such that $w(0) = 0$ holds. Equation (4.5), however, is the most general form of the MR equation which was derived later [132] and allows for a general initial particle velocity v_0.

Using the identity (4.6) and the identity

$$\frac{\mathrm{d}}{\mathrm{d}t}\int_0^t \frac{w(s)}{\sqrt{t-s}}\mathrm{d}s = \int_0^t \frac{\dot{w}(s)}{\sqrt{t-s}}\mathrm{d}s + \frac{w(0)}{\sqrt{t}}$$

for Riemann–Liouville fractional-order derivatives [131], we rewrite (4.5) in the more compact form

$$\begin{aligned}\dot{y} &= w + A_u(y,t),\\ \dot{w} &= -\mu\, w - M_u(y,t)w - \kappa\mu^{1/2}\frac{\mathrm{d}}{\mathrm{d}t}\int_0^t \frac{w(s)}{\sqrt{t-s}}\mathrm{d}s + B_u(y,t),\end{aligned} \tag{4.7}$$

where

$$\begin{aligned}A_u &= u + \frac{\gamma}{6}\mu^{-1}\Delta u,\\ B_u &= \left(\frac{3R}{2} - 1\right)\left(\frac{Du}{Dt} - g\right) + \left(\frac{R}{20} - \frac{1}{6}\right)\gamma\mu^{-1}\frac{D}{Dt}\Delta u\\ &\quad - \frac{\gamma}{6}\mu^{-1}\left[\nabla u + \frac{\gamma}{6}\mu^{-1}\nabla\Delta u\right]\Delta u,\\ M_u &= \nabla u + \frac{\gamma}{6}\mu^{-1}\nabla\Delta u,\end{aligned}$$

are known functions in terms of the fluid velocity u. The terms A_u, B_u : $\mathcal{D}\times R^+ \to \mathbb{R}^n$ represent vector fields while $M_u : \mathcal{D}\times\mathbb{R}^+ \to \mathbb{R}^{n\times n}$ is a tensor field. Note that equation (4.7) is linear in w and, for a typical fluid velocity field u, non-linear in y. The corresponding initial conditions for (4.7) are $y(0) = y_0$ and $w(0) = w_0 := v_0 - u(y_0, 0) - \frac{\gamma}{6}\mu^{-1}\Delta u(y_0, 0)$.

4.3 Local existence and uniqueness

4.3.1 Approach

This section is devoted to proving the local existence and uniqueness of solutions of (4.7) under certain smoothness assumptions on the fluid velocity field u.

Integrating equation (4.7) formally, one obtains

$$\begin{aligned}y(t) &= y_0 + \int_0^t \big[w(s) + A_u(y(s),s)\big]\mathrm{d}s,\\ w(t) &= w_0 + \int_0^t \left[-\mu\, w(s) - M_u(y(s),s)w(s) - \kappa\mu^{1/2}\frac{w(s)}{\sqrt{t-s}} + B_u(y(s),s)\right]\mathrm{d}s,\end{aligned} \tag{4.8}$$

where, for notational simplicity, we have omitted the dependence of y and w on y_0 and w_0. A *weak solution* of the MR equation is a function $(y(t), w(t))$ that satisfies the integral equation (4.8). The same solution is also a *strong solution* if it is smooth enough to also satisfy the differential form (4.7) of the MR equation.

Equation (4.8) can be viewed as a fixed point problem for the map

$$(P\Phi)(t) = \begin{pmatrix} y_0 + \int_0^t \left[\eta(s) + A_u(\xi(s), s)\right] \mathrm{d}s \\ w_0 + \int_0^t \left[-\left(\mu + \frac{\kappa\mu^{1/2}}{\sqrt{t-s}} + M_u(\xi(s), s)\right)\eta(s) + B_u(\xi(s), s)\right] \mathrm{d}s \end{pmatrix}, \tag{4.9}$$

where $\Phi = (\xi, \eta) \in \mathbb{R}^{2n}$. We will establish the existence of weak solutions to the MR equations by showing that P has a unique fixed point on an appropriate function space under general regularity assumptions on the fluid velocity u.

4.3.2 Set-up

We will use $|\cdot|$ to denote the Euclidean norm on $\mathbb{R}^m$ with $m \in \{n, 2n\}$. The induced operator norm of a square matrix acting on $\mathbb{R}^m$ is denoted by $\|\cdot\|$. For continuous functions defined on $\mathbb{R}^m$, we denote the supremum norm by $\|\cdot\|_\infty$.

Let $X_{T,K}$ denote the set of continuous functions mapping from the interval $[0, T]$ into $\mathbb{R}^m$ that are uniformly bounded by the constant $K > 0$:

$$X_{T,K} := \{f \in C([0, T]; \mathbb{R}^m) : \ \|f\|_\infty \leq K\}. \tag{4.10}$$

Since $(C([0, T]; \mathbb{R}^m), \|\cdot\|_\infty)$ is a Banach space, the space $(X_{T,K}, \|\cdot\|_\infty)$ is a complete metric space, for $X_{T,K}$ is a closed subset of $C([0, T]; \mathbb{R}^m)$.

First, we would like to show that P defined in (4.9) maps $X_{T,K}$ into itself. To this end, we need the following assumption.

(H1) The velocity field $u(x, t)$ is three times continuously differentiable in its arguments over the domain $\mathcal{D} \times \mathbb{R}^+$, and its partial derivatives (including mixed partials) are uniformly bounded and Lipschitz up to order three.

4.3.3 Existence and uniqueness of solutions

Under assumption (H1), we obtain the following result:

Lemma 4.1. *Assume that (H1) holds. Then for any $y_0 \in \mathcal{D}$ and $w_0 \in \mathbb{R}^n$, there exist $K > 0$ large enough and $\delta > 0$ small enough, such that, for any $T \in [0, \delta]$, we have P: $X_{T,K} \to X_{T,K}$.*

Proof. Under assumption (H1), the vector fields $A_u, B_u : \mathcal{D} \times \mathbb{R}^+ \to \mathbb{R}^n$ and the tensor field $M_u : \mathcal{D} \times \mathbb{R}^+ \to \mathbb{R}^{n\times n}$ are continuous and uniformly bounded. Specifically, there exists a constant $L_b > 0$ such that

$$\|A_u\|_\infty, \|B_u\|_\infty, \|M_u\|_\infty \leq L_b.$$

Then, based on eq. (4.9), the quantity $P\Phi$ satisfies the estimate

$$\begin{aligned}
|P\Phi(t)| \leq & \|y_0 + \int_0^t \left[\eta(s) + A_u(\xi(s), s)\right] \mathrm{d}s\|_\infty \\
& + \|w_0 + \int_0^t \left[\left(\mu + \frac{\kappa\mu^{1/2}}{\sqrt{t-s}} + M_u(\xi(s), s)\right)\eta(s) + B_u(\xi(s), s)\right] \mathrm{d}s\|_\infty \\
\leq & |y_0| + |w_0| + \|\eta\|_\infty \left(t + \mu t + 2\kappa\mu^{1/2}\sqrt{t} + L_b t\right) + 2L_b t \\
\leq & |y_0| + |w_0| + \|\Phi\|_\infty \left(t + \mu t + 2\kappa\mu^{1/2}\sqrt{t} + L_b t\right) + 2L_b t.
\end{aligned}$$

Now take $K = 4\max\{|y_0|, |w_0|\}$ and $\delta > 0$ small enough such that

$$\delta + \mu\delta + L_b t + 2\kappa\mu^{1/2}\sqrt{\delta} < \frac{1}{4}, \quad 2L_b\delta < \frac{K}{4}.$$

Then, for any $T \in [0, \delta]$, $\|P\Phi\|_\infty \leq K$ given that $\Phi \in X_{T,K}$. The continuity of $P\Phi : [0, T] \to \mathbb{R}^{2n}$ follows from assumption (H1) after one notes that, for $\eta \in X_{T,K}$, the term $\int_0^t \frac{\eta(s)}{\sqrt{t-s}}\mathrm{d}s$ in (4.9) is continuous in t. □

We establish the existence of a unique solution to (4.8) by proving that P is a contraction mapping on $X_{T,K}$ and hence has a unique fixed point.

Lemma 4.2. *Assume that (H1) holds. Then there exists $\delta > 0$ such that, for any $T \in [0, \delta]$ and $\Phi_1, \Phi_2 \in X_{T,K}$,*

$$\|P\Phi_1 - P\Phi_2\|_\infty \leq \frac{1}{2}\|\Phi_1 - \Phi_2\|_\infty$$

Proof. Note that as a direct consequence of assumption (H1), the maps $A_u(\cdot, t), B_u(\cdot, t) : \mathcal{D} \to \mathbb{R}^n$ and $M_u(\cdot, t) : \mathcal{D} \to \mathbb{R}^{n\times n}$ are Lipschitz continuous, uniformly in time, i.e., there is a constant $L_c > 0$ such that, for any $t \in [0, T]$ and $y_1, y_2 \in \mathcal{D}$,

$$|A_u(y_1, t) - A_u(y_2, t)| \leq L_c|y_1 - y_2|,$$

$$|B_u(y_1, t) - B_u(y_2, t)| \leq L_c|y_1 - y_2|,$$

$$\|M_u(y_1, t) - M_u(y_2, t)\| \leq L_c|y_1 - y_2|. \tag{4.11}$$

Let $\Phi_1, \Phi_2 \in X_{T,K}$, where $\Phi_i = (\xi_i, \eta_i)$. Using the above inequalities, we

have

$$
\begin{aligned}
|(P\Phi_1)(t) - (P\Phi_2)(t)| \leq & \int_0^t \left(|\eta_1(s) - \eta_2(s)| + |A_u(\xi_1(s), s) - A_u(\xi_2(s), s)|\right) \mathrm{d}s + \\
& \int_0^t \Big[\mu|\eta_1(s) - \eta_2(s)| + \kappa\mu^{1/2} \frac{|\eta_1(s) - \eta_2(s)|}{\sqrt{t-s}} + \\
& \qquad |M_u(\xi_1(s), s)\eta_1(s) - M_u(\xi_2(s), s)\eta_2(s)| + \\
& \qquad |B_u(\xi_1(s), s) - B_u(\xi_2(s), s)|\Big] \mathrm{d}s \\
\leq & (t + \mu t + 2\kappa\mu^{1/2}\sqrt{t})\|\eta_1 - \eta_2\|_\infty + 2L_c t\|\xi_1 - \xi_2\|_\infty + \\
& \int_0^t \left[|M_u(\xi_1(s), s)\eta_1(s) - M_u(\xi_1(s), s)\eta_2(s)| + \right. \\
& \qquad \left. |M_u(\xi_1(s), s)\eta_2(s) - M_u(\xi_2(s), s)\eta_2(s)|\right] \mathrm{d}s \\
\leq & (t + \mu t + 2\kappa\mu^{1/2}\sqrt{t} + L_b t)\|\eta_1 - \eta_2\|_\infty + (2 + K)L_c t\|\xi_1 - \xi_2\|_\infty,
\end{aligned}
$$

where we used the fact that

$$
\begin{aligned}
\int_0^t \Big|M_u(\xi_1(s), s)\eta_1(s) - M_u(\xi_2(s), s)\eta_2(s)\Big| \mathrm{d}s = & \\
\int_0^t \Big|M_u(\xi_1(s), s)(\eta_1(s) - \eta_2(s)) + & \left(M_u(\xi_1(s), s) - M_u(\xi_2(s), s)\right)\eta_2(s)\Big| \mathrm{d}s \\
\leq \int_0^t \|M_u(\xi_1(s), s)\||\eta_1(s) - \eta_2(s)| \mathrm{d}s + & \int_0^t \|M_u(\xi_1(s), ts) - M_u(\xi_2(s), s)\||\eta_2(s)| \mathrm{d}s \\
\leq t L_b\|\eta_1 - \eta_2\|_\infty + t L_c\|\eta_2\|_\infty\|\xi_1 - \xi_2\|_\infty. &
\end{aligned}
$$

Therefore, one can take $\delta > 0$ small enough such that, for any $t \in [0, \delta]$,

$$
\begin{aligned}
|(P\Phi_1)(t) - (P\Phi_2)(t)| \leq & \frac{1}{4}\left(\|\xi_1 - \xi_2\|_\infty + \|\eta_1 - \eta_2\|_\infty\right) \\
\leq & \frac{1}{2}\|\Phi_1 - \Phi_2\|_\infty.
\end{aligned}
$$

Here, for the last inequality, we have used the fact that $\|\xi\|_\infty + \|\eta\|_\infty < 2\|\Phi\|_\infty$. Hence, we obtain the contraction property

$$
\|P\Phi_1 - P\Phi_2\|_\infty \leq \frac{1}{2}\|\Phi_1 - \Phi_2\|_\infty,
$$

as claimed. □

Lemma 4.2 leads to our main existence result.

Theorem 4.1. *[Local existence of weak solutions] Assume that (H1) holds. Then for any initial condition $(y_0, w_0) \in \mathcal{D} \times \mathbb{R}^n$, there exists $\delta > 0$ such that over the time interval $[0, \delta]$, the integral equation (4.8) has a unique solution $(y(t), w(t))$ with $(y(0), w(0)) = (y_0, w_0)$. As consequence, the function $y(t)$ is a weak solution of the original form (4.1) of the Maxey–Riley equation.*

Proof. By Lemma 4.2, for any $y_0 \in \mathcal{D}$ and $w_0 \in \mathbb{R}^n$, there exist $K > 0$ and $\delta > 0$ such that for any $T \in [0, \delta]$, the map $P : X_{T,K} \to X_{T,K}$ is a contraction on the complete metric space $X_{T,K}$. As a consequence, the mapping P has a unique fixed point $(y, w) : [0, \delta] \to \mathcal{D}\times\mathbb{R}^n$. By the definition of P, this fixed point solves the integral equation (4.8), and hence is a weak solution of (4.7), or equivalently, of (4.1). □

Remark 4.1. The solution $y(t)$ is, in general, not a strong solution of (4.1), because it is only once continuously differentiable at $t = 0$, and hence only satisfies the integrated form of $w(t)$. The following example demonstrates the lack of existence of strong solutions in a simple case where the w-equation in (4.7) can be solved explicitly.

Example 4.1. For a uniform fluid at rest (i.e., $u \equiv 0$), if we neglect the effect of gravity (i.e., set $g = 0$), A_u, B_u and M_u in equation (4.7) vanish. Then, the equation for w reduces to

$$\dot{w} + \kappa\mu^{1/2}\frac{\mathrm{d}}{\mathrm{d}t}\int_0^t \frac{w(s)}{\sqrt{t-s}}\mathrm{d}s + \mu w = 0,$$

with an arbitrary initial condition $w(0) = w_0$. Taking the Laplace transform of this equation, we obtain

$$W(p) = \frac{1}{p + Gp^{1/2} + \mu}w_0,$$

where $G = \sqrt{9R\mu/2}$ and W denotes the Laplace transform of w. For $R < 8/9$, the inverse Laplace transform yields the exact solution

$$w(t) = w_0\Big\{\mathrm{e}^{-\alpha t}\cos(\beta t) + \frac{G^2}{2\beta}\mathrm{e}^{-\alpha t}\sin(\beta t) - \frac{G}{\sqrt{\pi}}\int_0^t \frac{\mathrm{e}^{-\alpha s}\cos(\beta s) - (\alpha/\beta)\mathrm{e}^{-\alpha s}\sin(\beta s)}{\sqrt{t-s}}\mathrm{d}s\Big\},$$

with $\alpha = \mu(1 - 9R/4)$ and $\beta = G\sqrt{\mu(1 - 9R/8)}$. Defining

$$c(s) = \mathrm{e}^{-\alpha s}\cos(\beta s) - (\alpha/\beta)\mathrm{e}^{-\alpha s}\sin(\beta s),$$

and taking the derivative of w with respect to time t, we obtain

$$\dot{w}(t) = w_0\Big\{\left(\frac{G^2}{2} - \alpha\right)\mathrm{e}^{-\alpha t}\cos(\beta t) - \left(\frac{\alpha G^2}{2\beta} + \beta\right)\mathrm{e}^{-\alpha t}\sin(\beta t) - \frac{G}{\sqrt{\pi}}\int_0^t \frac{\dot{c}(s)}{\sqrt{t-s}}\mathrm{d}s - \frac{G}{\sqrt{\pi t}}\Big\}.$$

For any $T > 0$, the first three terms in $\dot{w}$ are continuous over the time interval $[0, T]$. The last term $\frac{G}{\sqrt{\pi t}}$, however, is discontinuous at $t = 0$. This concludes our example showing that, in general, the MR equation with non-zero initial condition $w(0)$ only admits weak solutions. ■

As mentioned in the Introduction, the original form of the MR equation [117] assumes the initial velocity $w(0) = 0$. This assumption is mathematically convenient, as it removes the unbounded term from (4.1). Physically, however,

the assumption is artificial, and cannot be enforced at the release of an inertial particle.

Nevertheless, $w(0) = 0$ has been routinely assumed in various studies of the MR equation (see, e.g., Babiano et al. [122], Candelier et al. [124], Daitche and Tél [125]) as an important special case. We now show that under this special assumption, the MR equation in fact has strong solutions.

Theorem 4.2. *Assume that (H1) holds. Then for any $y_0 \in \mathcal{D}$, there exists $\delta > 0$ such that, over the time interval $[0, \delta]$, the Maxey-Riley equation (4.1) has a unique solution satisfying $y(0) = y_0$ and $w(0) = 0$.*

Proof. See Appendix 4.A. □

4.3.4 Regularity of solutions

Here we show the differentiability of the solutions of (4.7) with respect to the initial condition (y_0, w_0). Assume that a solution $(y(t), w(t))$ is differentiable at (y_0, w_0) and denote the derivative of y and w with respect to (y_0, w_0) by Dy and Dw, respectively.

Differentiating (4.7) formally and integrating in time, we obtain that $Dy, Dw : \mathbb{R}^+ \to \mathbb{R}^{n\times 2n}$ must satisfy

$$\begin{aligned} Dy(t) =& \big(I_n | O_n\big) + \int_0^t \left[Dw(s) + \nabla A_u(y(s), s) Dy(s)\right] \mathrm{d}s, \\ Dw(t) =& \big(O_n | I_n\big) + \int_0^t \Big[-\mu Dw(s) - \mathcal{L}(y(s), w(s), s) Dy(s) - M_u(y(s), s) Dw(s) \\ & - \kappa\mu^{1/2} \frac{Dw(s)}{\sqrt{t-s}} + \nabla B_u(y(s), s) Dy(s)\Big] \mathrm{d}s, \end{aligned} \tag{4.12}$$

where $\mathcal{L}$ denotes the $n \times n$ matrix given by

$$\mathcal{L}_{ij}(y(s), w(s), s) = \sum_k \frac{\partial M_{ik}}{\partial y_j}\Big|_{(y(s),s)} w_k(s).$$

The matrices I_n and O_n denote the identity and null matrices on $\mathbb{R}^{n\times n}$.

The differentiability of the solution (y, w) with respect to the initial condition (y_0, w_0), therefore, is equivalent to the existence and uniqueness of solutions to the equations (4.12). We show that under further regularity assumptions on the fluid velocity u, a unique solution to these equations does exist. In particular, we need the following assumption:

(H2) The velocity field $u(x, t)$ is four times continuously differentiable in its arguments over the domain $\mathcal{D} \times \mathbb{R}^+$. Its partial derivatives (including mixed partials) are uniformly bounded and Lipschitz up to order three.

Theorem 4.3. *Assume that (H2) holds. Then for any $y_0 \in \mathcal{D}$ and $w_0 \in \mathbb{R}^n$, there exists $\delta > 0$ small enough such that, a unique weak solution $(y(t), w(t))$ of (4.7) exists over the time interval $[0, \delta]$, and is continuously differentiable with respect to its initial condition (y_0, w_0).*

Proof. Note that the map $\mathcal{P}$ defined by the right hand side of (4.12) is linear in Dy and Dw. It follows from assumption (H2) that $\mathcal{P}$ maps $C([0,\delta];\mathbb{R}^{2n\times 2n})$ into itself for any $\delta \in \mathbb{R}^+$. Furthermore, for $\delta > 0$ small enough, the map $\mathcal{P}$ is a contraction $C([0,\delta];\mathbb{R}^{2n\times 2n})$ by an argument similar to Lemma (4.2) (omitted here for brevity). Therefore, there are unique derivatives $Dy, Dw : [0,\delta] \to \mathbb{R}^{n\times 2n}$ that belong to the function space $C([0,\delta];\mathbb{R}^{n\times 2n})$ and solve equations (4.12). □

Remark 4.2. For the special case $w(0) = 0$, one can similarly show that the strong solution $(y(t), w(t))$ is differentiable with respect to the initial position y_0.

4.4 Conclusion

We have proved the local existence and uniqueness of solutions of the Maxey–Riley (MR) equation. In the most general case, the solutions exist only in a weak sense. This is consistent with the physics of the problem, because an initial velocity mismatch between the ambient fluid and the particle creates a vorticity layer around the particle with high drag. This drag force is modeled in the MR equation by a term proportional to $1/\sqrt{t}$, which is singular but integrable. As a result, the solution of the MR equation is continuous but only differentiable for $t > 0$.

In theoretical and numerical investigations of the MR equation, it is routinely assumed that the relative velocity term $w(t)$ is chosen in a way that eliminates the infinitely large force at time $t = 0$. We have shown that under this assumption, a unique strong solution exists to the MR equation. Moreover, both the weak and the strong solutions are differentiable with respect to their initial conditions.

Remaining challenges for the MR equations include global existence and uniqueness and an asymptotic analysis of the solutions, at least for small inertial particles.

Appendix 4.A Proof of Theorem 4.2

First, we slightly reformulate the MR equation. If continuously differentiable solutions to equation (4.7) exist, then the integral term in the equation can be re-written as

$$\frac{\mathrm{d}}{\mathrm{d}t}\int_0^t \frac{w(s)}{\sqrt{t-s}}\mathrm{d}s = \int_0^t \frac{\dot{w}(s)}{\sqrt{t-s}}\mathrm{d}s,$$

since $w(0) = 0$. As a consequence, the MR equation (4.7) can be written as

$$\begin{aligned}\dot{y} &= w + A_u(y,t),\\ \dot{w} &= -\mu\, w - M_u(y,t)w - \kappa\mu^{1/2}\int_0^t \frac{\dot{w}(s)}{\sqrt{t-s}}\mathrm{d}s + B_u(y,t).\end{aligned} \tag{4.13}$$

Now, we would like to show that this latter equation, in fact, admits continuously differentiable solutions satisfying $y(0) = y_0$ and and $w(0) = 0$. Our proof will differ from the proof of Theorem 4.1. The main ideas follow those of Burton and Purnaras [129], although the details are quite different. In particular, the results of [129] do not apply in our context.

We need to show that there are unique bounded continuous functions $\phi, \psi : [0, T] \to \mathbb{R}^n$ such that the functions

$$y(t) = y_0 + \int_0^t \phi(s)\mathrm{d}s,$$

$$w(t) = \int_0^t \psi(s)\mathrm{d}s, \tag{4.14}$$

solve equation (4.13). For notational simplicity, we omit the dependence of y, w, ϕ and ψ on the initial condition y_0.

Substituting $y(t)$ and $w(t)$ in (4.13), we obtain

$$\begin{aligned}
\phi(t) = & \int_0^t \psi(s)\mathrm{d}s + A_u\left(y_0 + \int_0^t \phi(s)\mathrm{d}s, t\right), \\
\psi(t) = & -\mu \int_0^t \psi(s)\mathrm{d}s - M_u\left(y_0 + \int_0^t \phi(s)\mathrm{d}s, t\right) \int_0^t \psi(s)\mathrm{d}s \\
& - \kappa\mu^{1/2} \int_0^t \frac{\psi(s)}{\sqrt{t-s}}\mathrm{d}s + B_u\left(y_0 + \int_0^t \phi(s)\mathrm{d}s, t\right).
\end{aligned} \tag{4.15}$$

The right-hand sides of these equations define a mapping P as

$$(P\Phi)(t) = \begin{pmatrix} \int_0^t \psi(s)\mathrm{d}s + A_u(y(t), t) \\ -\int_0^t \left[\mu + \frac{\kappa\mu^{1/2}}{\sqrt{t-s}} + M_u(y(t), t)\right] \psi(s)\mathrm{d}s + B_u(y(t), t) \end{pmatrix}, \tag{4.16}$$

where $\Phi = (\phi, \psi) \in \mathbb{R}^{2n}$ and $y(t) = y_0 + \int_0^t \phi(s)\mathrm{d}s$.

We will show that the mapping P has a unique fixed point in $X_{T,K}$ for some $T, K > 0$. Then the existence of the above mentioned solution of (4.13) follows directly.

The following lemma shows that for an appropriate choice of T and K, P maps $X_{T,K}$ into itself.

Lemma 4.3. *Assume that (H1) holds. Then for $K \geq 4L_b$ and any $y_0 \in \mathcal{D}$, there exists $\delta > 0$ such that, for any $T \in [0, \delta]$, we have $P : X_{T,K} \to X_{T,K}$.*

Proof. The continuity of $P\Phi : \mathbb{R}^+ \to \mathbb{R}^{2n}$ follows from assumption (H1). We

also have

$$\begin{aligned}
|P\Phi(t)| \leq & \| \int_0^t \psi(s)\mathrm{d}s + A_u(y(t),t)\|_\infty \\
& + \| - \int_0^t \left[\mu + \frac{\kappa\mu^{1/2}}{\sqrt{t-s}} + M_u(y(t),t)\right]\psi(s)\mathrm{d}s + B_u(y(t),t)\|_\infty \\
\leq & \|\psi\|_\infty \left(t + \mu t + 2\kappa\mu^{1/2}\sqrt{t} + L_b t\right) + 2L_b \\
\leq & \|\Phi\|_\infty \left(t + \mu t + 2\kappa\mu^{1/2}\sqrt{t} + L_b t\right) + 2L_b \\
\leq & K\left(t + \mu t + 2\kappa\mu^{1/2}\sqrt{t} + L_b t\right) + \frac{K}{2}
\end{aligned}$$

If $\delta > 0$ is small enough such that $t+\mu t+2\kappa\mu^{1/2}\sqrt{t}+L_b t \leq 1/2$ for any $t \in [0,\delta]$, we have $\|P\Phi\|_\infty \leq K$; and hence $P\Phi \in X_{T,K}$ for any $T \in [0,\delta]$. □

We now fix the constant $K = 4L_b$ in the following. We show that the map P is a contraction mapping on the space $X_{T,K}$.

Lemma 4.4. *There is $\delta > 0$ such that, for any $T \in [0,\delta]$ and $\Phi_1, \Phi_2 \in X_{T,K}$,*

$$\|P\Phi_1 - P\Phi_2\|_\infty \leq \frac{1}{2}\|\Phi_1 - \Phi_2\|_\infty$$

Proof. Let $\Phi_1, \Phi_2 \in X_{T,K}$ where $\Phi_i = (\phi_i, \psi_i)^\top$. We have

$$\begin{aligned}
|(P\Phi_1)(t) - (P\Phi_2)(t)| \leq & \int_0^t |\psi_1(s) - \psi_2(s)|\mathrm{d}s + |A_u(y_1(t),t) - A_u(y_2(t),t)| \\
& + \mu\int_0^t |\psi_1(s) - \psi_2(s)|\mathrm{d}s \\
& + \kappa\mu^{1/2}\int_0^t \frac{|\psi_1(s) - \psi_2(s)|}{\sqrt{t-s}}\mathrm{d}s \\
& + |M_u(y_1(t),t)\int_0^t \psi_1(s)\mathrm{d}s - M_u(y_2(t),t)\int_0^t \psi_2(s)\mathrm{d}s| \\
& + |B_u(y_1(t),t) - B_u(y_2(t),t)| \\
\leq & \int_0^t |\psi_1(s) - \psi_2(s)|\mathrm{d}s + L_c\int_0^t |\phi_1(s) - \phi_2(s)|\mathrm{d}s \\
& + \mu\int_0^t |\psi_1(s) - \psi_2(s)|\mathrm{d}s \\
& + \kappa\mu^{1/2}\int_0^t \frac{|\psi_1(s) - \psi_2(s)|}{\sqrt{t-s}}\mathrm{d}s \\
& + L_b\int_0^t |\psi_1(s) - \psi_2(s)|\mathrm{d}s
\end{aligned}$$

$$+ L_c(t\|\psi_2\|_\infty) \int_0^t |\phi_1(s) - \phi_2(s)|\mathrm{d}s$$
$$+ L_c \int_0^t |\phi_1(s) - \phi_2(s)|\mathrm{d}s,$$

where we have used the Lipschitz continuity of $A_u(\cdot, t)$, $B_u(\cdot, t)$ and $M_u(\cdot, t)$. We also used the fact that

$$\begin{aligned}\left|M_u(y_1,t)\int_0^t \psi_1(s)\mathrm{d}s - M_u(y_2,t)\int_0^t \psi_2(s)\mathrm{d}s\right| = \\ \left|M_u(y_1,t)\int_0^t (\psi_1(s)-\psi_2(s))\mathrm{d}s + (M_u(y_1,t)-M_u(y_2,t))\int_0^t \psi_2(s)\mathrm{d}s\right| \\ \leq \|M_u(y_1,t)\|\int_0^t |\psi_1(s)-\psi_2(s)|\mathrm{d}s + \|M_u(y_1,t)-M_u(y_2,t)\|\int_0^t |\psi_2(s)|\mathrm{d}s.\end{aligned}$$

As a result, we obtain

$$\begin{aligned}|(P\Phi_1)(t) - (P\Phi_2)(t)| \leq &\Big(t + \mu t + 2\kappa\mu^{1/2}\sqrt{t} + L_b t\Big)\|\psi_1 - \psi_2\|_\infty \\ &+ \Big(2L_c t + L_c K t^2\Big)\|\phi_1 - \phi_2\|_\infty.\end{aligned}$$

Therefore, one can take $\delta > 0$ small enough such that, for any $t \in [0, \delta]$,

$$\begin{aligned}|(P\Phi_1)(t) - (P\Phi_2)(t)| \leq &\frac{1}{4}\left(\|\phi_1 - \phi_2\|_\infty + \|\psi_1 - \psi_2\|_\infty\right) \\ \leq &\frac{1}{2}\|\Phi_1 - \Phi_2\|_\infty.\end{aligned}$$

Hence we get the contraction property

$$\|P\Phi_1 - P\Phi_2\|_\infty \leq \frac{1}{2}\|\Phi_1 - \Phi_2\|_\infty.$$

□

Since P is a contraction mapping on the complete metric space $X_{T,K}$, it has a unique fixed point in $X_{T,K}$. Therefore, there are unique continuous functions $\phi, \psi : [0, \delta] \to \mathbb{R}^n$ such that the functions y, w defined by (4.14) solve the MR equation (4.13) and satisfy $y(0) = y_0$ and $w(0) = 0$. This concludes the proof of Theorem 4.2.

Part II

Applications

Chapter 5

How coherent are the vortices of two-dimensional turbulence?

5.1 Introduction

Coherent vortices are persistent patches of rotating fluid that are observed in experimentally and numerically generated two-dimensional turbulence [55, 134–136]. As opposed to a typical closed material line, the boundary of a coherent vortex is envisioned to preserve its overall shape without substantial stretching, folding or filamentation. While intuitive and simple, this material view on vortices is surprisingly challenging to formulate in rigorous and computable mathematical terms [137, 112].

For the detection of coherent vortices, the most natural quantity to consider is vorticity itself, which is almost invariant along fluid trajectories in high-Reynolds-number two-dimensional turbulence. Vorticity, however, can drastically differ in coordinate frames rotating relative to each other, resulting in conflicting vortex detections in different frames. Moreover, there are no well-justified thresholds over which a vortex contour could be considered coherent.

To circumvent the shortcomings of the vorticity field, a number of Eulerian scalar quantities have been developed for vortex detection (see [138] and [139], for a review). These methods attempt to quantify the rotation of fluid elements against the strain they experience. Simply connected regions with dominant rate of rotation are then defined as vortices. For instance, the Okubo-Weiss (OW) criterion [140, 141] measures the difference between the instantaneous rates of rotation and strain assuming that these quantities evolve slowly in time. Later, Hua and Klein [142] accounted for rapid changes in strain and rotation by including higher-order terms, i.e., acceleration terms.

In addition to their lack of objectivity, these Eulerian indicators are not ideal

for coherent vortex detection because, unlike vorticity, they are not preserved along fluid trajectories. As a result, the detected vortex boundaries at different time instances do not evolve into each other when advected under the flow. This invariance under the flow map is desirable since our intuitive understanding of a coherent vortex as a rotating body of fluid is Lagrangian in nature.

A recent development in the theory of finite-time dynamical systems [24] offers an objective Lagrangian measure of coherence that can be applied to coherent vortices of two-dimensional turbulence. Haller and Beron-Vera [24] show that an appropriately defined Lagrangian strain energy necessarily vanishes along coherent (i.e., non-filamenting) material lines. They develop a numerical method based on this principle to find closed coherent material lines in two-dimensional flows, and apply it to satellite-derived surface velocities in the ocean.

Here, we use their method to detect the optimal boundaries of coherent vortices in a direct numerical simulation of Navier-Stokes turbulence. We also carry out a detailed comparison with alternative Eulerian and Lagrangian techniques. This comparison reveals that the coherent vortices that survive for long times are significantly larger than what has been thought so far.

In section §5.2, we use Lagrangian vortex detection method of [24] to locate vortices objectively in a direct numerical simulation of Navier–Stokes turbulence. We verify that the coherent vortex boundaries obtained in this fashion are indeed optimal. With these optimal boundaries at hand, we find that coherent vortices are significantly larger in enclosed surface area but also smaller in number than previously thought.

In Section §5.2, we briefly review the variational theory of [24]. Our results are presented in Section §6.3. Section §5.4 contains our concluding remarks.

5.2 Preliminaries

5.2.1 Set-up

Let $u(x,t)$ be a two-dimensional velocity field, defined over positions x in an open domain $U \subset \mathbb{R}^2$ and times t ranging though a finite interval $I = [a,b]$. The motion of passive fluid particles under such a velocity field is governed by the differential equation

$$\dot{x} = u(x,t), \tag{5.1}$$

where $x(t;t_0,x_0)$ is the position of a particle at time t whose initial position at time t_0 is $x_0 \in U$. For the fixed time interval I, the dynamical system (6.1) defines the specific flow map

$$\begin{aligned} F : U &\to U \\ x_a &\mapsto x_b, \end{aligned} \tag{5.2}$$

that takes an initial condition x_a to its time-b position $x_b = F(x_a) := x(b;a,x_a)$.

5.2.2 Coherence principle

A typical set of fluid particles deforms significantly as advected under the flow map F, provided that the advection time $b-a$ is at least of the order of a few eddy turn-over times in a turbulent flow [8]. One may seek coherent material vortices as atypical sets of fluid trajectories that defy this trend by preserving their overall shape. These shapes are necessarily bounded by closed material lines that rotate and translate, but otherwise show no appreciable stretching or folding.

Haller and Beron-Vera [24] seek Lagrangian vortex boundaries as closed material lines exhibiting no leading order average straining. A thin material belt around a typical material line γ experiences visible straining as advected under the flow. The material belt around a coherent material line, however, does not exhibit any noticeable strain (see figure 5.1).

To formulate this mathematically, let γ be a closed material line over the time interval $[a,b]$ and let $r : s \mapsto r(s)$ be a parametrization of γ at the initial time $t = a$. The *averaged tangential strain* of this material line over the time interval $I = [a,b]$ is then given by

$$Q(\gamma) = \frac{1}{\sigma}\int_0^\sigma \frac{\sqrt{\langle r'(s), C(r(s))r'(s)\rangle}}{\sqrt{\langle r'(s), r'(s)\rangle}}\mathrm{d}s, \tag{5.3}$$

where $s \in [0,\sigma]$. The Cauchy–Green strain tensor $C = DF^\top DF$ is defined in terms of the Jacobian of the flow map DF with the symbol $\top$ denoting matrix transposition [143]. The *prime* denotes the derivative with respect to the arc-length s and $\langle\cdot,\cdot\rangle$ denotes the Euclidean inner product.

Consider a small perturbation to γ given by $\gamma + \epsilon h$ where $0 < \epsilon \ll 1$ and $h : [0,\sigma] \to \mathbb{R}^2$ is a σ-periodic $\mathcal{O}(1)$ vector field orthogonal to γ. The perturbation $\gamma + \epsilon h$ represents the thin material belt of figure 5.1. For a typical material line, we have $Q(\gamma + \epsilon h) = Q(\gamma) + \mathcal{O}(\epsilon)$ due to the smoothness of the flow map F. That is $\mathcal{O}(\epsilon)$-perturbations to the material line γ lead to a $\mathcal{O}(\epsilon)$-perturbation in the averaged tangential strain Q. [24] argue that for a thin material belt centered on γ to remain coherent, it should not exhibit a leading-order change in its averaged straining. The leading order is meant with respect to the width of the material belt. In other words, $Q(\gamma + \epsilon h) = Q(\gamma) + \mathcal{O}(\epsilon^2)$ for a coherent material line γ, that is the first variation of Q vanishes: $\delta Q(\gamma) = 0$.

The Euler-Lagrange equations arising from the condition $\delta Q(\gamma) = 0$ are too complicated to yield any insight. [24] show, however, that a material line satisfies $\delta Q(\gamma) = 0$ if and only if it satisfies the pointwise condition

$$\langle r'(s), E_\lambda(r(s))r'(s)\rangle = 0, \tag{5.4}$$

for some constant $\lambda > 0$. The generalized *Green–Lagrange strain tensor* E_λ in (5.4) is defined in terms of the *Cauchy–Green strain tensor* C as

$$E_\lambda = \frac{1}{2}[C - \lambda^2 I], \tag{5.5}$$

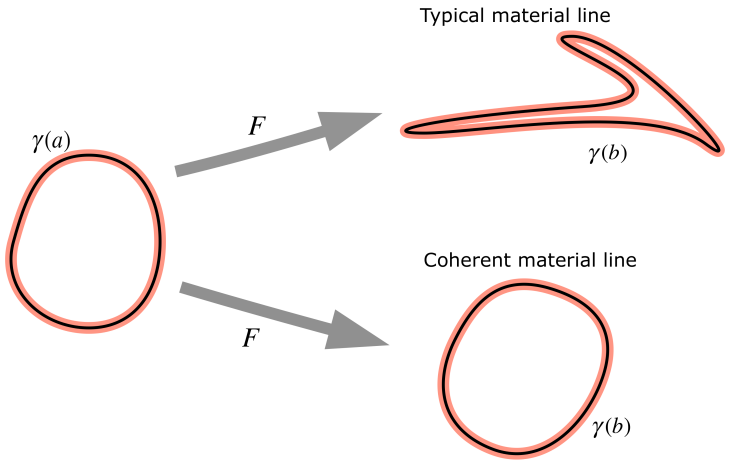

Figure 5.1: Deformation of a typical material line γ versus a coherent material line as advected under the flow map F from time $t = a$ to $t = b$. No leading-order straining is observed in the material belt (red) around a coherent material line.

where I is the two-by-two identity matrix.

Solving the implicit differential equation (5.4) simplifies locating coherent material lines as it has the explicit solutions

$$r' = \eta_\lambda^\pm(r) := \sqrt{\frac{\lambda_2(r) - \lambda^2}{\lambda_2(r) - \lambda_1(r)}}\xi_1(r) \pm \sqrt{\frac{\lambda^2 - \lambda_1(r)}{\lambda_2(r) - \lambda_1(r)}}\xi_2(r), \tag{5.6}$$

in terms of the invariants of the Cauchy–Green strain tensor C: $0 < \lambda_1 \leq \lambda_2$ are eigenvalues of C and $\{\xi_1, \xi_2\}$ are their corresponding eigenvectors. In an incompressible flow, $\lambda_1\lambda_2 = 1$ [47].

The vectors η_λ^+ and η_λ^- are one-parameter families of vector fields with λ being the parameter. In an incompressible flow, we have $\lambda_2 \geq 1$ and $\lambda_1 \leq 1$. Therefore, for $\lambda = 1$, $\eta_\lambda^\pm$ are well-defined real vector fields over the entire physical domain U. For $\lambda \neq 1$, the vector fields $\eta_\lambda^\pm$ are only defined over a subset $U_\lambda \subset U$ where $\lambda_2 \geq \lambda^2$ and $\lambda_1 \leq \lambda^2$. The trajectories of $\eta_\lambda^\pm$ can be computed over U_λ. We refer to these trajectories as λ-stretching material lines (or λ-*lines*, for short)

5.2.3 Lagrangian vortex boundaries and λ-lines

Here, we discuss some properties of the λ-lines that are of relevance for the Lagrangian coherent vortex detection in two-dimensional turbulence.

(i) *Uniform stretching*: λ-lines stretch uniformly by a factor of λ as advected under the flow map F. To quantify this statement, let γ_a be time-a position of a λ-line parametrized by $r : s \mapsto r(s)$. Since γ_a is a λ-line, we have $r'(s) \parallel \eta_\lambda^\pm(r(s))$. Its time-$b$ position γ_b will be parametrized by $F \circ r : s \mapsto F(r(s))$

whose tangential vector is given by $DF(r(s))r'(s)$. It is readily verifiable that $|DF(r(s))r'(s)| = \lambda|r'(s)|$. That is each material element of γ_a stretches by a factor of λ as advected by the flow to time $t = b$. Consequently, the total length of the curve changes by a factor of λ, i.e. $\ell(\gamma_b) = \lambda\ell(\gamma_a)$, where ℓ is the length of the curve.

For $\lambda = 1$, this implies that the final length $\ell(\gamma_b)$ is equal to the initial length $\ell(\gamma_a)$ and therefore the material line is, in fact, *non-stretching*. This is an atypical behavior for a material line in a turbulent flow, as a typical material line will stretch (or shrink) significantly under advection. This, however, does *not* imply unlikelihood of the existence of non-stretching material lines. In fact, through any point in the domain U there are two such material lines computable as the solution curves of η_1^+ and η_1^-.

For $\lambda \neq 1$, a similar statement holds for the subset $U_\lambda \subset U$: Passing through any point in U_λ are two uniformly stretching material lines that stretch by a factor λ.

(ii) *Existence of closed λ-lines*: Although λ-lines fill the set U_λ densely, they tend to be typically open. In general, the existence of closed λ-lines depends on the dynamical system. As shown in section §6.3, closed λ-lines exist in two-dimensional turbulent flows and mark the boundaries of coherent vortices. In fact, closed λ-lines always appear as a nested family of curves corresponding to different λ values close to 1 [24].

(iii) *Relation to Lagrangian vortex boundaries*: Why should one expect the Lagrangian vortex boundaries to be marked by closed λ-lines? In an incompressible flow, the area enclosed by any closed curve is invariant under the flow map [47]. Closed λ-lines with $\lambda = 1$, in addition, preserve their arc-length. As a consequence of this dual invariance of enclosed area and arc-length, closed λ-lines cannot deform significantly as advected under the flow map F. This property is the hallmark of coherent vortex boundaries in two-dimensional turbulence.

(iv) *Relation to KAM tori*: In time-periodically perturbed two-dimensional Hamiltonian systems, Kolmogorov-Arnold-Moser (KAM) curves are material lines that return onto themselves after some time-period of the perturbation [6]. As a result, KAM curves encircle regions with coherent dynamics, usually referred to as elliptic regions. In a temporally aperiodic system, however, material lines are generally not expected to come back on themselves at any time instance. Yet, elliptic regions with coherent dynamics are known to exist even in complex, aperiodic dynamical systems such as two-dimensional turbulence. Closed λ-lines are, in this sense, the generalization of the KAM curves to aperiodic flows. In the periodic case, it has been shown that KAM curves coincide with closed λ-lines [23, 53].

In light of the above discussion, we will seek Lagrangian coherent vortex boundaries as closed λ-lines. We refer to closed λ-lines as *elliptic Lagrangian coherent structures* (or elliptic LCSs, for short). In the case $\lambda = 1$, they are referred to as *primary* elliptic LCSs.

5.2.4 Black-hole analogy

As pointed out in [24], elliptic LCSs are analogous to black holes in cosmology. Over the subset U_λ of the flow domain, the bilinear form $g_\lambda : \mathbb{R}^2 \times \mathbb{R}^2 \to \mathbb{R}$ given by

$$g_\lambda(v, w) = \langle v, E_\lambda w \rangle,$$

defines a Lorentzian metric with signature $(-, +)$. (U_λ, g_λ) is a two-dimensional Lorentzian manifold. This manifold is similar to the space-time continuum in general relativity. In that context the manifold (U_λ, g_λ) is referred to as a two-dimensional space-time. Note that as opposed to Euclidean geometry, the distance between two distinct points measured by a Lorentzian metric can be negative or zero.

In the space-time geometry, light travels along null-geodesics of the metric g_λ which coincide with the λ-lines defined above. Near a black hole, the gravity is strong enough to trap the light on a closed orbit called a *photon sphere* [144]. Therefore, elliptic LCSs and hence Lagrangian vortex boundaries are the fluid analogs of photon spheres.

5.3 Results and discussion

We will use the method described in section §5.2 to identify coherent Lagrangian vortices in a direct numerical simulation of two-dimensional forced turbulence.

5.3.1 Numerical method

Consider the Navier–Stokes equations

$$\partial_t u + u \cdot \nabla u = -\nabla p + \nu \Delta u + f, \tag{5.7a}$$

$$\nabla \cdot u = 0, \tag{5.7b}$$

$$u(x, 0) = u_0(x), \tag{5.7c}$$

where the velocity field $u(x, t)$ is defined on the two-dimensional domain $U = [0, 2\pi] \times [0, 2\pi]$ with doubly periodic boundary conditions.

We use a standard pseudo-spectral method with 512 modes in each direction and 2/3 dealiasing to solve the above Navier–Stokes equation with viscosity $\nu = 10^{-5}$. The time integration is carried out over the interval $t \in [0, 50]$ (approximately, three eddy-turn-over times) by a fourth-order Runge-Kutta method with variable step-size [145]. The initial condition u_0 is the velocity field of a decaying turbulent flow. The external force f is random in phase and band-limited, acting on the wave-numbers $3.5 < k < 4.5$. The forcing amplitude is time-dependent balancing the instantaneous enstrophy dissipation $\nu \int k^2 Z(k, t)\, \mathrm{d}k$ where $Z(k, t) := \frac{1}{2} \int_{|\mathbf{k}|=k} |\hat{\omega}(\mathbf{k}, t)|^2 \, \mathrm{d}S(\mathbf{k})$ with $\hat{\omega}(\cdot, t)$ being the Fourier transform of the instantaneous vorticity $\omega(\cdot, t) = \nabla \times u(\cdot, t)$.

In two dimensions, the energy injected into the system by the forcing is mostly transferred to larger scales through a nonlinear process [146, 147]. In order to prevent the energy accumulation at largest available scales over time, a linear damping is usually added to the Navier–Stokes equation to dissipate the energy at large scales [148, 149]. However, for the time scales considered here, the energy accumulation is not an issue and hence the linear damping will be omitted.

The theory reviewed in Section §5.2 does not assume a particular governing equation for the velocity field $u(x,t)$. Thus, it can be applied to any two-dimensional velocity field, given as numerical solution of a partial differential equation or by direct measurements. In particular, it can be applied to Lagrangian vortex detection for the solutions of the Navier–Stokes equation (5.7). To detect the Lagrangian vortex boundaries, we take the following steps:

1. Solve the Navier–Stokes equation (5.7) as discussed above to get the velocity field $u(x,t)$ over the time interval $t \in [0,50]$ and a uniform 512×512 spatial grid over the domain $x \in U = [0,2\pi] \times [0,2\pi]$. The temporal resolution of the velocity field is 251 such that two consecutive time slices are $\Delta t = 0.2$ apart.

2. Advect each grid point according to the differential equation (6.1) from time $t = 0$ to time $t = 50$ to construct the flow map F such that $F(x_a) = x_b$ for any grid point x_a.

3. Construct an approximation of the flow map gradient DF by finite differences. To increase the finite difference accuracy, we use the auxiliary grid method introduced in [48]. The chosen auxiliary grid distance is 10^{-3}.

4. Construct the Cauchy–Green strain tensor $C(x_a) = [DF(x_a)]^\top DF(x_a)$ for each grid point x_a. Compute the eigenvalues $\{\lambda_1, \lambda_2\}$ and the corresponding eigenvectors $\{\xi_1, \xi_2\}$ of the Cauchy–Green strain tensor.

5. Seek the closed orbits of the one-parameter families of vector fields $\eta_\lambda^\pm$ defined in (5.6). For detecting these closed orbits, we use the automated algorithm developed in [24].

We detect the Lagrangian vortex boundaries as elliptic LCSs, i.e., the closed orbits of $\eta_\lambda^\pm$. In the following, we present a detailed analysis of these vortex boundaries and their relation to alternative Eulerian and Lagrangian indicators.

5.3.2 Lagrangian coherent vortex analysis

Figure 5.2a shows the boundaries (red) of Lagrangian coherent vortices superimposed on the contours of the Eulerian vorticity (gray) at time $t = 0$. The boundaries are found as the outermost elliptic LCSs, i.e., closed orbits of the vector fields $\eta_\lambda^\pm$ (see Eq. (5.6)). The advected image of the coherent vortex

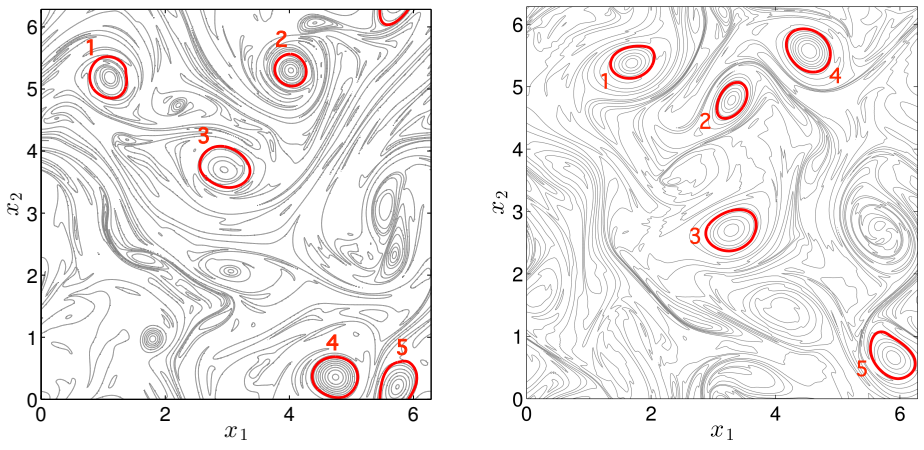

Figure 5.2: Lagrangian vortex boundaries (red) at time $t = 0$ (a) and $t = 50$ (b). The vorticity contours are shown in gray in the background. The vorticity contours are distributed as $-1 : 0.1 : 1$ at time $t = 0$ and as $-1.5 : 0.15 : 1.3$ at time $t = 50$. The coherent vortices are numbered in order to facilitate their identification at the two time-instances.

boundaries at time $t = 50$ are shown in figure 5.2b along with the corresponding instantaneous vorticity field. These coherent vortex boundaries resist straining and filamentation as advected under the flow. In the following, the vortex numbers refer to the numbering in figure 5.2.

Figure 5.3 shows the relative stretching $\delta\ell(t) := (\ell(t) - \ell(a))/\ell(a)$ of the primary elliptic LCSs over the time interval $t \in [0, 50]$. Here, $\ell(t)$ denotes the length of a material line at time t. In principle, the initial and the final lengths of a primary elliptic LCS must be exactly equal resulting in zero relative stretching at time $t = 50$. In practice, a deviation of at most 4% is observed from this ideal limit which arises from numerical errors. The inset of figure 5.3 shows the relative stretching of a typical non-coherent iso-vorticity line. Unlike the coherent vortices, the relative stretching for a general material curve increases exponentially, with its final value at least an order of magnitude larger than that of a coherent vortex.

As mentioned in section §5.2, coherent material vortex boundaries are formed by a nested set of elliptic LCSs (i.e., closed λ-lines). Figure 5.4 shows two of the coherent vortices and their corresponding λ-lines. We find that for vortex 1, the secondary elliptic LCSs with $\lambda > 1$ lie in the interior of the primary elliptic LCS (i.e., the closed λ-line with $\lambda = 1$). For all other coherent vortices of figure 5.2, the secondary elliptic LCSs with $\lambda > 1$ lie in the exterior of the primary elliptic LCS. In all five cases, values of λ for which an elliptic LCS exists are close to 1, ranging in the interval $0.94 \leq \lambda \leq 1.05$.

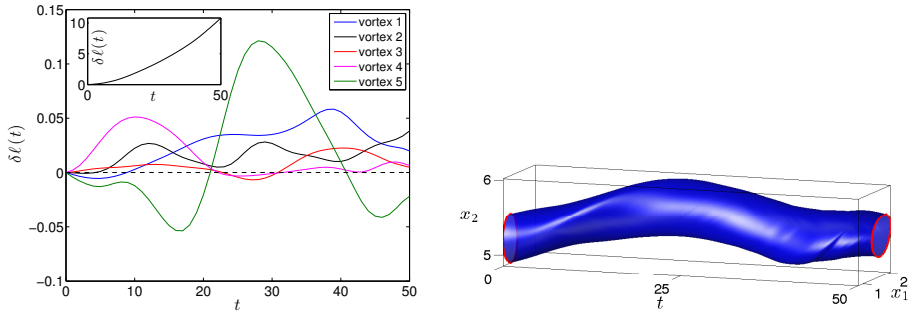

(a) (b)

Figure 5.3: (a) The relative deformation as a function of time for the primary elliptic LCSs. The inset shows the relative stretching for a typical closed material line over the same time interval. (b) The Lagrangian vortex 1 in the extended phase space. The tube is created from the advection of the vortex boundary under the flow.

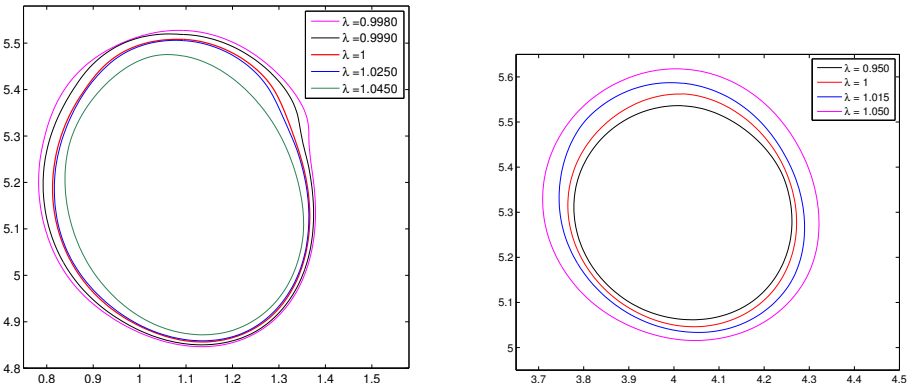

(a) (b)

Figure 5.4: Elliptic LCSs (i.e., closed λ-lines) around vortex 1 (a) and vortex 2 (b).

The majority of vortices appearing in figure 5.2a are not coherent in the Lagrangian frame, and hence no elliptic LCSs were found around them. Some of the non-coherent vortices are trapped in a hyperbolic region and experience substantial straining over time. Some others undergo a merger process where a larger vortex is created from two smaller co-rotating vortices. Each smaller vortex deforms substantially during the merger. The merged vortex may or may not remain coherent for later times.

Figure 5.5 focuses on one Eulerian vortex undergoing a merger process. To illustrate the deformation of this vortex, we take three vorticity contours at

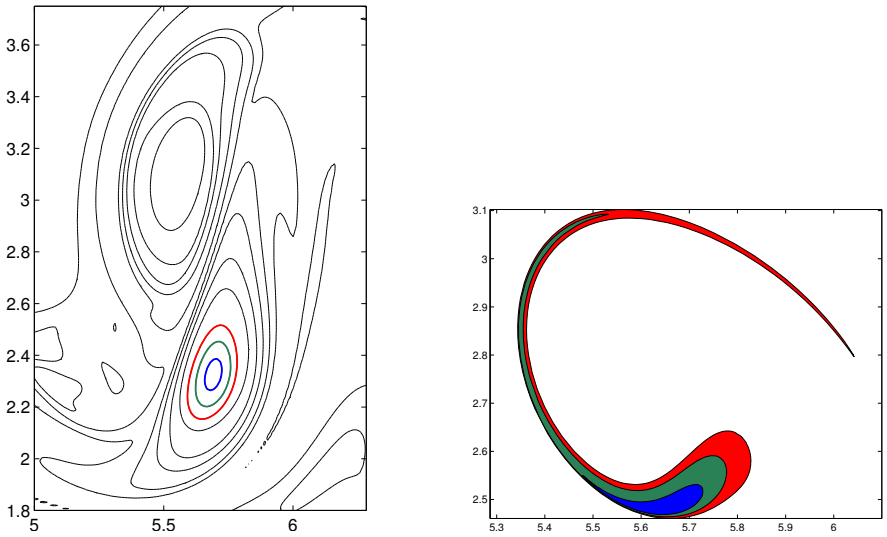

(a) (b)

Figure 5.5: (a) Vortex contours at $t = 0$ for two non-coherent vortices that merge as one later in time. To demonstrate the deformation of the vortices we monitor the advection of three vorticity contours. The contour values are 0.6 (red), 0.7 (green) and 0.8 (blue). (b) The selected contours advected to time $t = 50$ and filled with their corresponding color.

time $t = 0$ near the center of the vortex. Selected vorticity contours are then advected to the final time $t = 50$, showing the resulting deformation of the vortex core. Figure 5.6 shows a similar analysis for a non-coherent vortex trapped in a uniformly hyperbolic region of the flow. Hyperbolicity produces stretching of vorticity gradients resulting in smearing of the vortex.

Figure 5.7 shows the generalized stable and unstable manifolds obtained by the geodesic theory of Lagrangian coherent structures [23, 50], using the computational method described in [49]. These stable and unstable manifolds are, respectively, the most repelling and attracting material lines that form the skeleton of turbulent mixing patterns. The exponential attraction and repulsion generated by these manifolds leads to smearing of most fluid regions that appear as vortices in instantaneous streamline and vorticity plots. By contrast, coherent vortices we identify remain immune to extensive straining.

5.3.3 Optimality of coherent vortex boundaries

Here we consider the optimality of vortex boundaries obtained as outermost elliptic LCSs. The optimal boundary of a coherent vortex can be defined as a closed material line that encircles the largest possible area around the vortex and shows no filamentation over the observational time period. We seek to

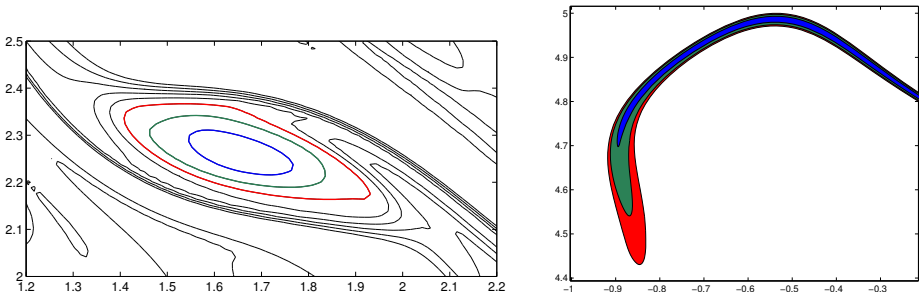

(a) (b)

Figure 5.6: (a) Vortex contours at $t = 0$ for a non-coherent vortex trapped in a straining field. The contours of vorticity with values 0.25 (red), 0.3 (green) and 0.35 (blue) are marked. (b) The selected contours advected to time $t = 50$ and filled with their corresponding color. Only part of the advected image is shown.

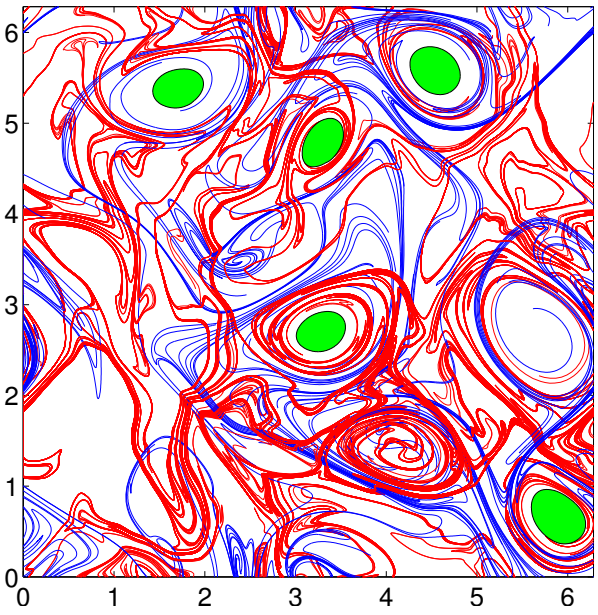

Figure 5.7: Generalized stable (red) and unstable (blue) manifolds. The coherent Lagrangian vortices (green), i.e. generalized KAM regions, are not penetrated by these manifolds. The manifolds and the KAM regions are shown at $t = 50$.

illustrate that outermost elliptic LCSs mark such optimal boundaries.

To this end, we considered a class of perturbations to the outermost elliptic LCS of vortex 1 corresponding to $\lambda = 0.998$. The perturbations are in the

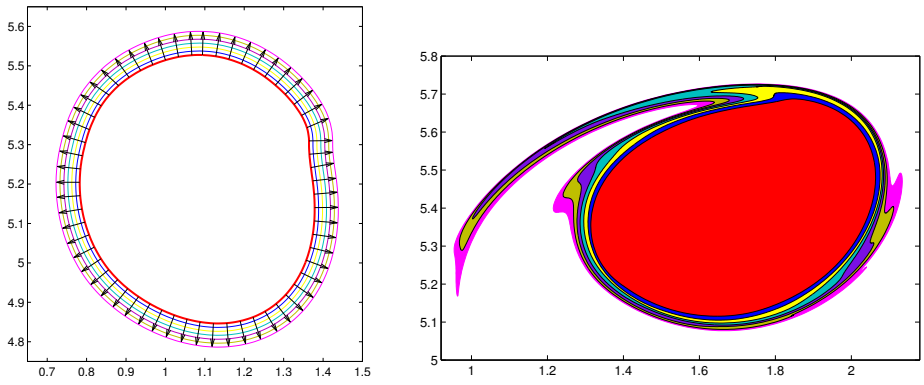

(a) (b)

Figure 5.8: (a) The outermost elliptic LCS (red) encircling vortex 1 of figure 5.2 and its outer normal perturbations. The perturbation parameter ranges between 0.01 and 0.06. (b) The advected image of the elliptic LCS and its normal perturbations at time $t = 50$. Each advected image is filled with its corresponding color from panel (a)

direction of the outer normal of the elliptic LCS. The amount of perturbation ranges between 0.01 and 0.06 (i.e., 1.5% to 10% of the diameter of the elliptic LCS). We then advect the vortex boundary and its perturbations to the final time $t = 50$ (see figure 5.8b). The perturbed curves visibly depart from the coherent core marked by the red elliptic LCS. Our findings are similar for all other coherent vortices (not shown here).

5.3.4 Comparison with Eulerian and Lagrangian vortex indicators

There are several indicators that have been previously developed to mark vortex boundaries. Among the Eulerian indicators are vorticity criterion of McWilliams [150], Okubo-Weiss (OW) criterion [140, 141] and the modified OW criterion of [142], to name a few. These Eulerian methods are instantaneous in nature and cannot be expected to capture long-term coherence in the Lagrangian frame. Nevertheless, they are broadly believed to be good first-order indicators of coherence in the flow.

We find that the coherent vortex boundaries obtained as outermost elliptic LCSs cannot be approximated by the instantaneous vorticity contours at the initial time $t = 0$. Figure 5.9 compares these vortex boundaries with the vorticity contours for two of the coherent vortices. None of the vorticity contours approximates the actual observed coherent vortex boundary of the Lagrangian frame. In fact, the nearby vorticity contours are not axisymmetric, even though that is intuitively expected for a vortex boundary [150]. For instance, we mark

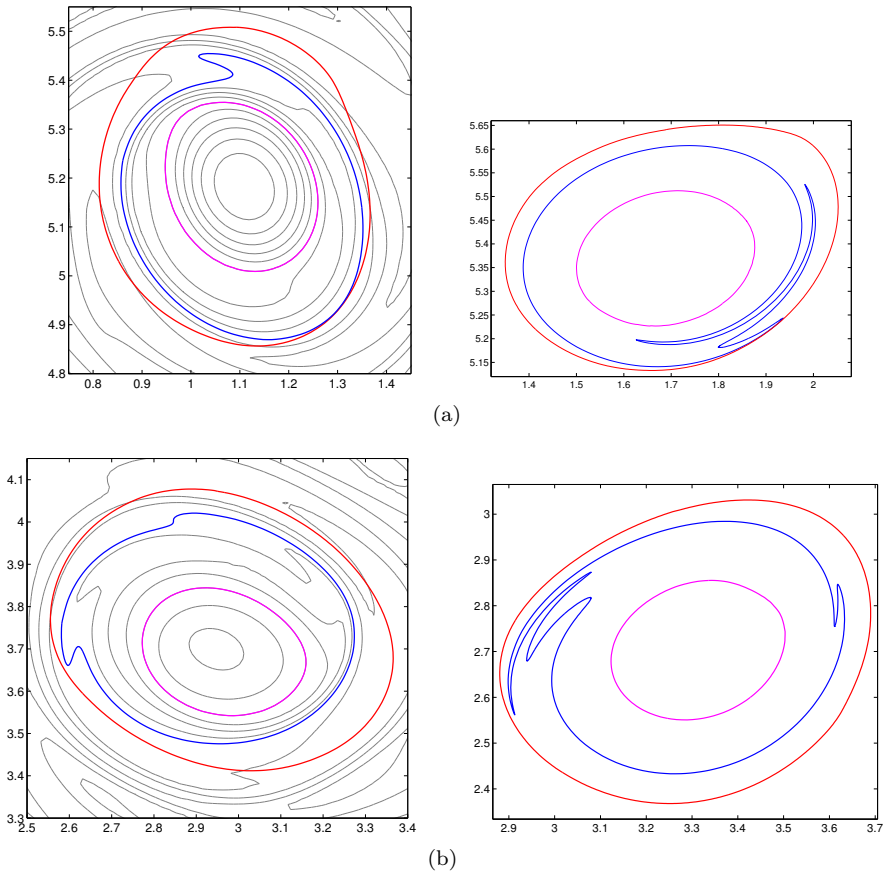

Figure 5.9: (a) Left: Vorticity contours (gray) and the Lagrangian vortex boundary (red) for vortex 1 at time $t = 0$. The blue curve marks the closed vorticity contour that lays entirely inside the elliptic LCS. This contour corresponds to $\omega = -0.3$. The magenta curve marks the closest axisymmetric vorticity contour to the elliptic LCS. Right: The Lagrangian vortex boundary and selected vorticity contours advected to time $t = 50$. (b) Same as (a) for vortex 3. The contour marked by the blue curve corresponds to $\omega = -0.32$.

the closest contour to the elliptic LCS in blue which notably lacks axisymmetry. Its advected image at time $t = 50$ develops filaments. On the other hand, the magenta-colored axisymmetric contour closest to the elliptic LCS preserves its overall shape. This contour would, however, significantly underestimate the true extent of the coherent fluid region.

Similar observations can be made for the OW criterion. The OW parameter

$$Q = \frac{1}{2}\left(|S|^2 - |\Omega|^2\right), \tag{5.8}$$

measures instantaneous straining against instantaneous rotation. Here, S and Ω are, respectively, the symmetric and anti-symmetric parts of the velocity gradient ∇u. The subset of the domain where $Q > 0$ is dominated by strain, while $Q < 0$ marks the regions dominated by vorticity. As a result, the zero contour of this parameter encircling a vortex may be expected to mark the outermost boundary of the vortical region. It has been pointed out by several authors (see, e.g., [151]), however, that the zero contours of Q will not necessarily mark vortex-like structures.

We also find that the outermost elliptic LCS marking the observed material boundary of a coherent vortex is not approximated by the zero contour of the OW parameter. In fact, none of the OW contours approximate well the true coherent vortex boundary (see figure 5.10). The closest OW contour (blue curve) to the outermost elliptic LCS lacks axisymmetry and develops substantial filamentation under advection. The axisymmetric contour (magenta curve) contained in the coherent vortex preserves its shape but seriously underestimates the extent of the coherent region (as do axisymmetric vorticity contours). This axisymmetric contour of the OW parameter is also the outermost contour that remains in the $Q < 0$ region over the entire time interval $t \in [0, 50]$.

We make a similar observation about other OW-type Eulerian indicators that have been developed to overcome the shortcomings of the OW criterion (see, e.g., [152–154, 142]).

Hua and Klein [142], for instance, consider the effect of higher-order terms due to fluid acceleration. They arrive at the indicator parameters $\lambda_\pm$ given by

$$\lambda_\pm = Q \pm \sqrt{|\dot{S}|^2 - |\dot{\Omega}|^2},$$

where $\dot{S}$ and $\dot{\Omega}$ denote, respectively, the instantaneous rate of change of strain and vorticity along fluid trajectories. The scalar Q is the OW parameter, defined in (5.8). The positive extrema of λ_+ correspond to regions of instantaneously strong stirring and dispersion. The negative extrema of λ_-, on the other hand, mark the vortex regions.

As in the case of vorticity and the OW-parameter, we find that the Lagrangian vortex boundaries cannot be inferred from the contours of the $\lambda_\pm$ parameters (see figure 5.11). The axisymmetric contours of $\lambda_\pm$ remain coherent under material advection over the time interval $t \in [0, 50]$. They, however, are significantly smaller (in enclosed surface area) than the true Lagrangian vortex boundary marked by the elliptic LCS.

Compared to the Eulerian criteria, there are far less Lagrangian indicators developed for quantifying coherent vortices. Such Lagrangian indicators include finite-time Lyapunov exponent [54, 151] and mesoellipticity [38]. We compare our results with these two diagnostics. More recent notions of Lagrangian coherence also include relative coherent pairs [28, 29], shape coherence [26] and ergodic partition of time-averaged observables [155].

Finite-time Lyapunov exponent (FTLE) measures the maximal local stretching of material lines. The FTLE corresponding to a time interval $[a, b]$ is defined

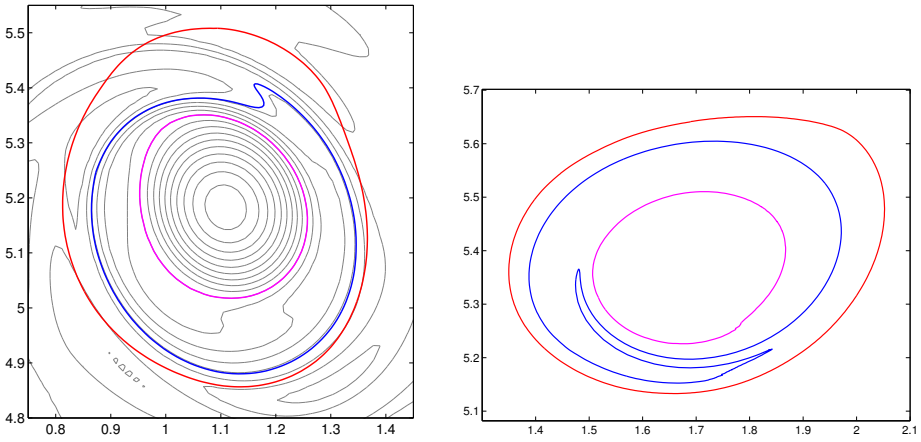

(a)

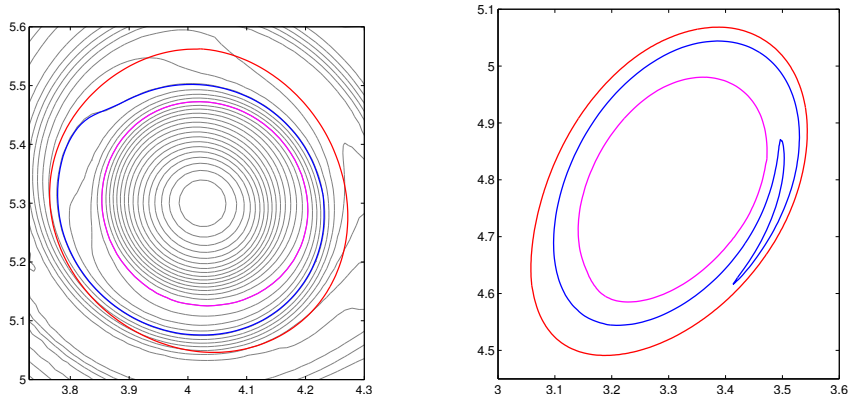

(b)

Figure 5.10: (a) Left: OW contours (gray) and the Lagrangian vortex boundary (red) for vortex 1 at time $t = 0$. Two contours corresponding to $Q = -0.018$ (blue) and $Q = -0.06$ (magenta) are selected for advection. Right: The Lagrangian vortex boundary and selected OW contours advected to time $t = 50$. (b) Same as (a) for vortex 2. Here, the OW contours corresponding to $Q = -0.024$ (blue) and $Q = -0.10$ (magenta) are selected for advection.

as

$$\Lambda(x_a) = \frac{1}{2(b-a)} \log(\lambda_2(x_a)), \tag{5.9}$$

for any point $x_a \in U$ where λ_2 is the larger eigenvalue of the Cauchy–Green strain tensor C. The FTLE measures the maximum separation of nearby initial conditions over the given time interval. Therefore, its higher values mark regions with high mixing. Conversely, regions with relatively small FTLE values experience less mixing. As a result, one may expect that low-FTLE regions co-

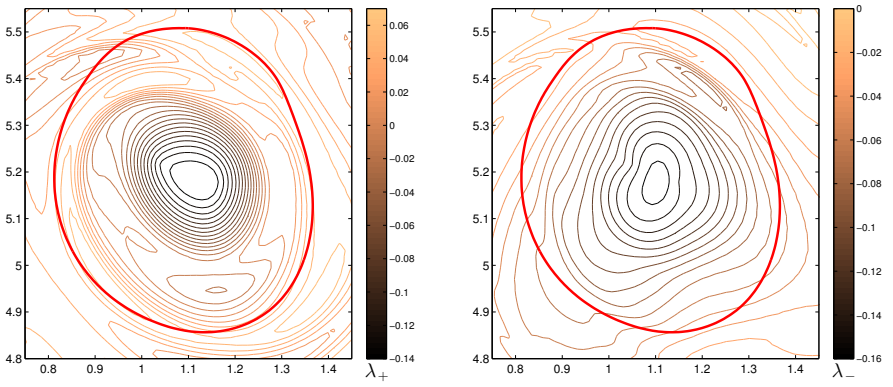

Figure 5.11: The contours of λ_+ (left) and λ_- (right) around vortex 1 at time $t = 0$. The Lagrangian vortex boundary is shown with thick red line.

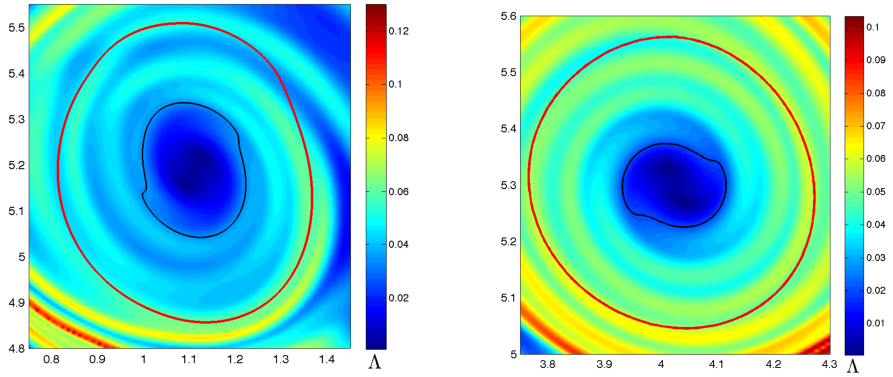

(a) (b)

Figure 5.12: (a) Time $t = 0$ position of the Lagrangian vortex boundary (red) for vortex 1. The background color shows the FTLE field. The black curve marks the FTLE contour with $\Lambda = 3.45 \times 10^{-2}$. The FTLE value is chosen such that the corresponding contour is the outermost, almost-axisymmetric contour encircling the vortex core. (b) Same as (a) for vortex 2. Here, the value of the FTLE contour is $\Lambda = 2.0 \times 10^{-2}$

incide with the coherent vortex regions identified as interiors of the outermost elliptic LCSs.

Figure 5.12 shows the color-coded FTLE values for vortices 1 and 2. Clearly, the Lagrangian vortex boundary (red curves) cannot be inferred from the FTLE plot. In fact, locally maximal values of FTLE spiral into the Lagrangian vortex boundary, giving the wrong impression that it will stretch significantly under advection.

In addition, FTLE contours around the vortex core lack axisymmetry. The

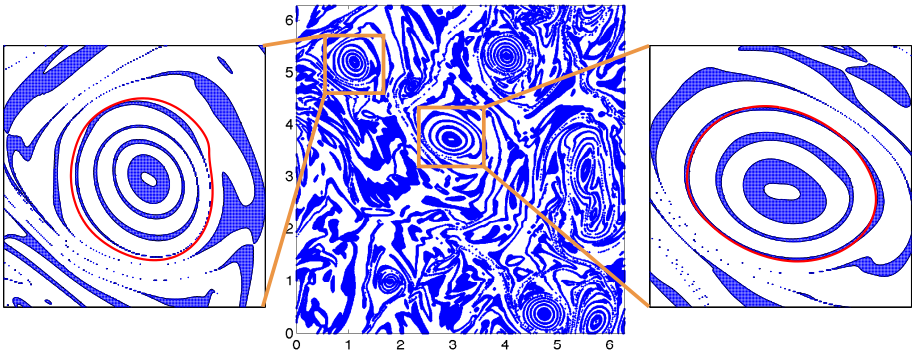

Figure 5.13: The mesoelliptic regions (blue) compared to two elliptic LCSs (red).

outermost, almost-axisymmetric FTLE contours encircling the vortex cores (black curves) are clearly far from the true vortex boundary marked by the elliptic LCS.

We conclude this section with a comparison between elliptic LCSs and elliptic regions obtained from the Lagrangian mixing diagnostic of [38]. This diagnostic classifies a trajectory starting from a point x_a as *mesoellipitic* in an incompressible flow, if the eigenvalues of the deformation gradient $DF(x_a)$ lie on the complex unit circle. Mesoelliptic trajectories are expected to lie in a vortical region. In contrast, if the eigenvalues of $DF(x_a)$ are off the complex unit circle , the trajectory is classified as *mesohyperbolic* and is expected to lie in a strain-dominated region.

Figure 5.13 shows the mesoelliptic (blue) and mesohyperbolic (white) regions in our turbulent flow. The actual Lagrangian coherent vortex boundaries (i.e., the outermost elliptic LCS) are shadowed by nearby thin mesoelliptic regions. At the same time, substantial portions of the vortices are diagnosed as mesohyperbolic (annular white regions). Also, a number of mesoelliptic regions appear in non-coherent, hyperbolic mixing regions (compare to figure 5.7) which undergo substantial stretching and filamentation. Due to such observations, we could not establish a systematic a priori criterion for extracting a coherent vortex boundary from this diagnostic.

5.4 Conclusions

We have used the variational theory of [24] to detect the boundaries of coherent vortices in a direct numerical simulation of two-dimensional Navier–Stokes turbulence. We demonstrated that these boundaries are optimal in the sense that they are the outermost material lines enclosing a vortex and retaining their shape over long time intervals. They are also frame-independent and Lagrangian by nature.

A comparison with other Eulerian methods (vorticity contours, Okubo-Weiss

criterion, λ-parameters) shows that the size of coherent vortices of turbulence is substantially larger than what has been thought before based on Eulerian indicators. At the same time, the actual number of coherent vortices is lower than what is signaled by the same indicators. This is consistent with the findings in [156], who observed a similar trend for the ocean eddies in satellite-altimetry-based velocity fields of the South Atlantic. We find that the superfluous vortices suggested by Eulerian indicators are destroyed relatively quickly by the straining induced by repelling and attracting Lagrangian coherent structures present in the flow.

We also compared our results with two Lagrangian indicators: the finite-time Lyapunov exponent (FTLE) and the mesoellipticity of [38]. The FTLE field indicates the approximate position of vortex cores with a relatively low FTLE value. However, it does not provide an indication of the coherent Lagrangian vortex boundary. As a rule, we have found mesoelliptic regions near the actual coherent Lagrangian vortex boundary. However, the results are difficult to interpret as portions of coherent vortices are diagnosed as mesohyperbolic and, at the same time, there exist mesoelliptic regions that experience substantial straining.

Compared to instantaneous Eulerian indicators, such as Okubo-Weiss criterion, our vortex detection is clearly computationally more expensive. It requires accurate advection of a large ensemble of fluid particles, as well as, closed orbit detection in the vector fields (5.6). Therefore, developing cost effective computational algorithms while staying faithful to the underlying theory is of great interest (see [157–159], for recent developments).

Future theoretical work will focus on the correlation between Lagrangian coherent vortices and the dynamical properties of the flow, e.g., the scale-by-scale transfer of energy and enstrophy [160].

Chapter 6

Detecting invariant manifolds, attractors, and generalized KAM tori in aperiodically forced mechanical systems

6.1 Introduction

A number of numerical and analytical techniques are available to analyze externally forced nonlinear mechanical systems. Indeed, perturbation methods, Lyapunov exponents, Poincaré maps, phase space embeddings and other tools have been broadly used in mechanics [6]. Still, most of these techniques, are only applicable to nonlinear systems subject to autonomous (time-independent), time-periodic, or time-quasiperiodic forcing.

These recurrent types of forcing allow for the analysis of asymptotic features based on a finite-time sample of the underlying flow map–the mapping that takes initial conditions to their later states. Indeed, to understand the phase space dynamics of an autonomous system, knowing the flow map over an arbitrary short (but finite) time interval is enough, as all trends can be reproduced by the repeated applications of this short-time map. Similarly, the period map of a time-periodic system (or a one-parameter family of flow maps for a time-quasiperiodic system) renders asymptotic conclusions about recurrent features, such as periodic and quasiperiodic orbits, their stable and unstable manifolds, attractors, etc.

By contrast, the identification of key features in the response of a nonlinear system under time-aperiodic forcing has remained an open problem. Mathe-

matically, the lack of precise temporal recurrence in such systems prevents the use of a compact extended phase space on which the forced system would be autonomous. This lack of compactness, in turn, renders most techniques of nonlinear dynamics inapplicable. Even more importantly, a finite-time understanding of the flow map can no longer be used to gain a full understanding of a (potentially ever-changing) non-autonomous system.

Why would one want to develop an understanding of mechanical systems under aperiodic, finite-time forcing conditions? The most important reason is that most realistic forms of forcing will take time to build up, and hence will be transient in nature, at least initially. Even if the forcing is time-independent, the finite-time transient response of a mechanical system is often crucial to its design, as the largest stresses and strains invariably occur during this period.

Similar challenges arise in fluid dynamics, where temporally aperiodic unsteady flows are the rule rather than the exception. Observational or numerical data for such fluid flows is only available for a limited time interval, and some key features of the flow may only be present for an even shorter time. For instance, the conditions creating a hurricane in the atmosphere are transient, rather than periodic, in nature, and the hurricane itself will generally only exist for less than two weeks [161]. As a result, available asymptotic methods are clearly inapplicable to its study, even though there is great interest in uncovering its internal structure and overall dynamics.

In response to these challenges in fluid dynamics, a number of diagnostic tools have been developed [57, 162]. Only recently, however, has rigorous mathematical theories emerged for dynamical structures in finite-time aperiodic flow data, some of which were either developed or reviewed in previous chapters. These theories find that finite-time invariant structures in a dynamical system are governed by intrinsic, metric properties of the finite-time flow map.

In this chapter, we briefly review the theory and methods in the context of one-degree-of-freedom, aperiodically forced mechanical systems. We then show how they uncover key invariant sets under both conservative and dissipative forcing in cases where classic techniques, such as Poincaré maps, are not available. Remarkably, these finite-time invariant sets can be explicitly identified as parametrized curves, as opposed to plots requiring post-processing or feature extraction.

The organization of this chapter is as follows. Section §6.2 is divided into two subsections: Section §6.2.1 provides the necessary background. In section §6.2.2, we describe the numerical implementation. Section §6.3 presents results from the application of this numerical algorithm to one degree-of-freedom mechanical systems. First, as a proof of concept, §6.3.1 considers conservative and dissipative time-periodic Duffing oscillators, comparing their LCS-based extracted invariant sets with those obtained form Poincaré maps. Next, section §6.3.2 deals with invariant sets in aperiodically forced Duffing oscillators, for which Poincaré maps or other rigorous extraction methods are not available. We conclude the chapter with a summary and outlook.

6.2 Set-up

The key invariant sets of autonomous and time-periodic dynamical systems–such as fixed points, periodic and quasiperiodic motions, their stable and unstable manifolds, and attractors–are typically distinguished by their asymptotic properties. In contrast, invariant sets in finite-time, aperiodic dynamical systems solely distinguish themselves by their observed impact on trajectory patterns over the finite time interval of their definition. This observed impact is a pronounced lack of trajectory exchange (or transport) across the invariant set, which remains coherent in time, i.e., only undergoes minor deformation. Well-understood, classic examples of such transport barriers include local stable manifolds of saddles, parallel shear jets, and KAM tori of time-periodic conservative systems. Until recently, a common dynamical feature of these barriers has not been identified, hindering the unified detection of transport barriers in general non-autonomous dynamical systems.

As noted recently in [23], however, a common feature of all canonical transport barriers in two dimensions is that they stretch less under the flow than neighboring curves of initial conditions do. This observation leads to a non-standard calculus of variations problem with unknown endpoints and a singular Lagrangian. Below we recall the solution of this problem from [23], with a notation and terminology adapted to one-degree-of-freedom mechanical oscillators.

A one-degree-of-freedom forced nonlinear oscillator can generally be written as a two-dimensional dynamical system

$$\dot{x} = v(x,t), \quad x \in U \subset \mathbb{R}^2, \quad t \in [t_0, t_1], \tag{6.1}$$

with U denoting an open set in the state space, where the vector x labels tuples of positions and velocities. The vector $v(x,t)$, assumed twice continuously differentiable, contains the velocity and acceleration of the system at state x and at time t.

Let $x(t_1; t_0, x_0)$ denote the final state of system (6.1) at time t_1, given its state x_0 at an initial time t_0. The flow map associated with (6.1) over this time interval is defined as

$$F_{t_0}^{t_1} : \mathbf{x}_0 \longmapsto \mathbf{x}(t_1; t_0, x_0), \tag{6.2}$$

which maps initial states to final states at t_1. The Cauchy–Green (CG) strain tensor associated with the flow map (6.2) is defined as

$$C_{t_0}^{t_1}(x_0) = [DF_{t_0}^{t_1}(x_0)]^\top DF_{t_0}^{t_1}(x_0), \tag{6.3}$$

where $DF_{t_0}^{t_1}$ denotes the gradient of the flow map (6.2), and the symbol $\top$ refers to matrix transposition.

Note that the CG tensor is symmetric and positive definite. As a result, it has two positive eigenvalues $0 < \lambda_1 \leq \lambda_2$ and an orthonormal eigenbasis $\{\xi_1, \xi_2\}$. We fix this eigenbasis so that

$$\begin{aligned} &C_{t_0}^{t_1}(x_0)\xi_i(x_0) = \lambda_i(x_0)\xi_i(x_0), \quad |\xi_i(x_0)| = 1, \quad i \in \{1,2\}, \\ &\xi_2(x_0) = \Omega\xi_1(x_0), \quad \Omega = \begin{pmatrix} 0 & -1 \\ 1 & 0 \end{pmatrix}. \end{aligned} \tag{6.4}$$

We suppress the dependence of λ_i and ξ_i on t_0 and t_1 for notational simplicity.

6.2.1 Transport barriers in phase space

A *material line* $\gamma_t = F_{t_0}^t(\gamma_{t_0})$ is an evolving curve of initial conditions γ_{t_0} under the flow map $F_{t_0}^t$. As shown in [23], for such a material line to be a locally least-stretching curve over $[t_0, t_1]$, it must be a hyperbolic, a parabolic or an elliptic line (see figure 6.1).

The initial position γ_{t_0} of a hyperbolic material line is tangent to the vector field ξ_1 at all its points. Such material lines are compressed by the flow by locally the largest rate, while repelling all nearby material lines at an exponential-in-time rate. The classic example of a hyperbolic material lines is the unstable manifold of a saddle-type fixed point.

An elliptic material line is a closed curve whose initial position γ_{t_0} is tangent to one of the directions of locally largest shear. At each point of the phase space, the two directions of locally largest shear are given by

$$\eta_\pm = \sqrt{\frac{\sqrt{\lambda_2}}{\sqrt{\lambda_1}+\sqrt{\lambda_2}}}\xi_1 \pm \sqrt{\frac{\sqrt{\lambda_1}}{\sqrt{\lambda_1}+\sqrt{\lambda_2}}}\xi_2, \tag{6.5}$$

as derived in [23]. Elliptic material lines still repel most nearby material lines (except for those parallel to them), but only at a rate that is linear in time. Classic examples of elliptic material lines are closed trajectories of a steady, circular shear flow, such as a vortex.

Initial positions of hyperbolic material lines are, by definition, *strainlines*, i.e., trajectories of the autonomous differential equation

$$r' = \xi_1(r), \qquad r \in U \subset \mathbb{R}^2, \tag{6.6}$$

where $r : [0, \ell] \mapsto U$ is the parametrization of the strainline by arc-length. A *hyperbolic barrier* is then a locally least-stretching strainline

Similarly, initial positions of elliptic material lines are, by definition, closed *shearlines*, i.e., closed trajectories of the autonomous differential equation

$$r' = \eta_\pm(r), \qquad r \in U \subset \mathbb{R}^2. \tag{6.7}$$

For the purposes of the present discussion, we call a mechanical system of the form (6.1) *conservative* if it has vanishing divergence, i.e., $\nabla \cdot v(x,t) = 0$, with ∇ referring to differentiation with respect to x. This property implies that flow map of (6.1) conserves phase-space area for all times [47].

While a typical material line in such a conservative system will still stretch and deform significantly over time, the length of a shearline will always be preserved under the area-preserving flow map $F_{t_0}^{t_1}$ (cf. [23]). An elliptic barrier in a conservative system will, therefore, have the same enclosed area and arclength at the initial time t_0 and at the final time t_1. These two conservation properties imply that an elliptic barrier in a non-autonomous conservative system may only undergo translation, rotation and some slight deformation, but will

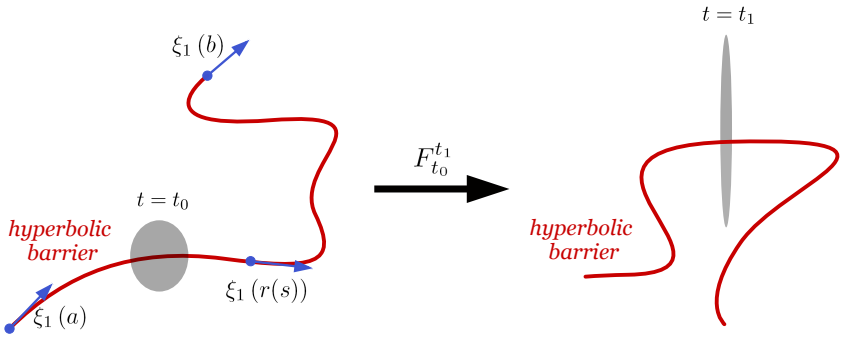

(a) A repelling hyperbolic barrier (red curve) repels nearby trajectories (gray blob) exponentially fast in time.

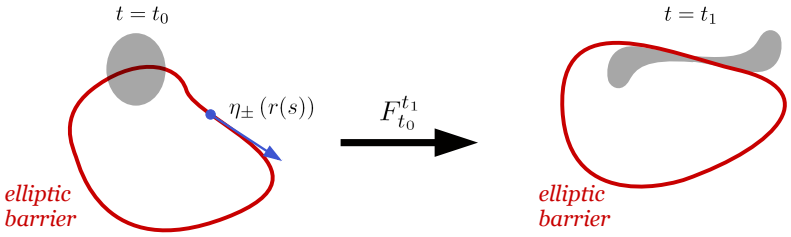

(b) An elliptic barrier (red curve) is a *closed* curve with the locally largest rate of Lagrangian shear along its tangent.

Figure 6.1: Two types of transport barriers in two-dimensional flows.

otherwise preserve its overall shape. As a result, the interior of an elliptic barrier will not mix with the rest of the phase-space, making elliptic barriers the ideal generalized KAM curves in aperiodically forced conservative mechanical systems.

6.2.2 Computation of invariant sets as transport barriers

In this section, we describe numerical algorithms for the extraction of hyperbolic and elliptic barriers in a one-degree-of-freedom mechanical system with general time dependence.

Our numerical algorithms require a careful computation of the CG tensor. In most mechanical systems, trajectories separate rapidly, resulting in an exponential growth in the entries of the CG tensor. This growth necessitates the use of a well-resolved grid, as well as the deployment of high-end integrators in solving for the trajectories of (6.1) starting form this grid. Further computational challenges arise from the handling of the unavoidable orientational discontinuities and isolated singularities of the eigenvector fields ξ_1 and ξ_2 (see Chapter 1).

As a zeroth step, we fix a sufficiently dense grid $\mathcal{G}_0$ of initial conditions in

the phase-space U, then advect the grid points from time t_0 to time t_1 under system (6.1). This gives a numerical representation of the flow map $F_{t_0}^{t_1}$ over the grid $\mathcal{G}_0$. The CG tensor field $C_{t_0}^{t_1}$ is then obtained by definition (6.3) from $F_{t_0}^{t_1}$. In computing the gradient $DF_{t_0}^{t_1}$, we use careful finite differencing over an auxiliary grid, as described in Chapter 1.

Since, at each point $x_0 \in \mathcal{G}_0$, the tensor $C_{t_0}^{t_1}(x_0)$ is a two-by-two matrix, computing its eigenvalues $\{\lambda_1, \lambda_2\}$ and eigenvectors $\{\xi_1, \xi_2\}$ is straightforward. With the CG eigenvalues and eigenvectors at hand, we locate the hyperbolic barriers using the following algorithm.

Algorithm 6.1 (Locating hyperbolic barriers)**.**

1. Calculate strainlines by solving the ODE (6.6) numerically, with linear interpolation of the strain vector field between grid points.

2. Locate hyperbolic barriers as strainline segments γ_{t_0} with locally minimal relative stretching, i.e., strainline segments that locally minimize the function
$$q(\gamma_{t_0}) = \frac{l(\gamma_{t_1})}{l(\gamma_{t_0})}. \tag{6.8}$$
Here $l(\gamma_{t_0})$ and $l(\gamma_{t_1})$ denote the length of the strainline γ_{t_0} and the length of its advected image γ_{t_1}, respectively.

Computing the relative stretching (6.8) of a strainline γ_{t_0}, in principle, requires advecting the strainline to time t_1. However, as shown in [23], the length of the advected image satisfies $l(\gamma_{t_1}) = \int_{\gamma_{t_0}} \sqrt{\lambda_1}\, ds$, where the integration is carried out along the strainline γ_{t_0}. This renders the strainline advection unnecessary.

Numerical experiments have shown that a direct computation of ξ_1 is usually less accurate than that of ξ_2 due to the attracting nature of strongest eigenvector of the CG tensor [48]. For this reason, computing ξ_1 as an orthogonal rotation of ξ_2 is preferable. Moreover, it was shown in Chapter 2 that strainlines can be computed more accurately as advected images of *stretchlines*, i.e. curves that are everywhere tangent to the second eigenvector of the *backward-time* CG tensor $C_{t_1}^{t_0}$. In the present chapter, this approach is taken for computing the strainlines.

Computing elliptic barriers amounts to finding limit cycles of the ODE (6.7). To this end, we follow the approach used in [23, 49] by first identifying candidate regions for shear limit cycles visually, then calculating the Poincaré map on a one-dimensional section transverse to the flow within the candidate region (see figure 6.2). Hyperbolic fixed points of this map can be located by iteration, marking limit cycles of the shear vector field (see [49] for more detail).

This process is used in the following algorithm to locate elliptic barriers.

Algorithm 6.2 (Locating elliptic barriers)**.**

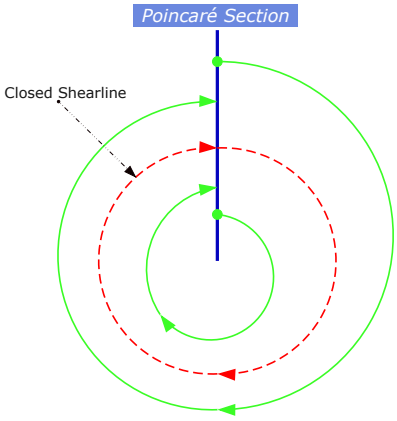

Figure 6.2: Locating closed shearlines using a Poincaré section of the shear vector field. Closed shearlines pass through the fixed points of the corresponding Poincaré map.

1. Visually locate the regions where closed shearlines may exist[1]. Construct a sufficiently dense Poincaré map, as discussed above. Locate the fixed points of the Poincaré map by iteration.

2. Compute the full closed shearlines emanating from the fixed points of the Poincaré map.

In the next section, we use the above algorithms for locating invariant sets in simple forced and damped nonlinear oscillators.

6.3 Results

We demonstrate the implementation of the above algorithms on four Duffing-type oscillators. As a proof of concept, in the first two examples (section §6.3.1), we consider *periodically* forced Duffing oscillators for which we can explicitly verify our results using an appropriately defined Poincaré map.

The next two examples deal with *aperiodically* forced Duffing oscillators (section §6.3.2). In these examples, despite the absence of a Poincaré map, we still obtain the key invariant sets as hyperbolic and elliptic barriers.

To implement algorithms 1 and 2 in the forthcoming examples, the CG tensor is computed over a uniform grid $\mathcal{G}_0$ of 1000×1000 points. A fourth order Runge-Kutta method with variable step-size (ODE45 in MATLAB) is used to

[1]Recently, Karrasch et al. [163] developed a method for automatic detection of elliptic barriers that renders this visual inspection unnecessary.

solve the first-order ODEs (6.1), (6.6) and (6.7) numerically. The absolute and relative tolerances of the ODE solver are set equal to 10^{-4} and 10^{-6}, respectively. Off the grid points, the strain and shear vector fields are obtained by bilinear interpolation.

In each case, the Poincaré map of algorithm 6.2 is approximated by 500 points along the Poincaré section. The zeros of the map are located by a standard secant method.

6.3.1 Proof of concept: Periodically forced Duffing oscillator

Case 1: Pure periodic forcing, no damping

Consider the periodically forced Duffing oscillator

$$\begin{aligned} \dot{x}_1 &= x_2, \\ \dot{x}_2 &= x_1 - x_1^3 + \epsilon\cos(t). \end{aligned}$$

For $\epsilon = 0$, the system is integrable with one hyperbolic fixed point at $(0,0)$, and two elliptic fixed points $(1,0)$ and $(-1,0)$, respectively. As is well known, there are two homoclinic orbits connected to the hyperbolic fixed point, each enclosing an elliptic fixed point, which is in turn surrounded by periodic orbits. These periodic orbits appear as closed invariant curves for the Poincaré map $P := F_0^{2\pi}$. The fixed points of the flow are also fixed points of P.

For $0 < \epsilon \ll 1$, the Kolmogorov–Arnold–Moser (KAM) theory [47] guarantees the survival of most closed invariant sets for P. Figure 6.3 shows these surviving invariant sets (KAM curves) of P obtained for $\epsilon = 0.08$. For the KAM curves to appear continuous-looking, nearly 500 iterations of P were needed, requiring the advection of initial conditions up to time $t = 1000\pi$. The stochastic region surrounding the KAM curves is due to chaotic dynamics arising from the transverse intersections of the stable and unstable manifold of the perturbed hyperbolic fixed point of P.

The surviving KAM curves are well-known, classic examples of transport barriers. We would like to capture as many of them as possible as elliptic barriers using Algorithm 6.2. Note that not all KAM curves are expected to prevail as locally least-stretching curves for a given choice of the observational time interval $[t_0, t_1]$; some of these curves may take longer to prevail due to their shape and shearing properties.

We use the elliptic barrier extraction algorithm of section 6.2.2. Figure 6.4 shows the resulting shearlines in the KAM regions, with the closed ones marked by red. Note that these shearlines were obtained from the CG tensor computed over the time interval $[0, 8\pi]$, spanning just four iterations of the Poincare map. Despite this low number of iterations, the highlighted elliptic barriers are practically indistinguishable form the KAM curves obtained from five hundred iterations.

Figure 6.5 shows the convergence of an elliptic barrier to a KAM curve as the integration time $T = t_1 - t_0$ increases.

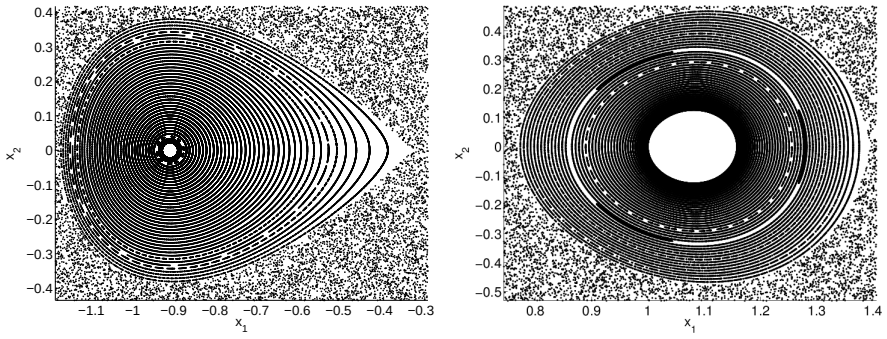

Figure 6.3: Five hundred iterations of the Poincaré map for the periodically forced Duffing oscillator. Two elliptic regions of the phase-space filled by KAM tori are shown.

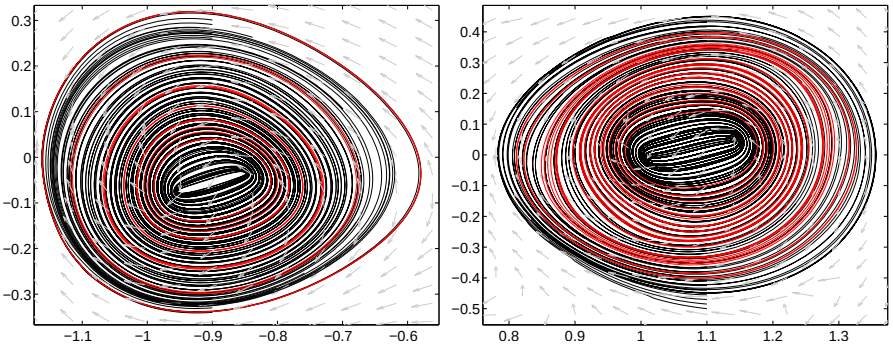

Figure 6.4: Shearlines (black) of the periodically forced Duffing oscillator computed at $t_0 = 0$, with integration time $T = 8\pi$.

Remarkably, constructing these elliptic barriers requires significantly shorter integration time (only four forcing periods) in comparison to visualization through the Poincaré map, which required 500 forcing periods to reveal KAM curves as continuous objects. Clearly, the overall computational cost for constructing elliptic barriers still comes out to be higher, since the CG tensor needs to be constructed on a relatively dense grid $\mathcal{G}_0$, as discussed in section §6.2.2. This high computational cost will be justified, however, in the case of aperiodic forcing (section §6.3.2), where no Poincaré map is available.

In the context of one-degree-of-freedom mechanical systems, the outermost elliptic barrier marks the boundary between regions of chaotic dynamics and regions of oscillations that are regular on a macroscopic scale. To demonstrate this sharp dividing property of elliptic barriers, we show the evolution of system (6.10) from three initial states, two of which are inside the elliptic region and one of which is outside (figure 6.6a). The system exhibits rapid changes in its state when started from outside the elliptic region. In contrast, more regular behavior

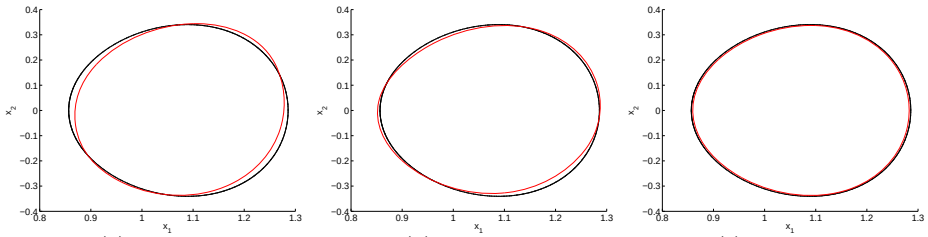

(a) $T = 8\pi$ (b) $T = 10\pi$ (c) $T = 12\pi$

Figure 6.5: Convergence of an elliptic barrier (red) to a KAM curve (black) as the integration time $T = t_1 - t_0$ increases.

is observed for trajectories starting inside the elliptic region. This behavior is further depicted in figure 6.7, which shows the evolution of the x_1-coordinate of the trajectories as a function of time.

Case 2: Periodic forcing and damping

Consider now the damped-forced Duffing oscillator

$$\begin{aligned} \dot{x}_1 &= x_2, \\ \dot{x}_2 &= x_1 - x_1^3 - \delta x_2 + \epsilon \cos(t), \end{aligned} \tag{6.9}$$

with $\delta = 0.15$ and $\epsilon = 0.3$. This system is known to have a chaotic attractor that appears as an invariant set of the the Poincaré map $P = F_0^{2\pi}$ (see, e.g., [6]). Here, we show that the attractor can be very closely approximated by hyperbolic barriers computed via algorithm 6.1.

Figure 6.8a shows strainlines computed backward in time with $t_0 = 0$ and integration time $T = t_1 - t_0 = -8\pi$. The strainline with globally minimal relative stretching (6.8) is shown in figure 6.8b.

The approximate location of the attractor can also be revealed by applying the Poincaré map to a few initial conditions (tracers) released from the basin of attraction. For long enough advection time, the initial conditions converge to the attractor highlighting its position (see figure 6.9a and 6.9b). In figure 6.9c, the hyperbolic barrier is superimposed on the advected tracers showing close agreement between the two. Figure 6.9d shows the tracers advected for a longer time ($T = 40\pi$) together with the hyperbolic barrier; the two virtually coincide. Note that the hyperbolic barrier is a smooth, parametrized curve (computed as a trajectory of (6.6)), while the tracers form a set of scattered points.

6.3.2 The aperiodically forced Duffing oscillator

In the next two examples, we study aperiodically forced Duffing oscillators. In the presence of aperiodic forcing, the Poincaré map P is no longer defined as the

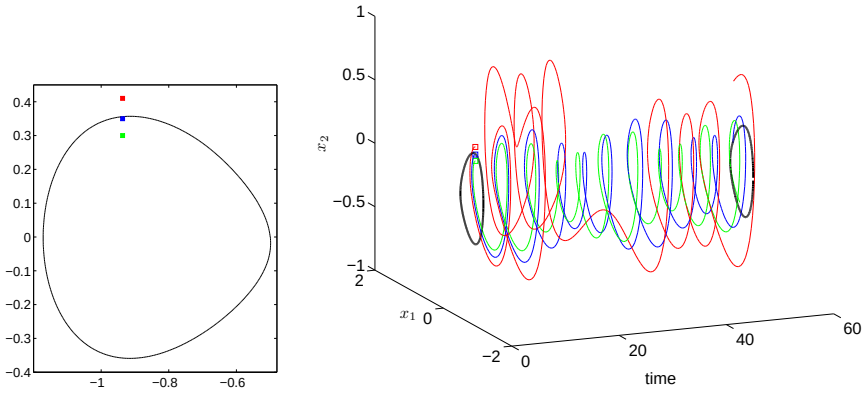

(a) (b)

Figure 6.6: (a) The outermost elliptic barrier (black curve) and three initial conditions: Two inside the elliptic barrier (blue and green) and one outside the elliptic barrier (red). (b) The corresponding trajectories are shown in the extended phase space of (x_1, x_2, t). The closed black curves mark the elliptic barrier at $t_0 = 0$ and $t_1 = 16\pi$.

system lacks any recurrent behavior. However, KAM-type curves (i.e., closed curves, resisting significant deformation) and generalized stable and unstable manifolds (i.e., most repelling and attracting material lines) exist in the phase-space and determine the overall dynamics of the system.

Case 1: Purely aperiodic forcing, no damping

Consider the Duffing oscillator

$$\begin{aligned} \dot{x}_1 &= x_2, \\ \dot{x}_2 &= x_1 - x_1^3 + f(t), \end{aligned} \tag{6.10}$$

where $f(t)$ is an aperiodic forcing function obtained from a chaotic one-dimensional map (see figure 6.10).

While, KAM theory is no longer applicable, one may still expect KAM-type barriers to survive for small forcing amplitudes. Such barriers would no longer be repeating themselves periodically in the extended phase space. Instead, a generalized KAM barrier is expected to be an invariant cylinder, with cross sections showing only minor deformation. The existence of such structures can, however, be no longer studied via Poincaré maps.

Figure 6.11 confirms that generalized KAM-type curves, obtained as elliptic barriers, do exist in this problem. These barriers are computed over the time interval $[0, 4\pi]$ (i.e. $t_0 = 0$ and $t_1 = t_0 + T = 4\pi$). As discussed in section §6.2.1, the arclength of an elliptic barrier at the initial time t_0 is equal to the arclength

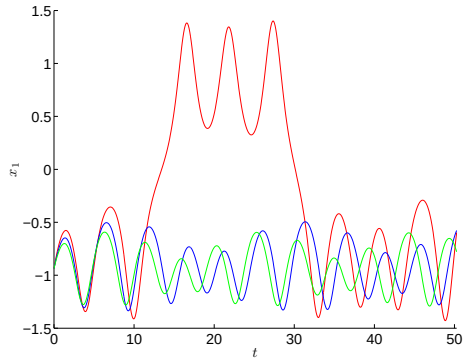

Figure 6.7: The x_1-coordinate of the trajectories of figure 6.6.

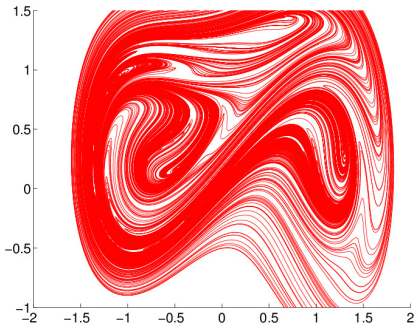

(a) Strainlines computed for the damped-forced Duffing oscillator (6.9) at time $t_0 = 0$, with the integration time $T = -8\pi$.

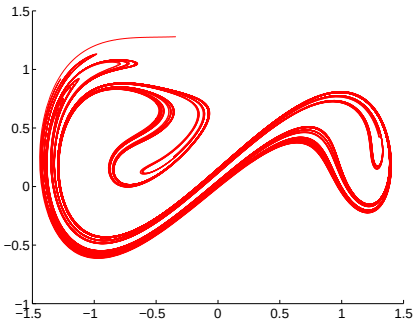

(b) Final approximation of the chaotic attractor by a single, continuous strainline.

Figure 6.8: Construction of the attractor of the damped-forced Duffing oscillator as a hyperbolic transport barrier.

of its advected image under the flow map $F_{t_0}^{t_1}$ at the final time t_1. This arclength preservation is illustrated numerically in figure 6.12, which shows the relative stretching,

$$\delta\ell(t) = \frac{\ell(\gamma_t) - \ell(\gamma_0)}{\ell(\gamma_0)} \tag{6.11}$$

of the time-t image γ_t of an elliptic barrier γ_0, with ℓ referring to the arclength of the curve. Ideally, the relative stretching of each elliptic barrier should be zero at time $t_1 = 4\pi$, i.e. $\delta\ell(4\pi) = 0$. Instead, we find that the relative stretching $\delta\ell(4\pi)$ of the computed elliptic barriers is at most 1.5%. This deviation from zero arises from numerical errors in the computation of the CG strain tensor $C_{t_0}^{t_1}$, which in turn causes small inaccuracies in the computation of closed shearlines.

As noted earlier, the small relative stretching and the conservation of enclosed area for an elliptic barrier in incompressible flow only allows for small

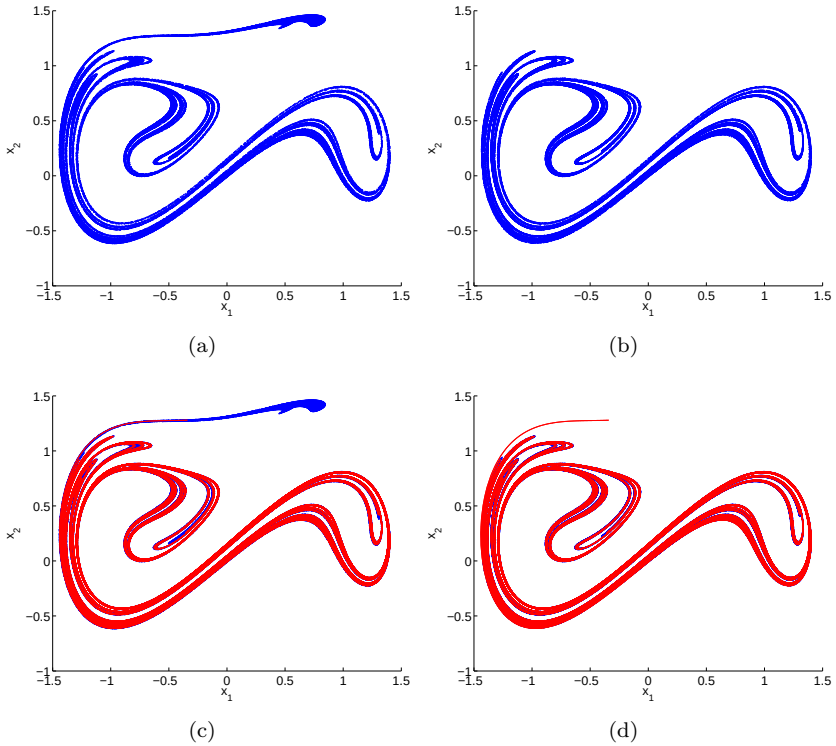

Figure 6.9: (a) Attractor of system (6.9) obtained from four iterates of the Poincaré map. (b) Attractor obtained from 20 iterates of the Poincaré map. (c) Attractor computed as a hyperbolic barrier (red), compared with the Poincaré map (blue) computed for the same integration time (four iterates). (d) Comparison of attractor computed as a hyperbolic barrier (red) with the one obtained from 20 iteration of the Poincaré map (blue). The integration time for locating the hyperbolic barrier is $T = t_1 - t_0 = -8\pi$.

deformations when the barrier is advected in time. This is illustrated in figure 6.13, which shows the blue elliptic barrier of figure 6.11b in the extended phase-space. Each constant-time slice of the figure is the advected image of the barrier.

Finally, we point out that the stability of the trajectories inside elliptic barriers show a similar trend as in the case of the periodically forced Duffing equation (figures 6.6 and 6.7). Namely, perturbations inside the elliptic regions remain small while they grow significantly inside the hyperbolic regions.

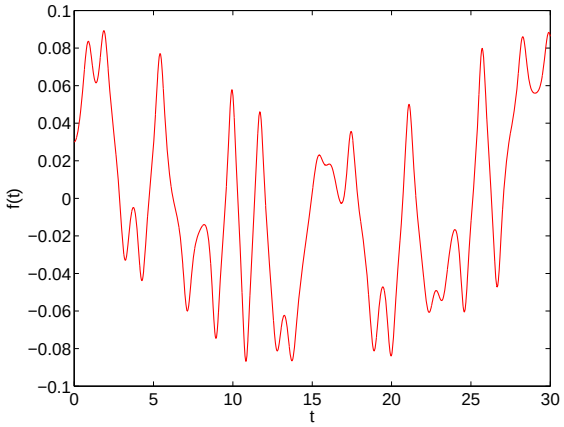

Figure 6.10: Chaotic forcing function $f(t)$ for equation (6.10).

Case 2: Aperiodic forcing with damping

In this final example, we consider the aperiodically forced, damped Duffing oscillator

$$\begin{aligned} \dot{x}_1 &= x_2, \\ \dot{x}_2 &= x_1 - x_1^3 - \delta x_2 + f(t), \end{aligned} \tag{6.12}$$

with damping coefficient $\delta = 0.15$. The forcing function $f(t)$ is similar to that of Case I above, but with an amplitude twice as large. As a result, none of the elliptic barriers survive even in the absence of damping.

Again, because of the aperiodic forcing, the behavior of this system is a priori unknown and cannot be explored using Poincaré maps. In order to investigate the existence of an attractor, strainlines (figure 6.14a) are computed from the backward-time CG strain tensor $C_{t_0}^{t_1}$ with $t_0 = 30$ and $t_1 = 10$. The strainline with minimum relative stretching (6.8) is then extracted.

In order to confirm the existence of the extracted attractor, we advect tracer particles in forward time, first from time $t_1 = 10$ to time $t_0 = 30$, then from $t_1 = 0$ to time $t_0 = 30$. Because of the fast-varying dynamics and weak dissipation, a relatively long advection time is required for the tracers to converge to the attractor. Figure 6.15 shows the evolution of tracers over $[t_1, t_0]$. Note that the attractor inferred from the tracers is less well pronounced than the hyperbolic barrier extracted over the same length of time. This shows a clear advantage for LCSs method over simple numerical experiments with tracer advection. For a longer integration time from $t_0 = 0$ to $t = 30$, the tracers eventually converge to the hyperbolic barrier.

Repelling hyperbolic barriers can be computed similarly using forward-time computations. Figure 6.16 shows both hyperbolic barriers (stable and unstable manifolds) at time $t_0 = 30$. The repelling barrier is computed from the CG strain tensor $\mathbf{C}_{t_0}^{t_1}$ with $t_0 = 30$ and $t_1 = 50$.

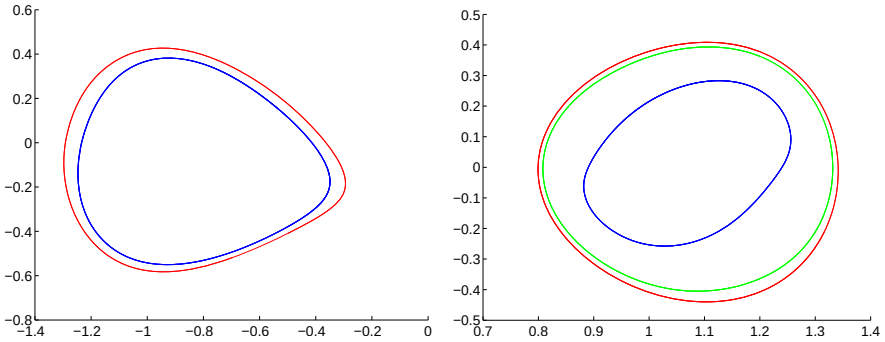

(a) (b)

Figure 6.11: Closed shearlines for equation (6.10) computed in two elliptic regions. The figure shows the shearlines at time $t_0 = 0$. The integration time is $T = 4\pi$.

6.4 Summary and Conclusions

We have used Lagrangian coherent structures to compute finite-time invariant sets in one-degree-of-freedom mechanical systems with general forcing. Specifically, in the presence of general time dependence, temporally aperiodic stable- and unstable manifolds, attractors, as well as generalized KAM tori can be located as hyperbolic and elliptic barriers, respectively. The hyperbolic barriers are computed as distinguished *strainlines*, i.e. material lines along which the Lagrangian strain is locally maximized. The elliptic barriers, on the other hand, appear as distinguished *shearlines*, i.e. material lines along which the Lagrangian shear is locally maximized.

We have used four simple examples for illustration. First, as benchmarks, we considered periodically forced Duffing equations for which stable and unstable manifolds, attractors and KAM curves can also be obtained as invariant sets of an appropriately defined Poincaré map. We have shown that elliptic barriers, computed as closed shearlines, coincide with the KAM curves. Also, stable and unstable manifolds, as well as attractors, can be recovered as hyperbolic barriers. More precisely, as the integration time $T = t_1 - t_0$ of the Cauchy–Green strain tensor $\mathbf{C}_{t_0}^{t_1}$ increases, the elliptic barriers in the periodically forced Duffing equations converge to KAM curves. Similarly, the chaotic attractor of the periodically forced and damped Duffing equation is more and more closely delineated by a hyperbolic barrier computed from the backward-time Cauchy–Green strain tensor $\mathbf{C}_{t_1}^{t_0}$ for increasing $T = t_0 - t_1$ where $t_0 > t_1$.

In the second set of examples, we have computed similar structures for an aperiodically forced Duffing oscillator with and without damping. In this case, Poincaré maps are no longer well-defined for the system, and hence we had to advect tracer particles to verify our predictions. Notably, tracer advection takes longer time to reveal the structures in full detail than the hyperbolic and elliptic

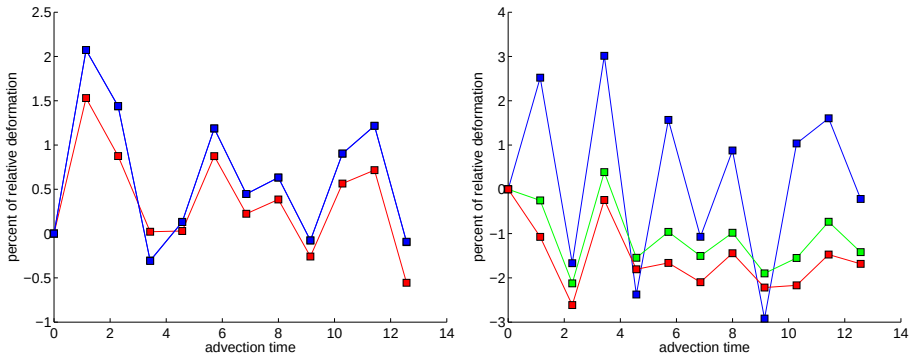

Figure 6.12: The relative stretching $\delta\ell(t) \times 100$ of closed shearlines of figure 6.11. The colors correspond to those of figure 6.11. By their arc-length preservation property, the advected elliptic barriers must theoretically have the same arclength at times $t_0 = 0$ and $t_1 = 4\pi$. The numerical error in arclength conservation is small overall, but more noticeable for oscillations with large amplitudes (green and red curves of the right panel).

barriers do. Also, tracer advection is only affective as a visualization tool if it relies on a small number of particles, which in turn assumes that one already roughly knows the location of the invariant set to be visualized. Finally, unlike scattered tracer points, LCSs are recovered as parametrized smooth curves that provide a solid foundation for further analysis or highly accurate advection.

In our examples, elliptic barriers have shown themselves as borders of subsets of the phase-space that barely deform over time. In fact, as illustrated in figure 6.6, outermost elliptic barriers define the boundary between chaotic and regular dynamics. Trajectories initiated inside elliptic barriers remain confined and robust with respect to small perturbations. We believe that this property could be exploited for stabilizing mechanical systems with general time dependence. For instance, formulating an optimal control problem for generating elliptic behavior in a desired part of the phase-space is a possible approach (see, e.g., Balasuriya and Padberg-Gehle [164] who developed a method for controlling stable and unstable manifolds in non-autonomous two-dimensional dynamical systems).

Undoubtedly, the efficient and accurate computation of invariant sets as LCSs requires dedicated computational resources. Smart algorithms reducing the computational cost are clearly of interest. Parallel programming (both at CPU and GPU levels) has previously been employed for Lagrangian coherent structure calculations and should be useful in the present setting as well (see e.g. [165, 166]). Other adaptive techniques are also available to lower the numerical cost by reducing the computations to regions of interest (see e.g. [167, 41]).

In principle, invariant sets in higher-degree-of-freedom mechanical systems could also be captured by similar techniques as locally least-stretching surfaces.

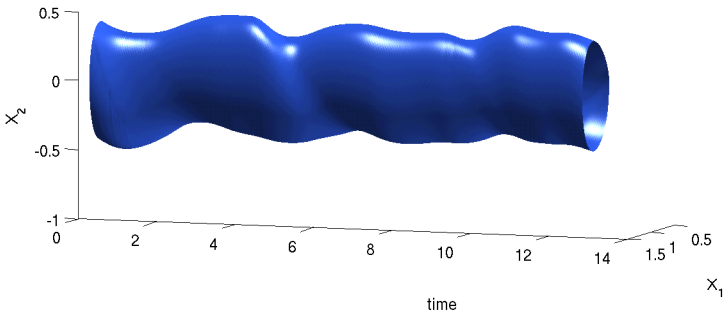

Figure 6.13: Generalized KAM-type cylinder in the extended phase space of the aperiodically forced Duffing undamped oscillator. The cylinder is obtained by advection of the closed shearline shown in blue in figure 6.11(b).

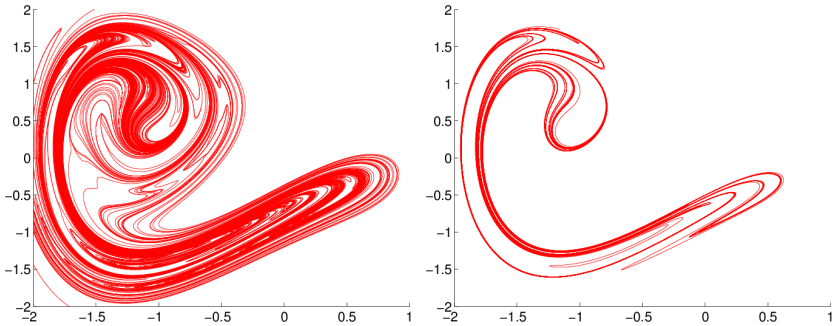

Figure 6.14: (a) Strainlines computed in backward time from $t_0 = 30$ to $t_1 = 10$. (b) The resulting hyperbolic barrier extracted as the least stretching strainline.

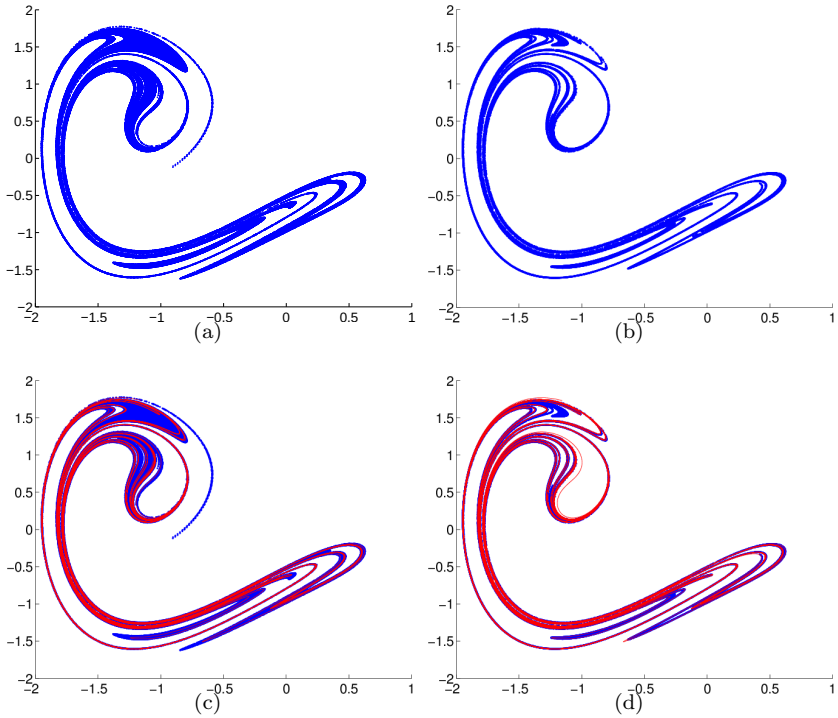

Figure 6.15: (a) Tracers advected over the time interval from $t_1 = 10$ to $t_0 = 30$. (b) Tracers advected over a longer time interval from $t_1 = 0$ to $t_0 = 30$. (c) The hyperbolic barrier (red) superimposed on the tracers advected for the same time interval (d) Comparison of the hyperbolic barrier (red) with the tracers advected for the longer time interval.

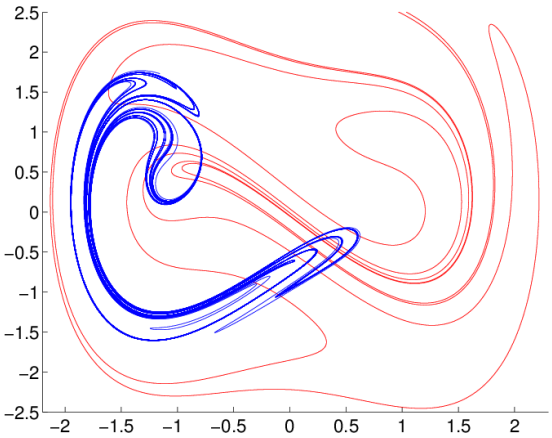

Figure 6.16: Attracting (blue) and repelling (red) barriers at $t_0 = 30$ extracted from backward-time and forward-time computations, respectively.

Bibliography

[1] G. Roy. *Combustion processes in propulsion: control, noise, and pulse detonation*. Butterworth-Heinemann, 2005.

[2] S. Hardt and F. Schönfeld. *Microfluidic technologies for miniaturized analysis systems*. Springer, 2007.

[3] D. L. Hartmann. *Global physical climatology*, volume 56. Academic press, 1994.

[4] L. M. Beal, W. PM De Ruijter, A. Biastoch, R. Zahn, et al. On the role of the Agulhas system in ocean circulation and climate. *Nature*, 472(7344): 429–436, 2011.

[5] A. J. Majda and P. R. Kramer. Simplified models for turbulent diffusion: Theory, numerical modelling, and physical phenomena. *Physics reports*, 314(4):237–574, 1999.

[6] J. Guckenheimer and P. Holmes. *Nonlinear oscillations, dynamical systems, and bifurcations of vector fields*, volume 42. New York, Springer Verlag, 1983.

[7] S. C. Shadden, F. Lekien, and J. E. Marsden. Definition and properties of Lagrangian coherent structures from finite-time Lyapunov exponents in two-dimensional aperiodic flows. *Physica D*, 212:271–304, 2005.

[8] H. Aref. Stirring by chaotic advection. *J. Fluid Mech.*, 143:1–21, 1984.

[9] J. M. Ottino. Mixing, chaotic advection and turbulence. *Ann. Rev. Fluid Mech.*, 22:207–253, 1990.

[10] R. S. MacKay. Complicated dynamics from simple topological hypotheses. *Philosophical Transactions of the Royal Society of London. Series A: Mathematical, Physical and Engineering Sciences*, 359(1784):1479–1496, 2001.

[11] S. Wiggins and J. M. Ottino. Foundations of chaotic mixing. *Philosophical Transactions of the Royal Society of London. Series A: Mathematical, Physical and Engineering Sciences*, 362(1818):937–970, 2004.

[12] S. Wiggins. *Normally hyperbolic invariant manifolds in dynamical systems*. Number 105 in Applied Mathematical Sciences. App. Math. Sci., Springer, 1994.

[13] V. Rom-Kedar, A. Leonard, and S. Wiggins. An analytical study of transport, mixing and chaos in an unsteady vortical flow. *Journal of Fluid Mechanics*, 214:347–394, 1990.

[14] R. de la Llave. A tutorial on KAM theory. In *Proceedings of Symposia in Pure Mathematics*, volume 69, pages 175–296. Providence, RI; American Mathematical Society; 1998, 2001.

[15] V. I. Arnold and B. A. Khesin. *Topological methods in hydrodynamics*, volume 125. Springer, 1998.

[16] L. J. Pratt, I. I. Rypina, T. M. Özgökmen, P. Wang, H. Childs, and Y. Bebieva. Chaotic advection in a steady, three-dimensional, Ekman-driven eddy. *J. Fluid Mech.*, 738:143–183, 2013.

[17] H. Aref, J. R. Blake, M. Budišić, J. H. E. Cartwright, H. J. H. Clercx, U. Feudel, R. Golestanian, E. Gouillart, Y. L. Guer, G. F. van Heijst, et al. Frontiers of chaotic advection. *arXiv preprint arXiv:1403.2953*, 2014.

[18] G. Haller and A. C. Poje. Finite time transport in aperiodic flows. *Physica D: Nonlinear Phenomena*, 119(3):352–380, 1998.

[19] K. Ide, D. Small, and S. Wiggins. Distinguished hyperbolic trajectories in time-dependent fluid flows: Analytical and computational approach for velocity fields defined as data sets. *Nonlinear Processes in Geophysics*, 9 (3/4):237–263, 2002.

[20] G. Haller. Finding finite-time invariant manifolds in two-dimensional velocity fields. *Chaos*, 10:99–108, 2000.

[21] G. Haller and G. Yuan. Lagrangian coherent structures and mixing in two-dimensional turbulence. *Physica D*, 147:352–370, 2000.

[22] G. Haller. Distinguished material surfaces and coherent structures in 3D fluid flows. *Physica D*, 149:248–277, 2001.

[23] G. Haller and F. J. Beron-Vera. Geodesic theory of transport barriers in two-dimensional flows. *Physica D*, 241(20):1680 – 1702, 2012.

[24] G. Haller and F. J. Beron-Vera. Coherent Lagrangian vortices: The black holes of turbulence. *J. Fluid Mech.*, 731, R4, 2013.

[25] D. Blazevski and G. Haller. Hyperbolic and elliptic transport barriers in three-dimensional unsteady flows. *submitted*, 2013.

[26] T. Ma and E. M. Bollt. Differential geometry perspective of shape coherence and curvature evolution by finite-time non-hyperbolic splitting. *arXiv preprint arXiv:1311.5457*, 2013.

[27] A. Lasota and M. C. Mackey. *Chaos, fractals, and noise: stochastic aspects of dynamics*, volume 97. Springer, 1994.

[28] G. Froyland. An analytic framework for identifying finite-time coherent sets in time-dependent dynamical systems. *Physica D*, 250:1–19, 2013.

[29] T. Ma and E. M. Bollt. Relatively coherent sets as a hierarchical partition method. *International Journal of Bifurcation and Chaos*, 23(07), 2013.

[30] M. Budisic, R. Mohr, and I. Mezic. Applied Koopmanism. *Chaos*, 22: 047510, 2012.

[31] M. Budišić and I. Mezić. Geometry of the ergodic quotient reveals coherent structures in flows. *Physica D: Nonlinear Phenomena*, 241(15):1255–1269, 2012.

[32] E. Aurell, G. Boffetta, A. Crisanti, G. Paladin, and A. Vulpiani. Predictability in the large: an extension of the concept of Lyapunov exponent. *Journal of Physics A: Mathematical and General*, 30(1):1, 1997.

[33] G. Haller. Lagrangian coherent structures from approximate velocity data. *Physics of Fluids (1994-present)*, 14(6):1851–1861, 2002.

[34] M. Mathur, G. Haller, T. Peacock, J. E. Ruppert-Felsot, and H. L. Swinney. Uncovering the Lagrangian skeleton of turbulence. *Physical Review Letters*, 98(14):144502, 2007.

[35] A. M. Mancho, S. Wiggins, J. Curbelo, and C. Mendoza. Lagrangian descriptors: A method for revealing phase space structures of general time dependent dynamical systems. *Communications in Nonlinear Science and Numerical Simulation*, 2013.

[36] I. I. Rypina, S. E. Scott, L. J. Pratt, M. G. Brown, and T. Tel. Investigating the connection between complexity of isolated trajectories and Lagrangian coherent structures. *Nonlinear Processes in Geophysics*, 18 (6), 2011.

[37] V. Pérez-Muñuzuri and F. Huhn. Path-integrated Lagrangian measures from the velocity gradient tensor. *Nonlinear Processes in Geophysics*, 20 (6), 2013.

[38] I. Mezić, S. Loire, V. A. Fonoberov, and P. Hogan. A new mixing diagnostic and Gulf oil spill movement. *Science*, 330(6003):486–489, 2010.

[39] F. Lekien and S. D. Ross. The computation of finite-time Lyapunov exponents on unstructured meshes and for non-Euclidean manifolds. *Chaos*, 20:017505, 2010.

[40] F. Lekien, S. C. Shadden, and J. E. Marsden. Lagrangian coherent structures in n-dimensional systems. *Journal of Mathematical Physics*, 48(6): 065404, 2007.

[41] D. Lipinski, B. Cardwell, and K. Mohseni. A Lagrangian analysis of a two-dimensional airfoil with vortex shedding. *Journal of Physics A: Mathematical and Theoretical*, 41(34):344011, 2008.

[42] F. J. Beron-Vera, M. J. Olascoaga, M. G. Brown, H. Koçak, and I. I. Rypina. Invariant-tori-like Lagrangian coherent structures in geophysical flows. *Chaos: An Interdisciplinary Journal of Nonlinear Science*, 20(1): 017514, 2010.

[43] S. Hendabadi, J. Bermejo, Y. Benito, R. Yotti, F. Fernández-Avilés, J. C. del Álamo, and S. C. Shadden. Topology of blood transport in the human left ventricle by novel processing of Doppler echocardiography. *Annals of biomedical engineering*, 41(12):2603–2616, 2013.

[44] G. Haller. A variational theory of hyperbolic Lagrangian Coherent Structures. *Physica D*, 240:574–598, 2011.

[45] M. Farazmand and G. Haller. Erratum and addendum to "A variational theory of hyperbolic Lagrangian Coherent Structures, *Physica D* **240** (2011) 574-598". *Physica D*, 241:439–441, 2012.

[46] D. Karrasch. Comment on a variational theory of hyperbolic Lagrangian coherent structures, physica d 240 (2011) 574–598. *Physica D: Nonlinear Phenomena*, 241(17):1470–1473, 2012.

[47] V. I. Arnold. *Mathematical Methods of Classical Mechanics*. Springer, 1978.

[48] M. Farazmand and G. Haller. Computing Lagrangian Coherent Structures from their variational theory. *Chaos*, 22:013128, 2012.

[49] M. Farazmand and G. Haller. Attracting and repelling Lagrangian coherent structures from a single computation. *Chaos*, 23:023101, 2013.

[50] M. Farazmand, D. Blazevski, and G. Haller. Shearless transport barriers in unsteady two-dimensional flows and maps. *Physica D*, 278-279:44–57, 2014.

[51] M. Farazmand and G. Haller. The Maxey-Riley equation: Existence, uniqueness and regularity of solutions. *J. Nonliner Analysis-B*, 2014. In press.

[52] M. Farazmand and G. Haller. How coherent are the vortices of two-dimensional turbulence? *arXiv preprint arXiv:1402.4835*, 2014.

[53] A. Hadjighasem, M. Farazmand, and G. Haller. Detecting invariant manifolds, attractors, and generalized KAM tori in aperiodically forced mechanical systems. *Nonlinear Dynamics*, 73(1-2):689–704, 2013.

[54] J. M. Ottino. *The kinematics of mixing: stretching, chaos and transport.* Cambridge University Press, 1989.

[55] A. Provenzale. Transport by coherent barotropic vortices. *Ann. Rev. Fluid Mech*, 31:55–93, 1999.

[56] G. Boffetta, G. Lacorata, G. Redaelli, and A. Vulpiani. Detecting barriers to transport: a review of different techniques. *Physica D*, 159:58–70, 2001.

[57] T. Peacock and J. Dabiri. Focus issue: Lagrangian Coherent Structures. *Chaos*, 20, 2010.

[58] M. Giona, A. Adrover, F. J. Muzzio, S. Cerbelli, and M. M. Alvarez. The geometry of mixing in time-periodic chaotic flows. I. Asymptotic directionality in physically realizable flows and global invariant properties. *Physica D*, 132:298–324, 1999.

[59] X. Tricoche, G. Scheuermann, and H. Hagen. A topology simplification method for 2D vector fields. *Proc. IEEE Visualization*, pages 359–366, 2000.

[60] T. Delmarcelle and L. Hesselink. The topology of symmetric, second-order tensor fields. In *Proceedings of the conference on Visualization '94*, pages 140–147, Los Alamitos, CA, USA, 1994. IEEE Computer Society Press.

[61] R. Abraham, J. E. Marsden, and T. Ratiu. *Manifolds, Tensor Analysis and Applications.* Springer, 1988.

[62] K. Tchon, J. Dompierre, M. G. Vallet, F. Guibault, and R. Camarero. Two-dimensional metric tensor visualization using pseudo-meshes. *Engineering with Computers*, 22:121–131, 2006.

[63] H. W. Broer, H. M. Osinga, and G. Vegter. Algorithms for computing normally hyperbolic invariant manifolds. *Z. angew Math. Phys.*, 48:480–524, 1997.

[64] A. M. Mancho, D. Small, S. Wiggins, and K. Ide. Computation of stable and unstable manifolds of hyperbolic trajectories in two-dimensional, aperiodically time-dependent vector fields. *Physica D*, 182:188–222, 2003.

[65] J. Chi, Y. Zhang, and C. Zhang. Optimized geometric Hermite curve based on curve length minimization. *IEEE 8th International Conference on Computer and Information Technology Workshops*, pages 330–335, 2008.

[66] J.-H. Yong and F. Cheng. Geometric Hermite curves with minimum strain energy. *Computer Aided Geometric Design*, 21:281–301, 2004.

[67] D. Lipinski and K. Mohseni. A ridge tracking algorithm and error estimate for efficient computation of Lagrangian coherent structures. *Chaos*, 20: 017504, 2010.

[68] C. Senatore and S. D. Ross. Detection and characterization of transport barriers in complex flows via ridge extraction of the finite-time Lyapunov exponent field. *Int. J. Num. Methods in Eng.*, 86:1163–1174, 2011.

[69] W. S. Edwards, L. S. Tuckerman, R. A. Friesner, and D. C. Sorensen. Krylov methods for the incompressible Navier–Stokes equations. *J. Comp. Phys.*, 110:82–102, 1994.

[70] S. Chen, R. E. Ecke, G. L. Eyink, X. Wang, and Z. Xiao. Physical mechanism of the two-dimensional enstrophy cascade. *Phys. Rev. Lett.*, 91: 214501, 2003.

[71] M. Farazmand, N. K.-R. Kevlahan, and B. Protas. Controlling the dual cascade of two-dimensional turbulence. *J. Fluid Mech.*, 668:202–222, 2011.

[72] M. J. Olascoaga and G. Haller. Forecasting sudden changes in environmental contamination patterns. *Poc. National Acad. Sci.*, 109:4738–4743, 2012.

[73] K. L. Palmerius, M. Cooper, and A. Ynnerman. Flow field visualization using vector field perpendicular surface. *Proceeding SCCG '09 (Proceedings of the 2009 Spring Conference on Computer Graphics)*, 2009.

[74] R. T. Frankot and R. Chellappa. A method for enforcing integrability in shape from shading algorithms. *IEEE Trans. Pattern Anal. and Machine Intelligence*, 10:439–451, 1988.

[75] G. Haller, M. Farazmand, and F. J. Beron-Vera. A variational theory of shear-type Lagrangian Coherent Structures. 2011. preprint.

[76] G. Haller and G. Yuan. Lagrangian coherent structures and mixing in two-dimensional turbulence. *Physica D*, 147:352–370, 2000.

[77] X. Tricoche, G. Scheuermann, and H. Hagen. A topology simplification method for 2D vector fields. In *Visualization 2000. Proceedings*, pages 359 –366, oct. 2000.

[78] J. M. Lee. *Manifolds and Differential Geometry (Graduate Studies in Mathematics)*. American Mathematical Society, 2009.

[79] J. Balzer. A Gauss-Newton method for the integration of spatial normal fields in shape space. *Journal of Mathematical Imaging and Vision*, 44: 65–79, 2012. ISSN 0924-9907.

[80] D. Karrasch. On attracting Lagrangian coherent structures. *arXiv preprint arXiv:1311.5043*, 2013.

[81] G. Haller and T. Sapsis. Lagrangian coherent structures and the smallest finite-time Lyapunov exponent. *Chaos*, 21:023115, 2011.

[82] D. del Castillo-Negrete, J. M. Greene, and P. J. Morrison. Area preserving nontwist maps: Periodic orbits and transition to chaos. *Physica D: Nonlinear Phenomena*, 91(1-2):1 – 23, 1996. ISSN 0167-2789.

[83] I. I. Rypina, M. G. Brown, F. J. Beron-Vera, H. Koçak, M. J. Olascoaga, and I. A. Udovydchenkov. Robust transport barriers resulting from strong Kolmogorov-Arnold-Moser stability. *Phys. Rev. Lett.*, 98:104102, March 2007.

[84] J. D. Szezech, I. L. Caldas, S. R. Lopes, P. J. Morrison, and R. L. Viana. Effective transport barriers in nontwist systems. *Phys. Rev. E*, 86:036206, 2012.

[85] R. M. Samelson. Fluid exchange across a meandering jet. *J. Phys. Oceanogr.*, 22:431–444, 1992.

[86] S. S. Abdullaev. *Construction of Mappings for Hamiltonian Systems and Their Applications (Lecture Notes in Physics, vol. 691)*. Berlin: Springer, 2006.

[87] V.I. Arnol'd. *Mathematical Methods of Classical Mechanics*. Graduate Texts in Mathematics. Springer, 1989. ISBN 9780387968902.

[88] A. Wurm, A. Apte, K. Fuchss, and P. J. Morrison. Meanders and reconnection–collision sequences in the standard nontwist map. *Chaos*, 15(2):023108, 2005.

[89] A. Delshams and R. de la Llave. KAM theory and a partial justification of Greene's criterion for nontwist maps. *SIAM Journal on Mathematical Analysis*, 31(6):1235–1269, 2000.

[90] U. Vaidya and I. Mezic. Existence of invariant tori in three dimensional maps with degeneracy. *Physica D: Nonlinear Phenomena*, 241(13):1136 – 1145, 2012.

[91] A. González-Enrıquez, A. Haro, and R. de la Llave. Singularity theory for non-twist KAM tori. *Memoirs of the AMS*, pages 11–179, 2012.

[92] T. C. Hender, P. Hennequin, B. Alper, T. Hellsten, D. F. Howell, G. T. A. Huysmans, E. Joffrin, P. Maget, J. Manickam, M. F. F. Nave, A. Pochelon, S. E. Sharapov, and contributors to EFDA-JET workprogramme. MHD stability with strongly reversed magnetic shear in JET. *Plasma Physics and Controlled Fusion*, 44(7):1143, 2002.

[93] R. Lorenzini, E. Martines, P. Piovesan, D. Terranova, P. Zanca, M. Zuin, A. Alfier, D. Bonfiglio, F. Bonomo, A. Canton, S. Cappello, L. Carraro,

R. Cavazzana, D. F. Escande, A. Fassina, P. Franz, M. Gobbin, P. Innocente, L. Marrelli, R. Pasqualotto, M. E. Puiatti, M. Spolaore, M. Valisa, N. Vianello, and P. Martin. Self-organized helical equilibria as a new paradigm for ohmically heated fusion plasmas. *Nat Phys*, 5(8):570–574, June 2009.

[94] R. Lorenzini, A. Alfier, F. Auriemma, A. Fassina, P. Franz, P. Innocente, D. Lopez-Bruna, E. Martines, B. Momo, G. Pereverzev, P. Piovesan, G. Spizzo, M. Spolaore, and D. Terranova. On the energy transport in internal transport barriers of rfp plasmas. *Nuclear Fusion*, 52(6):062004, 2012.

[95] D. Blazevski and D. del Castillo-Negrete. Local and nonlocal anisotropic transport in reversed shear magnetic fields: Shearless cantori and nondiffusive transport. *Phys. Rev. E*, 87:063106, June 2013.

[96] D. del Castillo-Negrete and P. J. Morrison. Chaotic transport by Rossby waves in shear flow. *Physics of Fluids A: Fluid Dynamics*, 5(4):948–965, 1993.

[97] I. I. Rypina, M. G. Brown, F. J. Beron-Vera, H. Kocak, M. J. Olascoaga, and I. A. Udovydchenkov. On the Lagrangian dynamics of atmospheric zonal jets and the permeability of the stratospheric polar vortex. *Journal of the Atmospheric Sciences*, 64(10):3595–3610, 2007.

[98] R. P. Behringer, S. D. Meyers, and H. L. Swinney. Chaos and mixing in a geostrophic flow. *Physics of Fluids A: Fluid Dynamics*, 3(5):1243–1249, 1991.

[99] R. M. Samelson and S. Wiggins. *Lagrangian transport in geophysical jets and waves: the dynamical systems approach*, volume 31 of *Interdisciplinary Applied Mathematics*. Springer, 2006.

[100] F. J. Beron-Vera, M. J. Olascoaga, M. G. Brown, H. Kocak, and I. I. Rypina. Invariant-tori-like lagrangian coherent structures in geophysical flows. *Chaos: An Interdisciplinary Journal of Nonlinear Science*, 20(1): 017514, 2010.

[101] T. Delmarcelle and L. Hesselink. The topology of symmetric, second-order tensor fields. In *Visualization, 1994., Visualization '94, Proceedings., IEEE Conference on*, pages 140–147, CP15, 1994.

[102] X. Tricoche, X. Zheng, and A. Pang. Visualizing the topology of symmetric, second-order, time-varying two-dimensional tensor fields. In J. Weickert and H. Hagen, editors, *Visualization and Processing of Tensor Fields*, Mathematics and Visualization, pages 225–240. Springer Berlin Heidelberg, 2006.

[103] G. K. Batchelor. *An introduction to fluid dynamics*. Cambridge university press, 1967.

[104] J. K. Beem, P. E. Ehrlich, and K. L. Easley. *Global Lorentzian Geometry.* Chapman & Hall CRC Press, second edition, 1996.

[105] S. Shinohara and Y. Aizawa. Indicators of reconnection processes and transition to global chaos in nontwist maps. *Progr. Theoret. Phys.*, 100 (2):219–233, 1998. ISSN 0033-068X.

[106] D. del Castillo-Negrete. Self-consistent chaotic transport in fluids and plasmas. *Chaos: An Interdisciplinary Journal of Nonlinear Science*, 10 (1):75–88, 2000.

[107] L. Carbajal, D. del Castillo-Negrete, and J. J. Martinell. Dynamics and transport in mean-field coupled, many degrees-of-freedom, area-preserving nontwist maps. *Chaos: An Interdisciplinary Journal of Nonlinear Science*, 22(1):013137, 2012.

[108] N. J. Balmforth, P. J. Morrison, and J.-L. Thiffeault. Pattern formation in Hamiltonian systems with continuous spectra: a normal-form single-wave model. *Review of Modern Physics, Submitted*, 2013.

[109] J. L. Tennyson, J. D. Meiss, and P. J. Morrison. Self-consistent chaos in the beam-plasma instability. *Physica D*, 71(1–2):1–17, 1994.

[110] G. Froyland, N. Santitissadeekorn, and A. Monahan. Transport in time-dependent dynamical systems: Finite-time coherent sets. *Chaos*, 20(4): 043116, 2010.

[111] M. Dellnitz, G. Froyland, C. Horenkamp, K. Padberg-Gehle, and A. Sen Gupta. Seasonal variability of the subpolar gyres in the Southern Ocean: a numerical investigation based on transfer operators. *Nonlin. Processes Geophys*, 16(4):655–664, 2009.

[112] J. C. McWilliams. *Fundamentals of geophysical fluid dynamics.* Cambridge University Press, 2006.

[113] F. J. Beron-Vera, Y. Wang, M. J. Olascoaga, G. J. Goni, and G. Haller. Objective detection of oceanic eddies and the Agulhas leakage. *J. Phys. Oceanogr.*, 43:1426–1438, 2013.

[114] I. M. Gelfand and S. V. Fomin. *Calculus of variations.* Dover Publications, 2000. Translated and edited by R. A. Silverman.

[115] C. M. Tchen. *Mean value and correlation problems connected with the motion of small particles suspended in a turbulent fluid.* PhD thesis, TU Delft, 1947.

[116] S. Corrsin and J. Lumley. On the equation of motion for a particle in turbulent fluid. *App. Sci. Res., Section A*, 6(2-3):114–116, 1956.

[117] M. R. Maxey and J. J. Riley. Equation of motion for a small rigid sphere in a nonuniform flow. *Phys. Fluids*, 26:883–889, 1983.

[118] E. van Sebille, M. H. England, and Gary Froyland. Origin, dynamics and evolution of ocean garbage patches from observed surface drifters. *Env. Res. Lett.*, 7(4):044040, 2012.

[119] D. Vallero. *Fundamentals of air pollution.* Academic press, fourth edition, 2008.

[120] J. D. Schwarzkopf, M. Sommerfeld, and Y. Tsuji. *Multiphase flows with droplets and particles.* CRC press, 2011.

[121] M. R. Maxey. The gravitational settling of aerosol particles in homogeneous turbulence and random flow fields. *J. Fluid Mech.*, 174(1):441–465, 1987.

[122] A. Babiano, J. H. E. Cartwright, O. Piro, and A. Provenzale. Dynamics of a small neutrally buoyant sphere in a fluid and targeting in Hamiltonian systems. *Phys. Rev. Lett.*, 84:5764–5767, 2000.

[123] G. Haller and T. Sapsis. Where do inertial particles go in fluid flows? *Physica D*, 237(5):573–583, 2008.

[124] F. Candelier, J. R. Angilella, and M. Souhar. On the effect of the Boussinesq–Basset force on the radial migration of a Stokes particle in a vortex. *Physics of Fluids*, 16(5):1765–1776, 2004.

[125] A. Daitche and T. Tél. Memory effects are relevant for chaotic advection of inertial particles. *Phys. Rev. Lett.*, 107:244501, 2011.

[126] A. Daitche. Advection of inertial particles in the presence of the history force: Higher order numerical schemes. *Journal of Computational Physics*, 254:93–106, 2013.

[127] C. M. F. Coimbra and R. H. Rangel. General solution of the particle momentum equation in unsteady Stokes flows. *J. of Fluid Mech.*, 370(1): 53–72, 1998.

[128] T. A. Burton and I. K. Purnaras. Singular integro-differential equations with small kernels. *J. of Integral Equations and Applications*, 25(1):1–20, 2013.

[129] T. A. Burton and I. K. Purnaras. L^p-solutions of singular integro-differential equations. *J. of Math. Anal. Appl.*, 386(2):830–841, 2012.

[130] I. Petrás. *Fractional-order nonlinear systems: modeling, analysis and simulation.* Springer, 2011.

[131] I. Podlubny. *Fractional Differential Equations. An Introduction to Fractional Derivatives, Fractional Differential Equations, Some Methods of Their Solution and Some of Their Applications.* Academic Press, San Diego - New York - London, 1999.

[132] M. R. Maxey. The equation of motion for a small rigid sphere in a nonuniform or unsteady flow. In *Gas-solid flows, 1993*, volume 166, pages 57–62. The American society of mechanical engineers, 1993.

[133] T. Sapsis and G. Haller. Inertial particle dynamics in a hurricane. *J. of the Atmos. Sci.*, 66(8):2481–2492, 2009.

[134] H. Kellay and W. I. Goldburg. Two-dimensional turbulence: a review of some recent experiments. *Reports on Progress in Physics*, 65(5):845, 2002.

[135] A. Provenzale, A. Babiano, A. Bracco, C. Pasquero, and J. B. Weiss. Coherent vortices and tracer transport. In *Transport and Mixing in Geophysical Flows, Lecture Notes in Physics*, pages 101–118. Springer, 2008.

[136] G. Boffetta and R. E. Ecke. Two-dimensional turbulence. *Ann. Rev. Fluid Mech.*, 44:427–451, 2012.

[137] U. Frisch. *Turbulence: the legacy of A.N. Kolmogorov*. Cambridge University Press, 1995.

[138] J. Jeong and F. Hussain. On the identification of a vortex. *J. of Fluid Mech.*, 285:69–94, 1995.

[139] G. Haller. An objective definition of a vortex. *J. Fluid Mech.*, 525:1–26, 2005.

[140] A. Okubo. Horizontal dispersion of floatable particles in the vicinity of velocity singularities such as convergences. *Deep Sea Research*, 17:445–454, 1970.

[141] J. Weiss. The dynamics of enstrophy transfer in two-dimensional hydrodynamics. *Physica D*, 48:273–294, 1991.

[142] B. L. Hua and P. Klein. An exact criterion for the stirring properties of nearly two-dimensional turbulence. *Physica D*, 113(1):98–110, 1998.

[143] C. Truesdell and W. Noll. *The non-linear field theories of mechanics*. Springer, New York, third edition, 2004.

[144] J. Beem, P. Ehrlich, and K. Easley. Global Lorentzian geometry, volume 202 of monographs and textbooks in pure and applied mathematics, 1996.

[145] J. R. Dormnad and P. J. Prince. A family of embedded Runge-Kutta formulae. *J. Comp. Appl. Math.*, 6:19–26, 1980.

[146] R. H. Kraichnan. Inertial ranges in two-dimensional turbulence. *Phys. Fluids*, 10:1417–1423, 1967.

[147] P. E. Merilees and H. Warn. On energy and enstrophy exchanges in two-dimensional non-divergent flow. *J. Fluid Mech.*, 69:625–630, 1975.

[148] G. Boffetta, A. Celani, S. Musacchio, and M. Vergassola. Intermittency in two-dimensional Ekman–Navier-Stokes turbulence. *Phys. Rev. E*, 66: 026304, 2002.

[149] Y.-K. Tsang, E. Ott, T. M. Antonsen, and P. N. Guzdar. Intermittency in two-dimensional turbulence with drag. *Phys. Rev. E*, 71:066313, 2005.

[150] J. C. McWilliams. The vortices of two-dimensional turbulence. *J. Fluid Mech.*, 219:361–385, 1990.

[151] R. T. Pierrehumbert and H. Yang. Global chaotic mixing on isentropic surfaces. *J. Atmos. Sci.*, 50:2462–2480, 1993.

[152] M. S. Chong, A. E. Perry, and B. J. Cantwell. A general classification of three-dimensional flow fields. *Phys. fluids A*, 2(5):765–777, 1990.

[153] M. Tabor and I. Klapper. Stretching and alignment in chaotic and turbulent flows. *Chaos, Solitons & Fractals*, 4(6):1031 – 1055, 1994.

[154] S. Kida and H. Miura. Identification and analysis of vortical structures. *European Journal of Mechanics - B/Fluids*, 17(4):471 – 488, 1998.

[155] M. Budišić, R. Mohr, and I. Mezić. Applied Koopmanism. *Chaos*, 22(4): 047510, 2012.

[156] F. J. Beron-Vera, Y. Wang, M. J. Olascoaga, G. J. Goni, and G. Haller. Objective detection of oceanic eddies and the Agulhas leakage. *J. of Phys. Oceanogr.*, 43(7), 2013.

[157] S. Leung. An Eulerian approach for computing the finite time Lyapunov exponent. *J. of Comp. Phys.*, 230(9):3500–3524, 2011.

[158] S. C. Shadden. Lagrangian coherent structures. In *Transport and Mixing in Laminar Flows: From Microfluidics to Oceanic Currents, edited by Roman Grigoriev*, pages 59–89. Wiley, New York, 2011.

[159] R. Peikert, A. Pobitzer, F. Sadlo, and B. Schindler. A comparison of finite-time and finite-size Lyapunov exponents. *Topological Methods in Data Analysis and Visualization III. Springer*, 2014.

[160] D. H. Kelley, M. R. Allshouse, and N. T. Ouellette. Lagrangian coherent structures separate dynamically distinct regions in fluid flows. *Phys. Rev. E*, 88:013017, 2013.

[161] B. Rutherford and G. Dangelmayr. A three-dimensional Lagrangian hurricane eyewall computation. *Quarterly Journal of the Royal Meteorological Society*, 136(653):1931–1944, 2010.

[162] Y.-C. Lai and T. Tél. *Transient chaos: complex dynamics on finite time scales*, volume 173. Springer, 2011.

[163] D. Karrasch, F. Huhn, and G. Haller. Automated detection of coherent Lagrangian vortices in two-dimensional unsteady flows. *arXiv preprint arXiv:1404.3109*, 2014.

[164] S. Balasuriya and K. Padberg-Gehle. Nonautonomous control of stable and unstable manifolds in two-dimensional flows. *Physica D*, 276(0):48 – 60, 2014.

[165] C. Garth, G.-S. Li, X. Tricoche, C. D Hansen, and H. Hagen. Visualization of coherent structures in transient 2d flows. In *Topology-Based Methods in Visualization II*, pages 1–13. Springer, 2009.

[166] S. Ameli, Y. Desai, and S. C. Shadden. Development of an efficient and flexible pipeline for Lagrangian coherent structure computation. In P.-T. Bremer, I. Hotz, V. Pascucci, and R. Peikert, editors, *Topological Methods in Data Analysis and Visualization III*, Mathematics and Visualization, pages 201–215. Springer International Publishing, 2014.

[167] S. Barakat, C. Garth, and X. Tricoche. Interactive computation and rendering of finite-time Lyapunov exponent fields. *Visualization and Computer Graphics, IEEE Transactions on*, 18(8):1368–1380, 2012.